UNIVERSIDADE D
COIMBRA

Maria Ana Cruz Moita

Impact of Cesium Carbonate Doping and Heat-Light Soaking on Cu(In,Ga)Se_2 Thin-Film Solar Cell Performance

Dissertation within the scope of Integrated Master in Physics Engineering supervised by Nicoleta Nicoara and Professor Helena Vieira Alberto

University of Coimbra

Physics Department of Faculty of Sciences and Technology

2022/2023

Acknowledgments

Firstly, I wish to express my most sincere appreciation towards my supervisors. To Dr.Nicoleta Nicoara for the guidance and help during my internship in INL and in the thesis writing. To Professor Helena Vieira Alberto for all the encouragement, guidance and support given during my thesis writing and for all the immense learning and kindness transmitted to me over the past years. I would also like to thank Ishwor Khatri for the guidance in the laboratory and to Dr. Sascha Sadewasser for accepting me in the group as well as to INL, where I spent some good times.

In addition, I would like to express how grateful I am for having worked side by side with my colleagues from LaNaSc, Kate, Patrícia, Daniel, Matej, Christian, Francisco, Wesley, Mathieu, Alessandro and Bruno. I laughed a lot, had very interesting conversations and learned a lot from them. A special thanks to Pedro Santos, Diana, Marina and Pedro Sousa for sharing their knowledge with me and helping me when I needed.

I want to share my appreciation to Eng.Pedro Sousa and my colleagues in Oncontrol, for their encouragement during my thesis writing.

My friends from Coimbra, specially Ana Pereira, Bárbara, Inês Morgado, Maria Diz, Francisca, Ana Mateus, Inês Sequeira, Joana, André, Gabriela and all the others that I did not mention here were also very important to me during this journey, thank you for all the support, motivation words, videocalls to study and advice! Thank you to all my friends with whom I shared these college years.

Finally, I want to thank to the most special people I have with me, my family, for being my cornerstones everyday, no words can express how grateful and lucky I am for having your support, understanding and love.

To my Avô Moita

Resumo

O presente trabalho analisa e carateriza extensivamente células solares de filme fino de Cu(In,Ga)Se_2 com uma buffer layer de CdS, que foram fabricadas usando um processo inovativo de dopagem baseado na técnica de spin-coating de uma solução aquosa de carbonato de césio ($CsCO_3$). As células solares foram fabricadas por Ishwor Khatri. Neste trabalho, as amostras foram sujeitas aos tratamentos de exposição à luz (LS), ao calor (HS) e exposição conjunta de luz e calor (HLS) e caraterizadas antes e depois destes tratamentos. A caraterização das mesmas foi realizada usando medidas de J-V e Eficiência Quântica Externa (EQE).

O tratamento de pós-deposição com a solução de Césio melhorou os parâmetros básicos das células solares, levando a um aumento de aproximadamente 100mV e 3.1% na tensão em circuito aberto (V_{OC}) e Eficiência, respetivamente, na amostra que foi sujeita a este tratamento duas vezes. As medidas de EQE também evidenciaram uma melhoria na absorção de fotões e colecção dos respetivos portadores de carga entre os 500nm e os 1100nm, indicando a redução de perdas por recombinação no absorsor e possivelmente na interface CIGS/CdS. A modificação da superfície da camada de CIGS e a eliminação de níveis profundos intra-banda foram sugeridos como possíveis razões para estas melhorias.

Nenhum efeito foi verificado numa amostra tratada duas vezes com spin-coating após ter sido realizado o LS, com duração de 1 hora. O equilíbrio entre efeitos prejudiciais e benéficos é discutido como sendo uma possível razão para tal comportamento: o aumento de flutuações eletrostáticas devido à redistribuição dos átomos de Cs após o LS e o aumento do comprimento de difusão dos portadores de carga. Para potencialmente atingir efeitos visíveis, é sugerido que as células permaneçam no escuro por mais tempo após este tratamento, para permitir uma melhor redistribuição de cargas.

Uma amostra tratada duas vezes com spin-coating foi exposta durante 30 minutos a uma temperatura de 75 ^{o}C e não foram observadas alterações relevantes. É sugerida uma exposição mais prolongada e a temperaturas mais elevadas em futuros tratamentos para, possivelmente, permitir passivação de defeitos, substituição iónica de elementos alcalinos mais leves e a ativação da conversão do defeito complexo V_{Se}-V_{Cu}.

O tratamento de HLS foi efetuado cumulativamente dos 75 ^{o}C aos 145 ^{o}C a uma amostra tratada uma vez com spin-coating e a uma amostra de referência (sem qualquer tratamento de pós-deposição). Um impacto semelhante foi constatado em ambas as amostras: o decréscimo na tensão em circuito aberto e o aumento da densidade de corrente de curto-circuito (J_{SC}) com o aumento de temperatura. Não foram verificadas mudanças significativas no fator de preenchimento (FF) e na eficiência devido às suas incertezas elevadas. O trade-off observado contradiz o descrito na literatura, sugerindo um aumento da zona de depleção e uma diminuição da concentração efetiva de lacunas na camada de CIGS. Contudo esta hipótese está aberta a discussão, uma vez que a distorção observada na curva J-V em algumas células depois do HLS a 145ºC pode ser resultado da acumulação de lacunas na camada de CIGS. As medidas de EQE revelaram um aumento nos comprimentos de onda curtos com o aumento da temperatura para a célula tratada com Césio, indicando uma melhor absorção de fotões e coleção dos respetivos portadores gerados na camada de CdS e na interface CdS/CIGS, em contraste com o que sucedeu para a amostra de referência, onde uma diminuição de EQE se deu. A distorção na curva J-V é menos pronunciada para a amostra tratada com Césio, o que é atribuído, hipoteticamente, à melhor absorção de luz azul nesta amostra.

Keywords

Cu(In, Ga)Se_2 , Tratamento por solução de Césio, Exposição à luz, Exposição ao calor, Exposição conjunta à luz e calor

Abstract

The present work thoroughly analyzes and characterizes Cu(In,Ga)Se_2 solar cells with CdS buffer layer, that were fabricated using a novel spin-coating $CsCO_3$ solution PDT process. The solar cells were fabricated by Ishwor Khatri. In this work, the cells were treated by LS (Light Soaking), HS (Heat Soaking and HLS (Heat-Light Soaking) and characterized before and after these treatments. The characterization was performed using J-V and External Quantum Efficiency measurements.

The Cs-solution process improved the basic parameters of CIGS solar cells, leading to an increase in V_{OC} by $\sim$100 mV and efficiency by $\sim 3.1\%$ in the twice spin-coated sample. EQE measurements showed improved absorption of photons and collection of carriers between 500nm and 1100nm, indicating reduced recombination losses in the absorber and possibly at the CIGS/CdS interface. Possible causes for these improvements include modification of the CIGS surface and reduction of deep-gap states in grain-boundaries.

The light-soaking (LS) treatment performed for 1 hour did not result in any noticeable changes in the twice spin-coated samples. It is believed that this balance of detrimental and beneficial effects, including the increase of electrostatic fluctuations due to the redistribution of Cesium atoms and the increase of the diffusion length of the charge carriers, may have contributed to this outcome. To potentially achieve noticeable effects, it is suggested that the cells be left in the dark for a longer period to allow for a better redistribution of charges.

The heat-soaking (HS) treatment done for 30 minutes at 75 ^{o}C in the twice spin-coated sample showed no significant changes. It is suggested that higher temperatures or longer exposure time be considered in future treatments to allow for passivation of defects, ionic substitution of lighter alkali atoms and activation of the conversion of the V_{Se}-V_{Cu} defect complex.

The effect of cumulative HLS from 75 ^{o}C to 145 ^{o}C on the non-treated and on the once Cs spin-coated CIGS samples was studied. Both samples showed a decrease of the V_{OC}, an increase of the J_{SC} with increasing temperature and no significant changes in the FF and Efficiency due to the large errors of these parameters. The observed trade-off contradicts previous literature and suggests an increase in the space-charge region and a decrease in the net hole concentration. Nevertheless, this hypothesis is opened to discussion, since a J-V distortion observed for some cells in both samples after HLS at 145 ^{o}C may be resultant of the accumulation of excess holes in the CIGS layer. The Cs-treated sample showed an increase in short wavelength EQE with increasing temperature, indicating a better absorption of photons in the CdS and CdS/CIGS interface and corresponding collection of carriers, while the non-treated sample showed a decrease. The J-V distortion is less pronounced for the Cs solution-treated solar cell, which is suggested to be due to the better absorption of blue light by this sample.

Keywords

Cu(In, Ga)Se_2 , Cesium-solution treatment, Light Soaking, Heat Soaking, Heat-Light Soaking

Table of Contents

List of Tables

List of Figures

Abreviations

AM Air Mass

ARC Antireflective Layer

AZO Aluminium Zinc Oxide

CdS Cadmium Sulphide

CdTe Cadmium Telluride

CIGS Copper Indium Gallium Diselenide

Cs Cesium

$CsCO_3$ Cesium Carbonate

CsF Cesium Fluoride

DI De-ionized

EF Fermi Level

EQE External Quantum Efficiency

FF Fill Factor

GB Grain Boundaries

HBS Heat-Bias Soaking

HLS Heat-Light Soaking

HS Heat Soaking

I Current

I_L Photocurrent

I_S Saturation/Dark Current

i-ZnO Intrinsic Zinc Oxide

J_{SC} Short-Circuit Current Density

J-V Current Density-Voltage

k_B Boltzman Constant

KF Potassium Fluoride

LS Light Soaking

Mo Molybdenum

$MoSe_2$ Molybdenum Diselenide

N_A Acceptor Concentration

NaF Sodium Fluoride

N_D Donor concentration

PDT Post-Deposition Treatment

PHRMS Pulsed Hybrid Reactive Magnetron Sputtering

P_{in} Incident Solar Radiation Power

P_{max} Maximum Power

P_{out} Cell Power Output

PV Photovoltaic

PVD Physical Vapor Deposition

R_S Series Resistance

R_{Sh} Shunt Resistance

RT Room Temperature

SCR Space-Charge Region

Si Silicon

SLG Soda-Lime Glass

STAR Sputtering Advanced System for Research

T Temperature

TCO Transparent Conductive Oxide

V Voltage

VBM Valence Band Maximum

V_{OC} Open Circuit Voltage

WL Wavelength

ZnO Zinc Oxide

ZnO:Al Alluminium-doped Zinc Oxide

Chapter 1

Introduction

The climate crisis and the continuing growth of global population demand a replacement of fossil fuels with renewable energy sources. Solar energy is the most abundant and cleanest source of energy, seeing that the Earth's surface receives enough energy in one hour to meet the world's annual energy demands. Therefore, it is necessary to take advantage of this energy, which can be achieved using photovoltaic systems. This technology must be competitive in terms of costs with the more traditional carbon-based sources (coil, oil and natural gas)[19].

Currently, the photovoltaics market is dominated by the first generation of solar cells: mainly based on monocrystalline or polycrystalline silicon wafers. The efficiency of these cells has reached about 26.7%, mainly limited by the spectral response of the silicon single-junction semiconductor. This type of solar cells has absorber layers with thicknesses above 100μm, which require complex and expensive manufacturing processes, besides, its production requires a high thermal budget owing to the high temperatures needed, of around 1100 ^{o}C[6][20].

An alternative to these cells are the second generation cells, based on metal chalcogenides, Cadmium Telluride and Copper Indium Gallium Selenide. CIGS are the most promising alternative considering that Cadmium is highly toxic, which brings difficulties in the large-scale commercialization of CdTe solar cells[6]. CIGS are direct band gap semiconductors unlike the indirect band gap semiconductor Si and possess large light absorption coefficients, which allow the use of thin light absorber layers in high-efficiency solar cells, reducing the material consumption and allowing the fabrication of lightweight and flexible solar cells[19]. Furthermore, these cells can be produced through different production technologies, which makes them cheaper[20].

Recently, the new efficiency record of the CIGS solar cell was achieved, 23.35%, with a CIGS using a cesium floride (CsF) post-deposition treatment (PDT)[21]. Alkali incorporation, specially of heavy alkalis (K, Rb and Cs), into the CIGS films has been crucial to attain high efficiency solar cells and has been mainly done through the evaporation of alkali-halides (KF, RbF, CsF) on CIGS' surface in vaccuum conditions[15][18]. In light of the prospect of employing printing and coating tecnhiques for large area device fabrication, the doping process of CIGS will have to be achieved through solution processing. A

few studies were done about solution processing of alkali metals, where alkali-halides are dissolved in a solution and spin-coated on the CIGS film[22][23]. A low-cost solution process for incorporating Cs into the CIGS thin films through spin-coating was developed by I.Khatri[18]. The solution used in this PDT was an aqueous solution of cesium carbonate ($CsCO_3$) [18] which before was only used to do interface modifications in organic light-emitting devices, polymer light-emitting devices [24], organic solar cells and perovskite solar cells[25].

Besides the alkali treatments, post-treatments, such as light, heat and heat-light soaking (LS, HS and HLS), which are done after the fabrication of the complete solar cells, have been studied to understand their effects on the CIGS solar cells because these induce a positive effect on the operation of the solar cells in certain conditions. [26][27][17] The effect of the LS and HS has been mainly studied in non-treated CIGS in contrast to the HLS. Lately, the focus shifted to the influence of HLS on alkali-fluoride treated CIGS solar cells[28] on account of the greater improvements on the treated cells when comparing to the non-treated cells subjected to this treatment[29] [30]. The impacts of LS, HS, and HLS on CIGS solar cells treated with a spin-coated $CsCO_3$ solution have not been investigated yet due to the recent development of this particular PDT.

The present work thoroughly analyzes and characterizes solar cells fabricated by I.Khatri using a spin-coating $CsCO_3$ solution process[1], before and after LS, HS, and HLS treatments. The main objectives of this thesis are:

- To conduct a comprehensive literature review on the fundamentals of photovoltaic technology and the properties of $Cu(In,Ga)Se_2$ solar cells.
- To acquire knowledge in electrical and optoelectronic device analysis techniques.
- To understand the effect of the $CsCO_3$ solution doping mechanism on device performance.
- To assess the impact of LS, HS, and HLS treatments on treated and non-treated CIGS cells.

Unfortunately, fabricating the solar cells and conducting further characterizations was hindered by high demand for the STAR system (where the cells were made) and its malfunctions, limiting the analysis to pre-fabricated cells. Additional characterizations were not possible due to time constraints.

This thesis is structured in 7 chapters. Chapter 1 introduces the motivation and goals, and outlines the challenges faced. Chapter 2 provides an overview of the key concepts and principles related to solar cells for better interpretation of the results. Chapter 3 and 4 present a literature review of the existing work on alkali-PDT and LS, HS and HLS treatments respectively. Chapter 5 describes the experimental methods used. Chapter 6 presents the results and discussion. Finally, Chapter 7 summarizes the main conclusions and suggests future work.

[1] The solar cells were fabricated in the STAR chamber within the LaNaSC laboratory where the present work was done.

Chapter 2

Main concepts and principles

2.1 Solar spectrum

Solar energy is the renewable source most abundant nowadays[31]. Thereby, it is essential to understand its distribution to be able to use it in the most efficient way. The sun's energy is radiated in the form of electromagnetic radiation[6]. The solar spectrum can be approached to a black body's spectrum of temperature 5900K[32], as it is plain to see in Figure 2.1, and varies depending on the location, time of the day, season, latitude, altitude above sea level, angle of the sun, among other factors.

To allow the performance comparison between different photovoltaic devices, standard reference spectra have been defined. These spectra vary according to the value of the Air Mass (AM) considered[33]. The Air Mass is used to describe the relative path length that the sun's rays cross through the atmosphere before reaching the ground and appraises the reduction in the power of light as it passes through the atmosphere suffering absorption and scattering[34] [35].

The AM0 is the standard spectrum for space application, since it represents the radiation distribution above the Earth's atmosphere, where the average irradiance is I=1366 W/m^2[33]. Due to the phenomena the radiation undergoes in the atmosphere, the solar spectrum of the radiation reaching the Earth's surface, known by AM1.5 spectrum, is not as uniform as the AM0's. The AM 1.5 spectrum is used to gauge the efficiency of solar cells. The integrated power of this spectrum is 1000 W/m^2 [6][36][37].

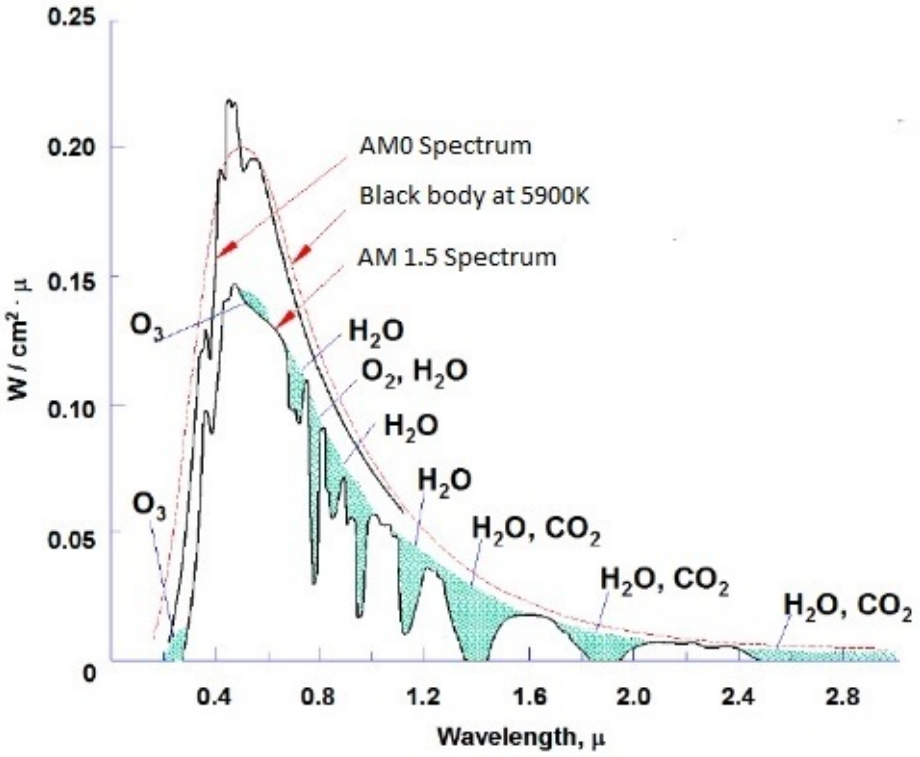

Figure 2.1: Solar irradiance above Earth's atmosphere (AM 0 spectrum) and at Sea Level (AM 1.5 spectrum). Image adapted from [1].

2.2 Introduction to semiconductors

2.2.1 Semiconductors

Photovoltaic solar cells are semiconductor diode structures[38]. Semiconductors can be i) crystallyne, having the elements stacked in a periodic pattern throughout the solid, ii) polycrystalline, being composed by several small crystals, called grains, arranged in random directions and adhering together at their boundaries and iii) amorphous, with no long-range lattice structure periodicity [39][6].

Semiconductors are solids that behave as quasi-metals in some situations and as insulators in others [3][37]. This occurs due to the existence of a moderate gap (up to a few electron volts) for electronic excitations in the energy distribution of electronic states of the semiconductor. At T=0K in a pure material (named intrinsic semiconductor) , there is a band of energy which is completely full, named valence band that is separated by the previously referred gap from the conduction band, which is empty [9]. If the electrons acquire enough energy, -the band gap energy-their transition from the valence band to the conduction band is possible and an electron-hole pair is created[6]. Therefore, these electrons and holes become free and are able to react to electric fields and concentration gradients that allow the unveiling of macroscopic currents [9].

Semiconductors can be classified as direct or indirect semiconductors. The maximum of the valence band and the minimum of the conduction band occur at the same momentum in direct semiconductors,

whereas for indirect semiconductors these values occur for different momentums. The absorption/emission of photons by electrons and consequent transitions are possible only in direct semiconductors. Transitions in the indirect gap semiconductors can only take place if a phonon is absorbed or emitted along with the photon, in order to have conservation of momentum. This particularity leads to a smaller absorption coefficient α, comparing to direct gap semiconductors[6] [37].

2.2.2 Defects and impurities

At room temperature and low temperatures, the properties of semiconductors are mostly affected by impurities and defects. Namely conductivity, due to the introduction of impurity/defect energy levels in the band gap[3]. The introduction of defects and impurities are used to control some electrical characteristics of the semiconductors[40].

Defects can be classified as point defects-deviations from the ideal lattice structure, that occur in a specific location, usually in one lattice point- and as extended defects-which are not confined to a specific lattice site.

The most important point defects are vacancies, missing atoms at an atomic position, and antisites that occur when an atom B of the lattice occupies the site of other atom, A. Vacancies are represented by V_A, where A is the missing atom and antisites by B_A.

Impurities are atoms that do not belong to the lattice of a semiconductor. When these are introduced deliberately into a semiconductor, the phenomenon is called doping. An impurity can be substitutional, when occupies the site of an atom of the lattice, or interstitial if it occupies an interstitial location in the lattice[41][42].

Defects and impurities can either be denominated as acceptors or donors. Donors give electrons to the conduction band and their centers become positively charged. An acceptor gives holes to the valence band, or, in other words, accepts electrons, and their center becomes negatively charged[42].

Donors donate electrons to the conduction band and conceive local energy levels just bellow it. As a result, the free electron density increases. Consequently, the Fermi level is shifted towards the conduction band. On the contrary, acceptors have less electrons than the host semiconductor, giving holes to the valence band and establishing energy levels just above this band. The density of holes is increased and, so, the Fermi level gets closer to the valence band.

As an example, for group IV semiconductors, it is common to replace some of its atoms by elements from group III, in this situation, a p-type semiconductor is obtained, or from group V, where a n-type semiconductor is created[6].

2.2.3 Passivation and compensation

Compensation occurs when the defects and/or impurities remain isolated from one another and electrons from donors recombine with holes from the acceptors.

When defects/impurities interact, a whole defect/impurity must be considered. In this situations, the most abundant defect/impurity is the one that determines the type of conductivity of the whole material.

The passivation of a donor or acceptor defect/impurity takes place when the whole defect does not present an electric activity, meaning that it does not establish a level in the band gap[3][41].

2.2.4 Photovoltaic effect

The photovoltaic effect is the phenomenon that allows the production of electricity from solar radiation in the solar cells[43]. The word itself describes the physical process: the conversion of absorbed light into electricity (from the words photo and voltaic)[37].

The photons coming from the sun that have an energy equal or higher than the semiconductor's bandgap are absorbed by the semiconductor's atoms and produce electron-hole pairs. Then, the photo-generated carriers are collected at opposite contacts.

The photon energy E_g is related to the wavelength λ according to the following relation:

$$\mathrm{E_{ph}} = \frac{\mathrm{hc}}{\lambda} \tag{2.1}$$

where h is the Planck's constant and c the speed of the light in vacuum[6][37].

2.2.5 Recombination

After the generation of an electron-hole pair due to external factors such as temperature or light-absorption, the system usually tends to move back to equilibrium, with recombination. Recombination is the opposite of electron-hole pair generation: an electron drops from the conduction band to the valence band, eliminating the valence-band hole[6][2].

There are several recombination mechanisms important to the operation of solar cells, namely Shockley-Read-Hall recombination, band-to-band recombination and Auger recombination illustrated in Fig. 2.2.

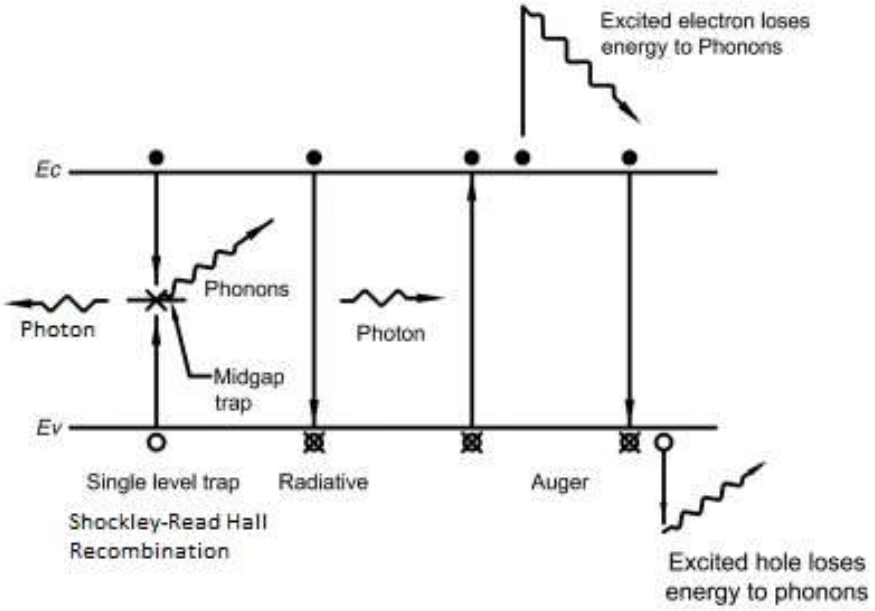

Figure 2.2: Recombination mechanisms in a solar cell. Image adapted from [2].

Shockley-Read-Hall recombination happens due to impurities/defects of the material. This recombination is not desirable for the good functioning of the solar cell. The impurities and defect centers in a semiconductor create allowable energy levels in the forbidden gap, known as trap levels. Trap energy levels closer to the mid of the band gap are very effective for recombination.[6]

This process has two-steps: the electron released from the conduction band is captured by a trap level. From the trap level, it moves to the valence band, annihilating a hole. The higher the defect density, the lower the lifetime of the carriers. The energy of the transitions can be released in the form of a photon or, as it is more often, in multiple phonons (single quantum of lattice vibration, which is equivalent to say thermal energy)[44][2].

Band-to-band recombination (or radiative recombination) is the reverse of the light absorption process. This type of recombination happens when an electron from the conduction band recombines with the hole directly in the valence band and releases the gap energy in the form of a photon. This is the most common recombination in direct band gap semiconductors.

The Auger recombination requires three particles to occur. The electron in the conduction band de-excites, recombining with a hole in the valence band and transfers its energy to a third particle that can be a electron or a hole. This third particle is subsequently excited to higher energy levels and gives off a series of phonons until it's energy returns to equilibrium energy-process of thermalization[44][3][6].

2.2.6 P-N junction

An p-n junction is formed by two semiconductors with opposite carrier type- a n-type semiconductor and a p-type semiconductor-in contact.

An homojunction is formed by two semiconductors of the same material and an heterojunction has two semiconductors of different materials. To explain the function of the p-n junction, the model of an homojunction will be used.

Homojunction at 0 bias-equilibrium

As two semiconductors of opposite carrier type are joined together, a concentration gradient exists between them. According to Fick's law, the charge carriers begin to diffuse to the region of opposite charge, where their concentration is lower[6]. Diffusion arises in the interface between the two semiconductors, because it is there where the concentration gradient is more significant. Electrons go to the p-side leaving the donors ionized, thus a static positive charge and holes go to the n-side, leaving acceptors ionized, meaning a static negative charge. The charge carriers recombine with their respective opposite charges and create a region with low charge carriers concentration, named the space charge region or depletion region, with a width W.

As a consequence , in the depletion region, an electric field pointing from the n-type region to the p-type region is created, the integration of this field is the built-in potential V_{bi}. The referred electric field will decrease the diffusion current because it creates a drift current with the opposite direction. As a result, it will be more difficult for the diffusion to happen as the value of the electric field increases and it becomes easier for the minority carriers of each side to go to the opposite region, which reduces recombination.

At a certain point, the drift current and the diffusion current are equal and an equilibrium is established [37][6][3][43].

Analyzing this process in terms of the band diagram is also possible. When the two-type semiconductors are apart from each other, (considering that they are of the same material) the top of the valence band and the minimum of the conduction band are the same. However, their Fermi levels are in different positions, considering that the semiconductors are of different conductivity types. The Fermi level is the thermodynamic work required to add one electron to the material body or by other words, the variation of free energy associated to the variation of the number of electrons[3][45].This quantity is much higher in the n-type semiconductor than in the p-type semiconductor, so the energy of the electrons reduces a

lot if they pass from the conduction band of the n-semiconductor to the empty states in the valence band of the p-type semiconductor.

As mentioned before, due to these transitions, an electric field arises and consequently the appearance of a potential barrier-the built-in potential- (as it is possible to see in the band diagram) which leads to the alignment of the Fermi level, that must be constant in all the semiconductor. This potential is the energy difference between the chemical potentials of the p-region and n-region. The electrons must overcome this barrier to pass from the n-region to p-region as illustrated in Fig. 2.3[3].

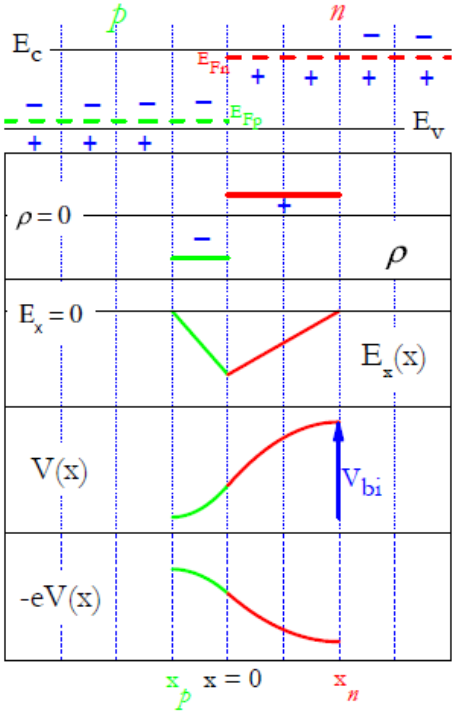

Figure 2.3: Electric characterization of the depletion region. From the top to the bottom: level diagram with the charge distribution in the depletion region, charge density in the junction, electric field $E_x(x)$, electric potential V(x), potential energy -eV(x) in the depletion region[3].

Homojunction at forward bias

When applying a voltage to the p-n junction, being the positive side connected to the p-type region, the holes are pushed in the direction of the n-type region and the electrons, that are connected to the negative side, are pushed to the p-type region. Hence, the majority carriers are ”forced” to diffuse more and the diffusion current increases.

The battery delivers more energy to the charges. Their energy allows them to pass the depletion region and recombine further from the junction, which reduces the depletion width. It would be expected that the drift current decreased since the space charge region decreased too (henceforth the electric field). Nonetheless, since the drift current is so small (because the quantity of minority carriers is small too), the reduction of the depletion region has a negligible effect on the drift current. Having this into account, the total current will go from the p-type region to the n-type region.

The electric field due to the external voltage has the opposite direction of the electric field of the junction. This reduces the net electric field of the junction and consequently there is a reduction in the potential barrier previously mentioned. The value of the potential difference is now given by V_{bi}-V_{ext} as illustrated in Fig. 2.4.[46][4]

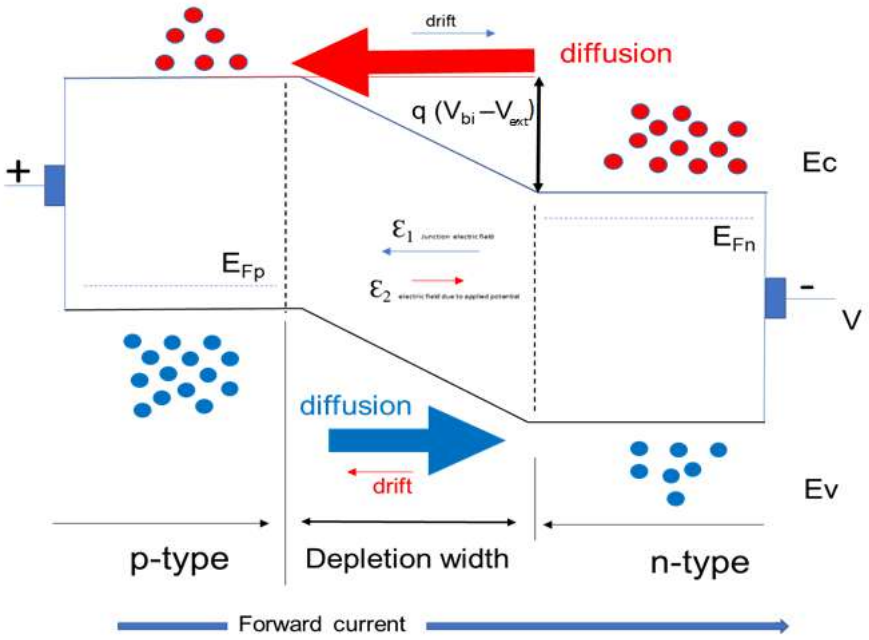

Figure 2.4: Band diagram of the p-n junction at forward bias. Image from [4].

Homojunction at reverse bias

When the solar cell works at reverse bias, a negative pole is connected to the p side and a positive pole is connected to the n side. This is the opposite situation of the forward bias: the electrons and holes are pulled to the contacts (of the region where they are majority carriers). In that event, the width of the depletion region increases and the electric field does too. The external electric field has the same direction as the electric field in the junction, thus, the net electric field(with the direction from the n-type region to the p-type region) increases and resultantly the potential barrier does too- it becomes V_{bi}+Vr (Vr is the applied external voltage) (see Fig. 2.5).

This electric field blocks the majority carriers to enter the opposite region (n-type region for the holes and p-type region for the electrons), or in other words, to diffuse. The diffusion current is reduced approximately to 0. The net current has the direction of the drift current. Nonetheless, this current is very small as it is due to minority carriers (which are not many).

If we increase the external voltage, the current will not increase. The minority carriers' velocity increases, not the quantity of carriers per unit time. The increase of the drift current (the net current), depends only on the generation of minority carriers in the depletion region[4][47].

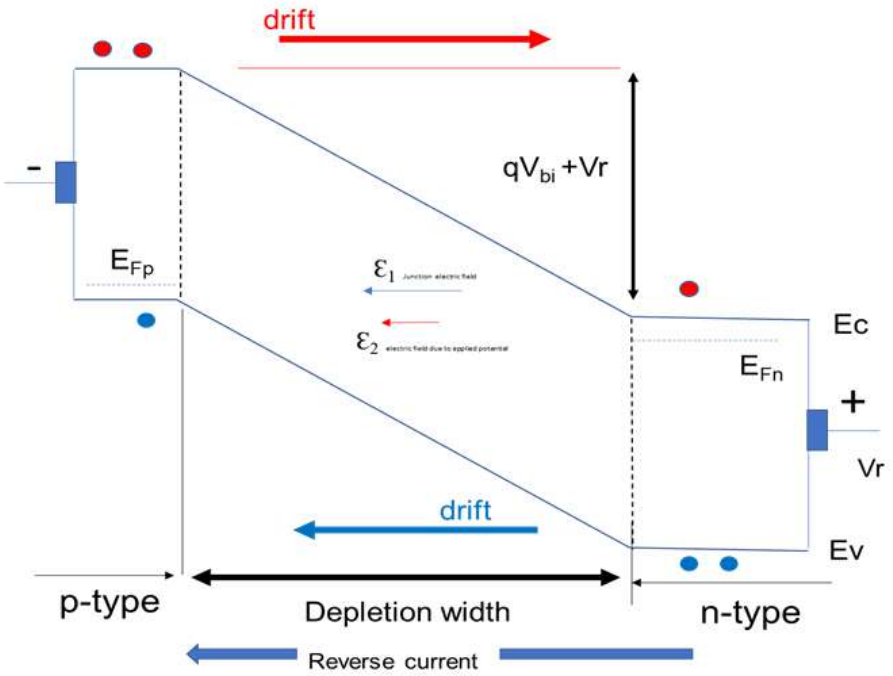

Figure 2.5: Band diagram of the p-n junction at reverse bias. Image from [4].

2.3 Solar cell

As referred in section 2.2.4 the photovoltaic effect is the most important working principle of solar cells. In a solar cell p-n junction, when this effect occurs, as the electron-hole pair is created, the electric field of the junction is responsible for the separation of charges that are then collected at opposite contacts and create a current. In this section, the behaviour of the solar cell at different bias will be analyzed[43].

2.3.1 Solar cell-p-n junction at reverse bias

In reverse bias, as previously discussed, the net electric field has the direction from the n-type region to the p-type region. The charges resulting from the photovoltaic effect will be separated (see Fig. 2.6) : the electrons go to the n-type region and the holes go to the p-type region, the generated current (photo current) has the opposite direction of the diffusion current, thus is considered a negative current[4][48].

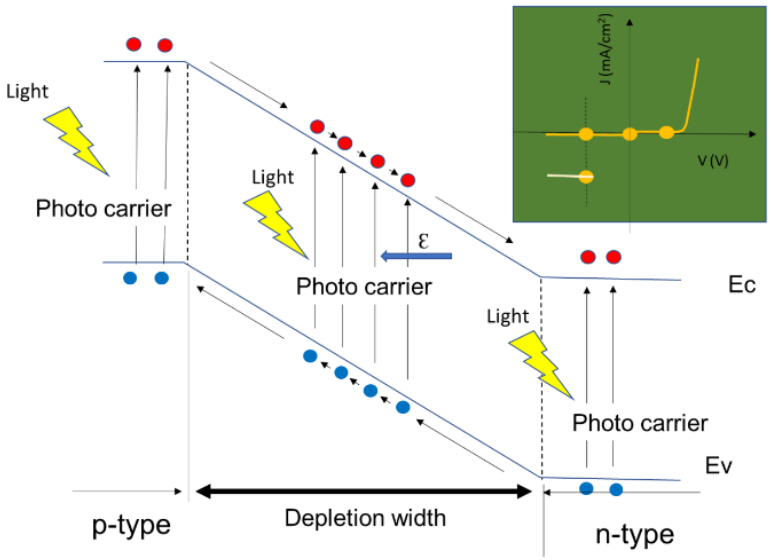

Figure 2.6: Band diagram of the p-n junction under illumination/solar cell and respective J-V curve representation before illumination (yellow curve) and after illumination for this voltage region (white curve) at reverse bias. Image from [4].

2.3.2 Solar cell-p-n junction at 0 bias

At 0 bias, without light, the net current would be 0. With light the net current has the opposite direction of the diffusion current, due to the emerging photo current[4].

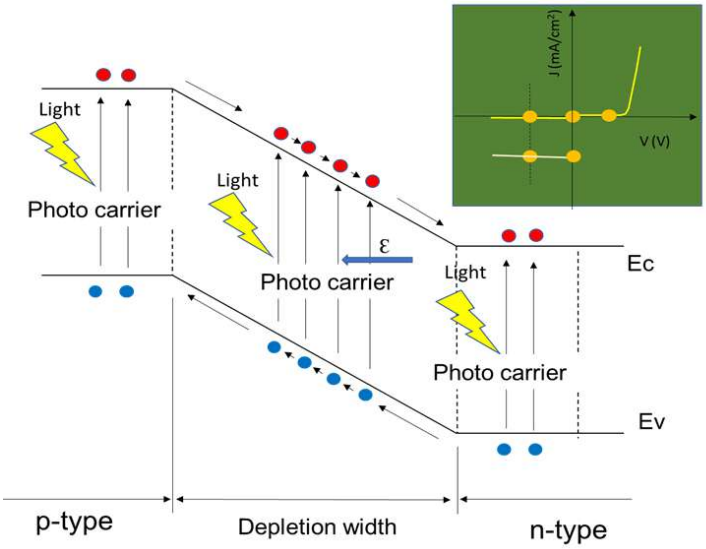

Figure 2.7: Band diagram of the p-n junction under illumination/solar cell and respective J-V curve representation before illumination (yellow curve) and after illumination until 0 bias. Image from [4].

2.3.3 Solar cell-p-n junction at forward bias

The net current before hitting light on the solar cell, at forward bias has the direction of the diffusion current. The photo current has the opposite direction. The net current will be the sum of this two currents: $I=I_D-I_L$. As the diffusion current increases (with increasing voltage) the total current decreases.(2.8) [4]

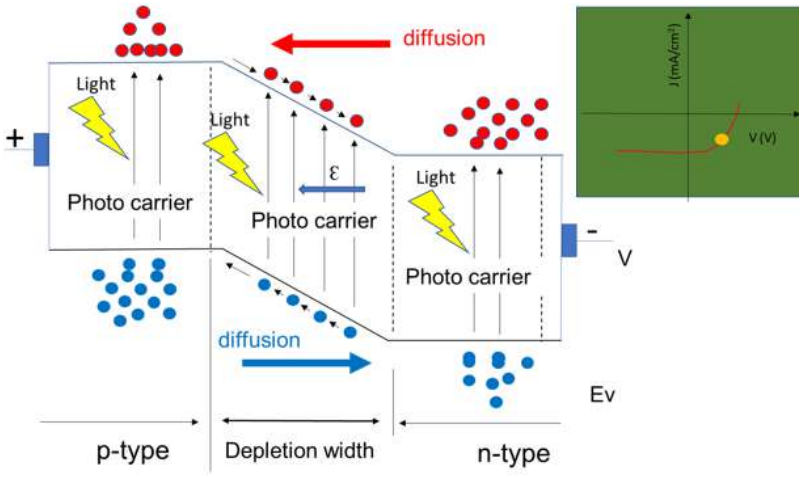

Figure 2.8: Band diagram of the p-n junction under illumination/solar cell and respective J-V curve representation after illumination. Image from [4].

In this regime, the charges have the opposite direction of the external applied voltage, thus it is possible to extract work from them and the cell works as a generator[3].

2.3.4 Heterojunction

As assigned before, heterojunctions are junctions formed by two different semiconductors.The usage of two different semiconductors enlarges the possibilities of design for solar cells since different materials have different bandgaps, refractive indices and other properties[49].

The band diagram of a typical p-n junction of the CIGS solar cells is represented in Fig. 2.9.

The descontinuities in both valence and conduction bands are a consequence of different properties in the materials of the device-namely the bandgap and the electron affinity. Optical and transport properties of the device are determined by these descontinuities[6].

Heterojunctions in solar cells are engineered in a way that favors the absorption in the absorber layer. Considering that the light generation of carriers decreases exponentially with penetration depth and that light is incident from the n-type side of the solar cell, it would be expected that the generation occurred in the n-type and not in the depletion region where a good collection would be ensured.

To enhance the absorption in the p-type region and respective collection two different approaches can be used: thinning the n-type material and using a n-type material with an enlarged band-gap energy. The latter transfers the generation profile directly into the junction in account of the large band-gap that prevents absorption in the n-type layer[9].

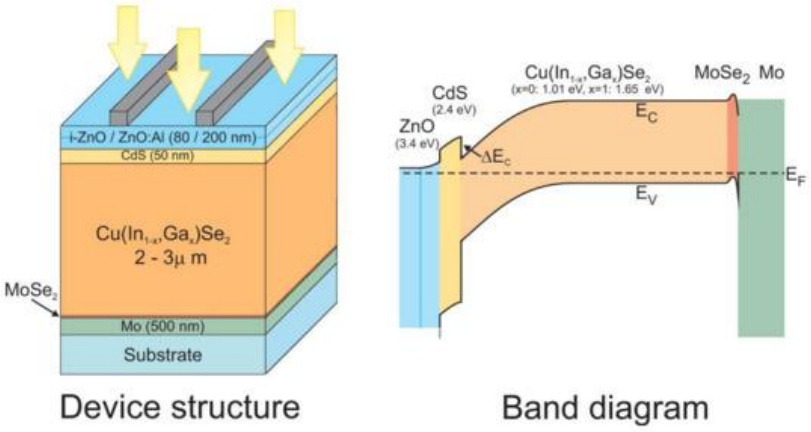

Figure 2.9: CIGS band diagram. From [5].

When joining together two semiconductors, it is very important to make sure that the interfaces are as free as possible of trap states in order to eliminate additional recombination and to prevent electrical charging due to preferred trapping of one carrier type. Recombination in the interface decreases the number of photogenerated carriers and consequently the photocurrent , which has a negative impact in the efficiency[50][6].

2.4 Electronic characteristics of a solar cell

2.4.1 I-V Curve and Equivalent Circuit

An ideal solar cell has the operation principle of a diode, formed by a semiconductor p-n junction, in parallel with a current source shown in Figure 2.10(a)[7][3].

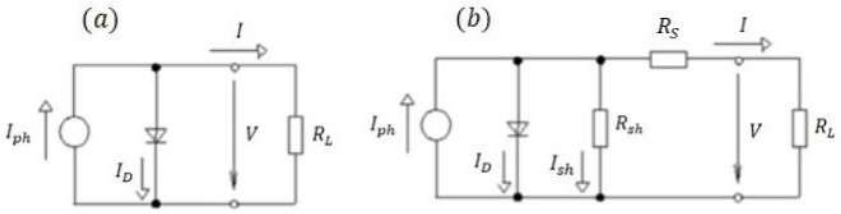

Figure 2.10: The equivalent circuit of (a) an ideal and (b)a real solar cell. From [6].

The current created in an ideal diode is given by the following expression:

$$\mathrm{I} = \mathrm{I_s}\left[\exp\left(\frac{\mathrm{eV}}{\mathrm{k_B T}}\right) - 1\right] \tag{2.2}$$

where I is the current flowing through the diode, $\mathrm{I_s}$ is the saturation or dark current which is a current that is measured in inverse polarization in the absence of light and consists of electrons and holes that are randomly generated thermally in the depletion region , e is the elementary charge, V is the voltage across the terminals of the diode, $\mathrm{k_B}$ is the Boltzman constant, and T is the temperature[7][3].

The emerging photocurrent in a solar cell shifts the curve of a diode in the direction of the negative currents, considering that this current has a negative direction.

When the cell is illuminated the ideal diode law becomes:

$$\mathrm{I} = \mathrm{I_s}\left[\exp\left(\frac{\mathrm{eV}}{\mathrm{k_B T}}\right) - 1\right] - \mathrm{I_L} \tag{2.3}$$

Being $\mathrm{I_L}$ the photocurrent[3].

The resultant I-V curve before and after illumination is shown in Fig. 2.11.

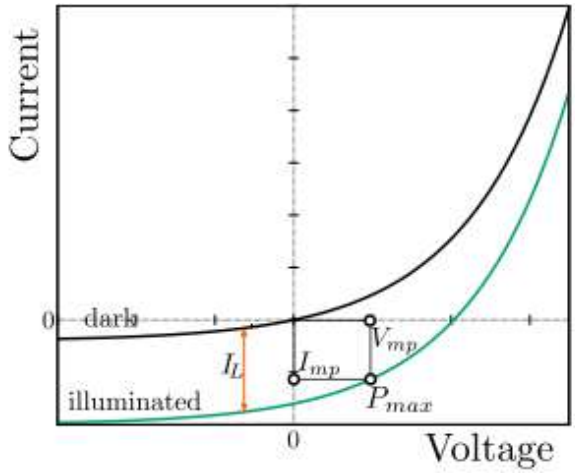

Figure 2.11: I-V curve of a solar cell before and after illumination with the principal parameters that can be extracted. From [7].

When classifying the PV characteristics of a solar cell, there are some parameters of great importance, namely:

Short circuit current is the maximum current obtained when the external applied voltage is zero (V=0, equivalent to a short circuit in the terminals of the cell), thus (in most cases) I_{SC} = -I_L.This means the current I_{SC} is directly proportional to the illumination available[7].

Open circuit voltage is obtained when the current flowing through the cell is zero, I=0. This voltage can be deduced from equation 2.3.

$$\mathrm{V_{OC}} = \frac{\mathrm{k_B T}}{\mathrm{e}} \ln\left(\frac{\mathrm{I_L}}{\mathrm{I_S}} + 1\right) \tag{2.4}$$

This value establishes the limit of the operation in which the junction can work as a solar cell. For this value, the extracted power becomes 0. The extracted power is $\mathrm{P} = \mathrm{V_{ext}} \times |\mathrm{I}|$ [3].

Maximum power, $\mathrm{P_{max}}$ is the maximum solar cell power output and it is verified in the point $(\mathrm{V_{mp}}, \mathrm{I_{mp}})$. As a result, it is determined as the product $\mathrm{P_{max}} = \mathrm{I_{mp}} \times \mathrm{V_{mp}}$ and graphically it is the biggest rectangle that can be obtained under the I-V curve, which in represented in Fig 2.11. [7]

After determining the parameters above described, it is possible to extract other values that help to assess the quality of a solar cell:

Fill Factor is the ratio between the peak power and the product of $\mathrm{V_{OC}}$ and $\mathrm{I_{SC}}$, considered the theoretical power[6][3].

$$\mathrm{FF} = \frac{\mathrm{V_{mp}} \cdot \mathrm{I_{mp}}}{\mathrm{V_{OC}} \cdot \mathrm{I_{SC}}} \tag{2.5}$$

Conversion efficiency of light into electric power of the cell. This parameter can be calculated as follows:

$$\eta = \frac{\mathrm{P_{out}}}{\mathrm{P_{in}}} = \frac{\mathrm{P_{max}}}{\mathrm{P_{in}}} = \frac{\mathrm{FF} \cdot \mathrm{V_{OC}} \cdot \mathrm{I_{SC}}}{\mathrm{P_{in}}} \tag{2.6}$$

Where $\mathrm{P_{out}}$ is the cell power output and $\mathrm{P_{in}}$ is the incident solar radiation power.

2.4.2 Parasitic resistive effects

For a real solar cell, the effect of parasitic resistances due to manufacturing defects must be considered. These resistances create additional current paths for the generated current.

Thus, in the circuit of a real solar cell we should include a shunt resistance, $\mathrm{R_{Sh}}$, and a series resistance, $\mathrm{R_S}$. This circuit is represented in Fig. 2.10(b).

The shunt resistance's magnitude is influenced by point defects in the p-n junction, leaking currents, for example along the edges of the solar cell, and impurities in the semiconductor lattice. Fitly, this resistance should be as high as possible because it creates an additional parasitic current path, reducing the overall current captured by $\mathrm{R_L}$. In terms of the parameters referred formerly, the shunt resistance affects largely the open-circuit voltage[8].

The series resistance is determined by the contact resistance of the metal-semiconductor interface, ohmic resistance in the metal contacts and semiconductors material. A high value of $\mathrm{R_S}$ is an obstacle

for the current that reaches the load, according to Ohm's law, the current is reduced by the R_S[6][37]. The series resistance influences the short-circuit current, reducing it with its increasing value[8].

The influence of these resistances in the I-V curve is represented in Fig. 2.12 and Fig. 2.13.

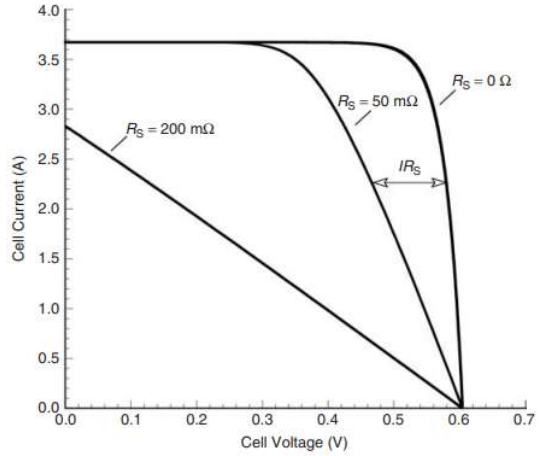

Figure 2.12: Effect of the series resistance on the current-voltage characteristic of a solar cell $R_{Sh} \rightarrow \infty$. From [8].

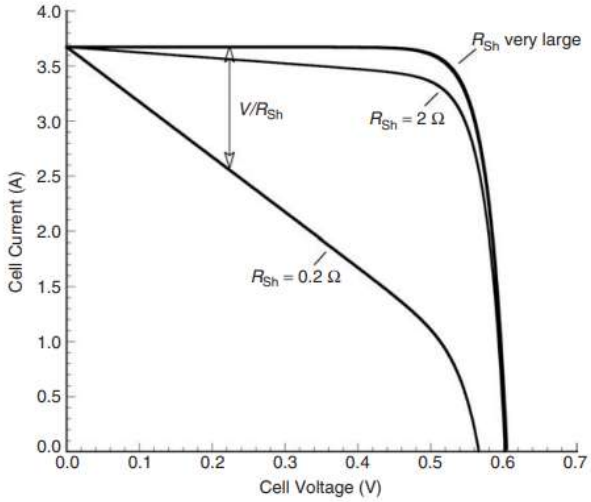

Figure 2.13: Effect of the shunt resistance on the current-voltage characteristic of a solar cell R_S=0. From [8].

2.4.3 External Quantum Efficiency (EQE)

EQE quantifies the conversion of an incident photon to an electron that is collected by the photovoltaic device and is generally a function of the photon wavelength[51].

$$\mathrm{EQE}(\lambda) = \frac{\Delta \mathrm{J/q}}{\Phi} = \frac{\#\text{collected electron} - \text{hole pairs}}{\#\text{incident photons}} \tag{2.7}$$

Where Φ is the total flux density in #/cm^{2}s and $\mathrm{J/q}$ is the current density over electric charge in #/cm^{2}s.

To acquire the EQE, a measurement of the current response at zero voltage for each wavelength is taken[9]. This characterization method can provide the information about the spectral regions that contribute to the photo-current generation and as a consequence may reveal loss mechanisms within the device stack[51] as it can be seen in Fig.2.14.

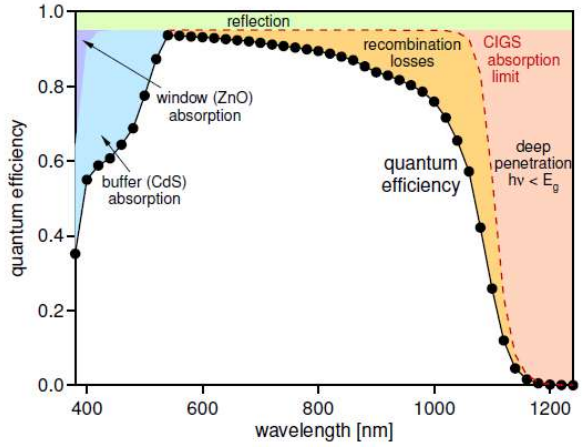

Figure 2.14: Simulation of an idealized CIGS EQE curve and involved loss mechanisms. From [9].

The EQE is the spectral response of the solar cell, thus the calculation of the J_{SC} of the cell under illumination can be calculated using it [51]:

$$\mathrm{J_{SC,EQE}} = \int \mathrm{q\,EQE}(\lambda)\,\mathrm{S}(\lambda)\,\mathrm{d}\lambda \tag{2.8}$$

where $\mathrm{S}(\lambda)$ is photons per second.

2.5 CIGS based thin-film solar cells

Commonly, thin-film solar cells are composed of the sequence of layers represented in Fig. 2.15: substrate, back contact, absorption layer, buffer layer, transparent conductive oxide (TCO) and an antireflective (ARC) layer[6].

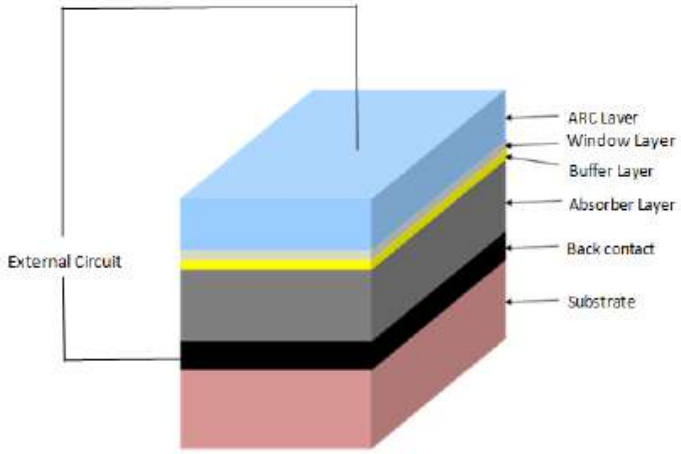

Figure 2.15: Typical structure of heterojunction solar cells. From [6].

Typical Cu(In,Ga)Se_2 (CIGS) thin-film solar cells use Cu(In,Ga)Se_2 as the absorber layer.This layer is a p-type semiconductor which in contact with a n-type material, whose layer is called buffer layer, forms a p-n junction . The most common and effective n-type material used in Cu(In,Ga)Se_2 based solar cells is a very thin layer of CdS (Cadmium Sulfide)[12].

A substrate for mechanical support is needed. The most efficient cells to date are grown on soda lime glass, but these can also be deposited on flexible substrates like polyimide films and stainless steel[52].

Above the buffer layer, at the front side, there is an intrinsic ZnO/ZnO:Al(AL-doped ZnO) bilayer window that transmits the light into the absorber and collects the electrons; for this reason it is also called front contact [12][7].

At the rear side, a molybdenum electrode collects the holes[7].

The thickness of the semiconductor layers altogether used in thin-film solar cell varies from 1.2 to $\sim$4 µm, which is very thin compared to the crystalline silicon at 170-200 µm[53].

Fig. 2.16 represents the typical structure of the CIGS solar cells. In this section these layers are going to be presented in more detail.

2.5.1 Soda-lime glass

Soda-lime glass (SLG) is a rigid flat substrate (allowing a conformal growth of the layers deposited on its surface) usually used in CIGS cells. It is a passive component in the device.

The substrate is required to be mechanically stable, which is the case for SLG, since it matches the thermal expansion coefficient with the deposited layers. This substrate is inert during the device fabrication and shows a good adhesion to the Mo back contact[6][54].

This layer's composition is 70% of SiO_2, 10% of CaO and 15% of Na_2O[55]. The presence of Na is important since it is known that Na diffuses from the soda lime glass to the CIGS layer at high tempera-

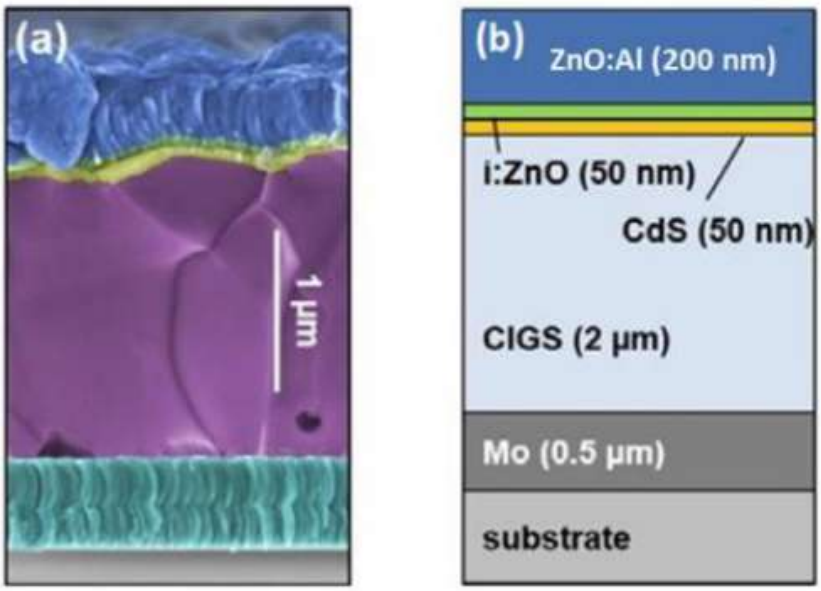

Figure 2.16: Typical structure of the CIGS solar cells: (a) Colored SEM image of a CIGSe cross-section. (b) Schematic of the standard structure of CIGS solar cell. From [10].

tures contributing to the improvement of its efficiency[12].

2.5.2 Mo back contact

Molybdenum is the most commonly used back contact in CIGS solar cells because it satisfies some important requirements such as chemical inertia towards Ga, In and Cu during the CIGS deposition and a high reflectance in the visible spectrum, which allows that some of the light not absorbed initially in the absorber layer is reflected back. A good adhesion of Mo films to the substrate and a low sheet resistivity, which are requirements for a good back contact, are highly dependent on the sputter conditions. The best results are obtained when doing a bilayer procedure, that results in a layer with a lower resistivity and other with a better adhesion to the substrate[54][6].

Mo is not chemically inert to selenium considering that it forms a $MoSe_2$ interfacial layer when reacting with it. This layer forms an ohmic contact with the CIGS layer, otherwise, the contact Mo/CIGS would form a Schottky barrier, creating resistive losses[56][6]. A factor that also contributes to the formation of this layer is the permeability of Mo for alkali elements. This allows the diffusion of Na from the soda-lime glass to the CIGS layer, which favors the formation of the $MoSe_2$ layer[12].

2.5.3 CIGS absorber layer

The absorber layer is a crucial layer in a solar cell, considering that it is the one responsible for absorbing the incident light, creating charge carriers that participate in the photocurrent.

It is formed by a p-type polycrystalline I-II-VI_2 semiconductor compound Cu(In,Ga)Se_2-constituted by Copper, Indium, Gallium and Selenium-with a high absorption coefficient of 10^{-5} cm^{-1}[7].

This semiconductor has a direct bandgap that can be changed to match the solar spectrum[11] . It can be tuned by varying the stoichometry of the compound. The best efficiency is reported in solar cells in which E_g is between 1.1 and 1.2 eV[7][6].

The chalcopyrite unit cell structure is a face-centered tetragonal structure[6] shown in Fig. 2.17.

The composition of the CIGS absorber layer is essential to determine its properties. In and Ga occupy the same atomic sites. As a consequence, they can substitute each other and their ratio is responsible for the value of the bandgap. The bandgap varies from 1.04eV for pure $CuInSe_2$ occupation to about 1.7eV for pure $CuGaSe_2$[11]. To quantify this quantity, the GGI ratio is used: [Ga]/([Ga]+[In]).

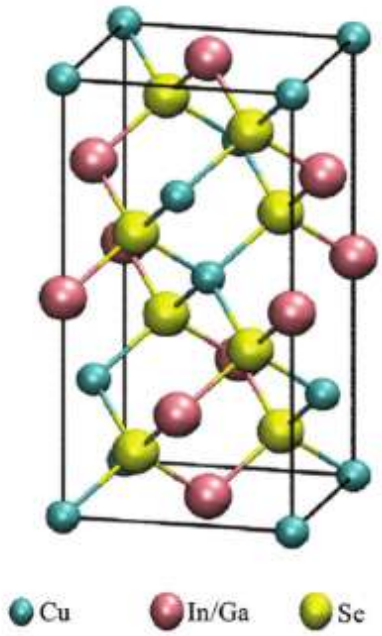

Figure 2.17: Unit cell of chalcopyrite $Cu(In,Ga)Se_2$. From [11].

To obtain the p-type conduction, the CIGS has a Cu-poor composition - [Cu]/([Ga]+[In])$<$1. The acceptor Cu vacancy V_{Cu}^{-}, the donor Cu substitution state (In_{Cu}^{2+} and Ga_{Cu}^{2+}) and the donor Se vacancy state (V_{Se}^{2+}), have a very low formation and form shallow states. The first two referred are strongly correlated and their proportion remains close to 2:1 forming a neutral pair. A small variation of this ratio is responsible for the p-type conductivity of the CIGS[12].

CIGS' properties are influenced by its growth and deposition conditions. Typically it is grown at temperatures between 450 °C and 600 °C[7].

2.5.4 CdS buffer layer

The CdS is a direct bandgap n-type semiconductor and it forms an heterojunction with the p-type CIGS. It has a bandgap of 2.4 eV, absorbing high-energy photons and preventing them from being absorbed in the absorber layer. This is disadvantageous because the photo-generated carriers in this layer do not contribute to the photocurrent due to the low carrier lifetime of the minority carriers.To reduce

the absorption of this layer, CdS films have a low thickness, which as a consequence, also reduces the resistance introduced into the system. [6]

The role of this layer is also to passivate the CIGS surface and therefore to reduce recombination losses and to protect the absorber surface during the sputtering of the window layer[12].

2.5.5 Window layer

In CIGS solar cells, the front contact is the ZnO window bi-layer composed by an intrinsic zinc oxide layer and an alluminum-doped zinc oxide layer- i-ZnO and ZnO:Al.

Intrinsic ZnO

This layer is intrinsically doped, which means that this compound deviates from its stoichiometric ratio, in this case there is a deficiency in oxygen. Oxygen vacancies are donors, as a consequence ZnO is intrinsically n-donor, permitting electron conduction in the conduction band[12]. The main role of this layer is to prevent a short-circuit between the two contacts since it has a high resistivity[7]. This layer also prevents the diffusion of Al into the absorber[11].

Al-doped ZnO

The front-contact is fabricated using a transparent conducting oxide (TCO). The aluminium doped zinc oxide is the oxide that is used (ZnO:Al)[11]. The addition of a MgI_2 coating on the surface of the AZO layer contributes to the reduction of light reflection at the air/ZnO:Al interface. The criteria to choose the compounds to use in the TCO are related to the transparency, conductivity to avoid resistive losses and compatibility to further processing[7].

Chapter 3

Alkali Element Doping in CIGS Thin-Film Solar Films

As mentioned before, doping is the intentional introduction of impurities in an intrinsic semiconductor to change its conductivity[41]. Alkali doping has been known to improve the efficiency of Cu(In,Ga)Se_2 solar cells[57]. Several explanations for this improvement exist, ranging from the passivation of defects at the p-type CIGS absorber surface or at grain boundaries, which reduces recombination, to the possibility of decreasing the buffer layer due to diffusion of donors to the CIGS surface[58][59].

3.1 Incorporation strategies of the alkali elements and its influence

The most commonly adopted alkali incorporation methods are: pre-deposition, co-evaporation and post-deposition. Pre-deposition consists on the diffusion of the alkali from an alkali-containing substrate. In the co-evaporation method the alkali element is evaporated during the absorber deposition. Post-deposition means that the absorber is deposited first and then annealed with the alkali element[58].

Pre-deposition incorporation

This type of incorporation arised from the unintentional diffusion of Na from a soda-lime glass (SLG) substrate during CIGS evaporation. This is a good Na doping method. However, for a large-scale SLG, the uniformity of the Na content is not sufficient and deteriorates the module efficiency.

To avoid this problem, some alternatives exist, such as:

- Depositing a thin layer of aluminum oxide (Al_2O_3) or silicon nitride (Si_3N_4) on SLG to block Na from diffusing into the CIGS absorber and distributing after Na through the sputtering of a Na containing

molybdenum (MoNa) back contact, acting as Na source.

- Depositing a NaF layer (a precursor layer) on the Mo back contact to ensure a sufficient supply of Na during the absorber deposition. The Na doping is controlled by the NaF thickness.

  Insufficient NaF amount results in low V_{OC} and FF and an excess leads to peeling-off problems during absorber deposition, so it is necessary to use an adequate thickness of this layer to get the results aimed.

The performance of these pre-deposition incorporation methods was compared and the NaF precursor sample showed the best performance with a substantially higher V_{OC} and FF than the other devices[60].

Co-evaporation incorporation

Co-evaporation is a technique that uses a reactor similar to the one presented in figure 3.1 [12].

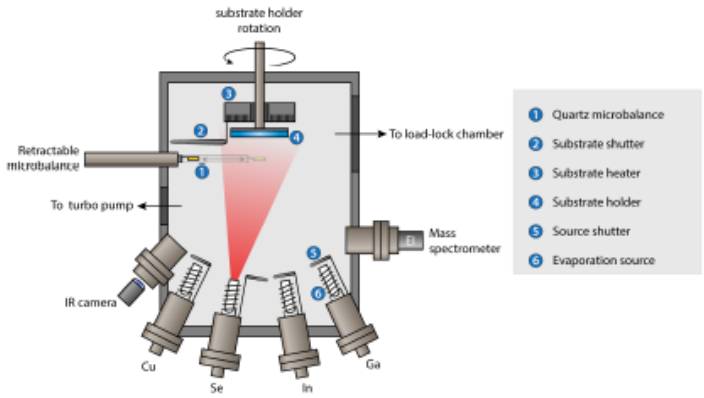

Figure 3.1: Schematics of the co-evaporation reactor used for the deposition of the CIGS layer. From [12].

In this reactor the Cu,In,Ga and Se elements are evaporated on the substrate in a high vacuum chamber. The substrate is placed at the top of the chamber on a heater, that controls its temperature along with a thermocouple (placed behind the substrate). The substrate is facing-down in a rotating substrate holder and has next to it a shutter[13].

Each pure element (Cu,In,Ga and Se) is placed in a crucible inside an evaporation source (Knudsen cell) and is evaporated at its saturation vapor pressure. The rate of the evaporation of each element is controlled by the power of each source heater.

The substrate shutter and the evaporation source shutters can be closed or opened to control the deposition[13][12].

Depending upon the number of growth stages, growth processes can be denominated[11]:

- Single stage processes- Only imply one evaporation rate for each element and Cu is deficient throughout the entire process.

- Two-stage process- It has two stages of deposition, one using a Cu-rich growth and the other using a Cu-poor growth. This is obtained controlling the Cu flux.

- Three stage process- This process is described in Fig.3.2.

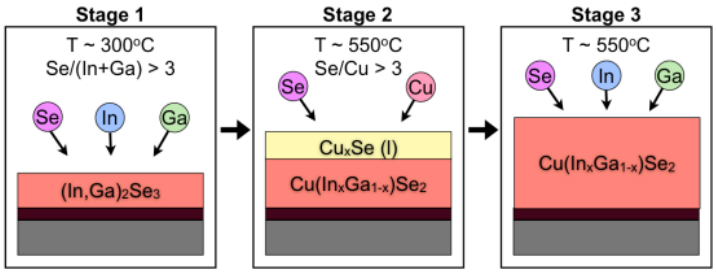

Figure 3.2: Schematic showing the three-stage process used to grow high efficiency CIGS solar cells by vacuum co-evaporation. Stage 1- The substrate is heated up to over 300 °C. After, the In, Ga and Se are released into the chamber. Consequently, a thick layer of $(In,Ga)_2Se_3$ is grown as a precursor. Stage 2- In the second stage the In and Ga flux is replaced with Cu as the temperature is heated up to over 550 °C. Stage 3- The third stage is characterized by the deposition of In and Ga. A constant Se flux is supplied in all the three stages. From [13].

As mentioned in [58] CIGS absorbers were prepared on a PI(polyimide) substrate using the three-stage co-evaporation process and Na was incorporated by co-evaporation in each stage. It was found that incorporating Na during the first and second stages deteriorates the CIGS crystallinity.

In contrast, at the third stage, the crystallinity is only slightly affected in comparison to a free-Na sample. The performance of this cell was the best, which can be explained by the small influence Na has on crystallinity and the passivation of the defects it does at the film surface and grain boundaries.

Excellent crystallinity and passivated surface and grain boundaries contribute to a larger free carrier concentration[58].

Post-deposition incorporation

Post-deposition treatment involves the incorporation of alkali elements (Na, K, Rb, Cs) into the CIGS layer after the deposition of the absorber. This process passivates defects without affecting the semiconductor crystallinity, improving the electric properties of the solar cell[58].

The PDT treatment most used to the date is the evaporation of alkali-fluorides in vacuum right after the deposition of the CIGS thin-film[18][15].

It was also performed using the spin-coating technique[22][18]. The spin-coating technique starts with the dilution of the material to be deposited in a solvent. The solution is subsequently dispensed in the center of the substrate surface-the absorber surface in this situation. The substrate is then rapidly rotated to produce uniform films. The centrifugal force of the rotation causes the liquid to spread into a film and coat the surface. After this process, the sample must be annealed. The solvent is removed partly during the spinning process due to evaporation and partly by subsequent baking at elevated

temperatures[61] [62]. The key process parameters of this technique are dispensed volume, concentration, viscosity of the solution and spinning speed and time[63]. The apparatus used in this treatment can be seen in Fig. 3.3.

The major advantages of this technique are the possibility of controlling the film thickness, uniformity, low operation cost and rapidness[63].

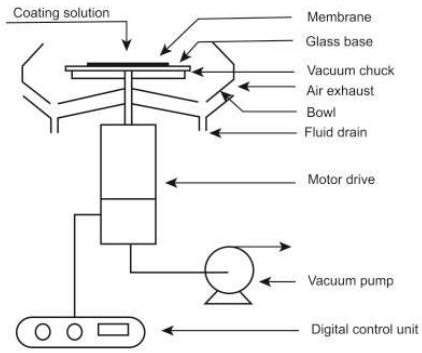

Figure 3.3: Schematic illustration of the spin-coating apparatus. From [14].

3.2 Effects of light and heavy alkali

Alkali elements such as sodium (Na), lithium (Li), potassium (K), rubidium (Rb), and Cesium (Cs) are the most common alkalis used to boost cell efficiencies of CIGS thin-film solar cells. Due to their electronic configuration, density and reactivity Li and Na are considered light alkali, whereas K, Rb and Cs are refered as heavier alkali. [15][64]

3.2.1 Effect of Na

Nowadays it is recognized that the presence of Na in the Cu(In,Ga)Se_2 absorber is necessary to attain reasonable efficiencies[64]. There is a broad consensus that attributes an increase in the V_{OC} and FF , and as a consequence, an increase of the efficiency, to the incorporation of Na.

In fact, there are some changes in CIGS macroscopic properties observed due to this alkali, namely, an enhanced carrier density, the Ga diffusion towards the Mo back contact enhancing the Ga gradient ([Ga]/[Ga+In]) and changes in crystallographic orientation. These phenomena are depicted in Fig. 3.4.

The increased p-type conductivity associated to Na incorporation is attributed to the enhanced carrier concentration, for which the exact physical mechanism behind is still in debate. There are arguments in favor of the passivation of donor defects in the GBs, several mechanisms are proposed: in the CIGS bulk, Na may substitute In_{Cu}^{2+} (donor) to form neutral defects Na_{Cu}[4], Na^{+} at the film surface might absorb O_2 to transform Se vacancy (V_{Se}), a donor, into O_{Se}, a neutral defect [58], as an alternate interpretation it is suggested that Na is capable of decomposing ($2V_{Cu}^{-}$ + In_{Cu}^{2+}) the neutral defect pairs by replacing In_{Cu}^{2+}, a donor defect, for Na_{Cu} in In-rich films, increasing the shallow acceptor defects, V_{Cu} that do

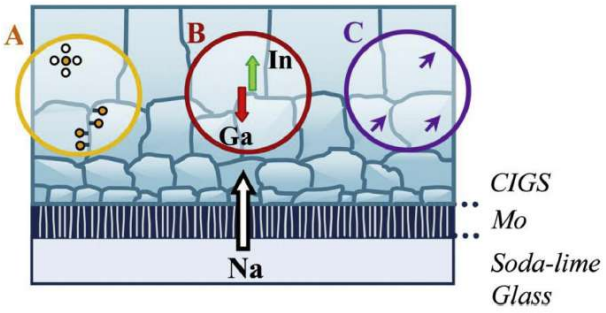

Figure 3.4: The observed changes of CIGS material properties due to Na incorporation. In this situation Na diffuses from the SLG. A-Enhanced carrier density. B-Ga diffusion towards the Mo back contact. C-Changes in cristallographic orientation. From [15].

not form any defect complex[58][15]. As a result of these reactions, the donor concentration could decrease and the difference N_A-N_D increase, reducing the compensation level. The number of holes would increase and consequently the built-in voltage too, contributing to higher values of V_{OC}[58][4][60].

Evidence of the presence of Na in the CIGS grain interiors with a concentration of 13 to 150 ppm exists. Initially, it was thought that Na affected the electrical performance due to the formation of new acceptor defects, but recent findings showed that Na_{In} and Na_{Ga} antisites are energetically unfavorable. The elimination of In_{Cu}^{2+} and Ga_{Cu}^{2+} by Na was also found to be unfeasible due to kinetic limitations. The reason for the enhancement of carrier concentration in CIGS grains remains unclear[15].

Concerning the relation between Na dopants and the grain size of the CIGS layer, no conclusions were taken since some studies report that grain size is enlarged, others claim that Na reduces the grain size and some reports even state that there is no relation between Na dopants and grain size[15].

All these contradictory results may be connected to the different growth processes used for the deposition of CIGS[60].

3.2.2 Effects of KF-PDT

Potassium has shown positive effects when incorporated in CIGS through PDT, leading to higher efficiencies than those attained just with the Na treatment[15]. It was also observed that when both Na and K are incorporated in the CIGS absorber better efficiencies are obtained[22].

It is disclosed that KF-PDT can modify the absorber's surface, leaving it Cu- and Ga- depleted[15]. However, in [65] it is reported that the amount of Ga increased at the very-near-surface region, suggesting that Ga atoms diffuse from the bulk to the very-near-surface region during KF deposition. It is also thought that potassium incorporated through evaporation (from a KF source) accumulates at the surface and forms a K-In-Se compound responsible for the widening of the bandgap at the absorber surface and passivation of defects[64][15].

Another finding is that KF-PDT facilitates Cd diffusion into the Cu-deficient CIGS surface, occupying the V_{Cu}^{-} acceptors and forming Cd_{Cu} donors. Thus, a surface inversion occurs and a strong buried

p-n homojunction is formed. Therefore, it is not necessary to use a thick buffer layer to form a high quality CIGS/CdS heterojunction. This possibility benefits the short wavelength absorption and as a result increases the J_{SC}[58].

When Na is also present, K pushes Na atoms away from grain boundaries and segregates along them while Na diffuses into the grain interior. This is the called ion-exchange mechanism and has been studied for further understanding.

Although the underlying mechanisms are not fully understood, the benefits proposed for this treatment are the increased hole concentration, the enhanced minority carrier lifetime which could be a reason for the reduction in the V_{OC} loss [65], a decreasing of the concentration of traps or deep levels and grain boundaries passivation[15].

3.2.3 Effects of Cs-PDT

The benefits that the KF-PDT brought to the solar cells have motivated researchers to further explore other heavy alkali elements such as Cs. The highest efficiency was attained with a CsF-PDT, and its value was 23.35%. [21] In [58], samples subjected to a CsF-PDT, showed a clearly higher V_{OC} and FF than samples without any PDT, while the J_{SC} presented little change (due to the non-optimization of the CdS thickness). The doping level of CsF is mentioned to have a significant role in improving the V_{OC} and FF, and thus the efficiency [58]. These results have been obtained in several studies[16][66][67]. The reasons behind these benefits are still very unclear, but some hypothesis have been proposed[15].

It is reported that Cs is present at the buffer/absorber heterointerface in the form of $CsInSe_2$, which contributes to shifting down the valence band of the absorber surface, reducing the recombination at the absorber-buffer interface and to a conduction band-upward[15][67]. On the other hand, it is claimed that this layer also forms at the grain boundaries after the CsF-PDT, where GBs recombination can also be supressed[16]. In [64], the effect on the surface electronic structure of the CIGS differed with absorber or type of heavy alkali PDT, although the improvement of the solar cell efficiency was the same, which with several studies lead to the conclusion that the main effect of PDT with heavy alkali was on the bulk recombination (non-radiative recombination), reducing it, by decreasing the number of charged defects at grain boundaries.

A diffusion process of Cs in the grain boundaries was suggested. It is illustrated in Fig. 3.5. In this process, Cs with a larger ionic radius might not replace the Cu vacancies as Na does. A strong chemical force of Cs to react with In and Se elements repels Cu, leaving a Cu-depletion region at grain boundaries and near-surface of the CIGS absorber. The formation of the $CsInSe_2$ compound could be explained this way[16]. The thickness of this layer (controlled by the CsF doping) and the Ga concentration are important to control the conduction band upward, which, if too high, promotes a barrier that blocks the photogenerated electrons , resulting in a negative effect on the device performance (JV distortion)[16][66]. It is mentioned that CsF-PDT will have a better impact on devices with a high Ga content on the absorber surface[66].

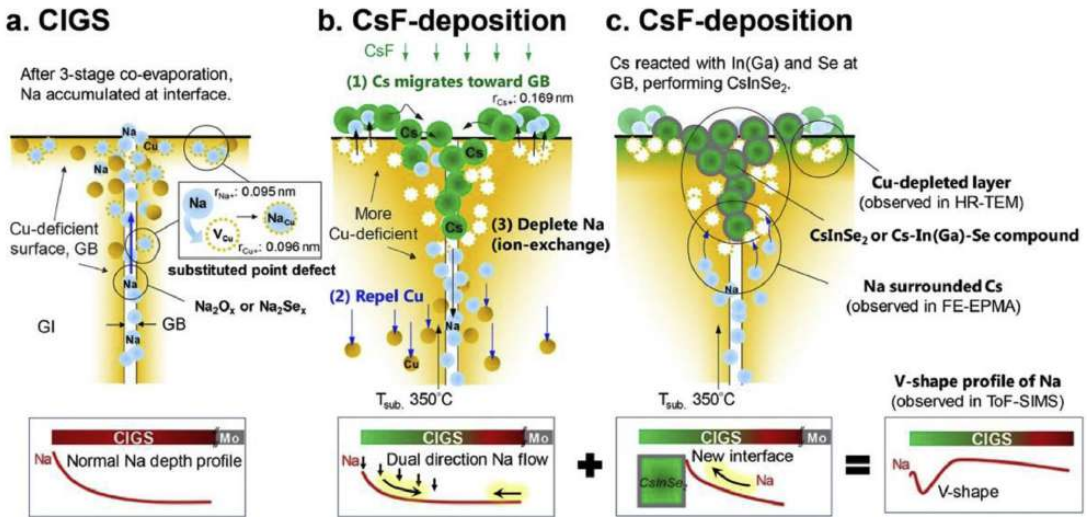

Figure 3.5: Schematic diagrams of Cs diffusion pathways and possible mechanisms in CIGS absorbers evaporated on Na-contained SLG substrates under different situations: (a)without CsF-PDT, (b) and (c) with CsF-PDT.From [16].

Contrary to [64], other studies suggest that Cs atoms not only distribute at the grain boundaries, but also enter the interior of the grains, where they can passivate donor defects and increase the concentration of holes and the lifetime of minority carriers. An excessive CsF doping is said to increase the Cs atoms entering in the CIGS grains leading to a large change in the texture of the film and to its phase transition, where some defects may act as recombination centers, thereby deteriorating the performance of the device[67].

It was suggested that the primary benefits of the Cs-PDT mainly include the increased hole concentration and the passivation of deep-level donor like defects and deep-level acceptor like defects[15].

Chapter 4

Light, heat and heat-light soaking

4.1 Light soaking

An essential characterization step for any photovoltaic technology is the device performance under extended duration illumination-light soaking-, since light exposure can produce a variety of effects that influence the performance of the solar cell and its stability. [26]

CIGS solar cells exhibit metastable performance changes under light soaking (LS), which can be beneficial or detrimental depending on the properties of the cell itself[68]. The behaviour of the cell has a great dependence with the buffer layer used, given that, usually , CIGS devices with CdS buffer are less sensitive to LS than devices with Zn(O, S, OH)$_x$ buffers[69].

The open-circuit voltages of CIGS solar cells may improve by several percent with illumination over periods ranging from minutes to hours at forward bias conditions (open-circuit voltage mainly). The magnitude of the improvement depends on device details[26]. In study [70], after several hours of light soaking at 20mW/cm^2, p-doping levels increased and the junction capacitance showed a decreased space-charge region width, indicating reduced recombination losses in the SCR of CIGS solar cells. Consequently, V_{OC} increased. In [71], a V_{OC} increase of at least 25mV was registered in CIGS solar cells with Zn(O,S)/(Zn,Mg)O buffer system, which was attributed to a reduction of the amplitudes of electrostatic fluctuations in the SCR after 30 min of illumination at 100mW/cm^2 and 1 week in the dark. In the same article, a second benefit of the LS treatment was the increase of electron-diffusion lengths for various CIGS/buffer layer combinations, namely for CdS buffer layers it increased almost twice. It was hypothesized that light illumination might have lead to the partial occupation of donor states/emptying of acceptor states, reducing the trapping of free charge carriers, which would increase the electron lifetime and consequently the diffusion length[71].

On the other hand, other experiments showed different behaviours of CIGS cells (with a NaF pre-deposited layer) with different minority carrier lifetimes (τ_n) . Cells with long τ_n lost V_{OC} and FF upon LS, whereas cells with short τ_n lost less or even gain V_{OC} and FF. The light-induced increase in the p-

doping level in the CIGS absorber is mentioned to be a possible explanation to the observed behaviour. LS is also claimed to be responsible for the transportation of Na from the back of the CIGS absorber towards the CIGS/CdS interface which may contribute to the LS effects observed. The electrical potential difference across the CIGS absorber generated by illumination might drive to this transportation[68].

Not many studies are done on the behaviour of alkali treated CIGS cells under LS. In [17] no changes in the basic solar cell parameters after LS under 1 sun illumination for 30 minutes were seen in NaF-PDT CIGS solar cells[17]. In [29], subjecting a KF-PDT CIGS solar cell to LS for 30 minutes under 1 sun illumination did not alter its initial performance significantly. Both treated and non-treated cells showed a slight-to-no decrease in net doping concentration, resulting in a slight increase of the SCR. Significant changes in the solar cell parameters occurred when LS was done together with HS. In contrast, LS in [72] resulted in a slightly improved efficiency, although it was not considered significant. Metastable holes caused a considerable increase in ionized acceptor concentration, which was too high as it led to a slight decrease in J_{SC}. This decrease was due to the thinner depletion layer and shorter minority carrier lifetime.

More detailed investigations display a wavelength dependence of the effects of LS. ”Red” light absorbed primarily in the CIGS absorber layer, generates different effects than ”blue” light that may be absorbed in the CdS buffer layer. The site in these layers where light is absorbed also has an influence on the subsequent effect. Light soaking with white light may produce an overall benign effect due to a balance of beneficial and detrimental effects.

These outcomes are proposed to have origin in the amphoteric Se-Cu divacancy complex, which is converted between donor and acceptor states by light absorption. Nonetheless there is still room for improvement in the understanding of this phenomenon[15].

4.2 Heat soaking

In addition to light exposure, the impact of heat exposure on solar cells is also crucial to evaluate. However, compared to light soaking, less attention has been given to heat soaking, and fewer studies have focused on the heat treatment of solar cells.

These are important since they can give us further information on to what extend CIGS is able to withstand critical environment conditions and also to understand which are the best annealing temperatures for tandem solar cells, in which CIGS is used as a bottom cell. Both exposure time and temperature have a large influence in the efficiency changes in CIGS solar cells[73]. The effect of heat treatment on CdS/CIGS interfaces in air and various atmospheres has been studied ([27] and therein).

Simulations were also performed on CIGS thin-film solar cells and it was predicted that from 25 °C to 70 °C a degradation of the V_{OC} and consequently the efficiency of CIGS solar cells would occur[74].

Cumulative heat soaking in air environment in the range of 150–300 °C and for a period of 30 seconds to 600 seconds was done in CIGSSe modules with a CdS buffer layer. The main observations and

conclusions were:

- Efficiency reduction after exposure to 300 °C for 30 seconds was limited to 2%-3%, while in the cases of 300 seconds and 600 seconds, it decreased by 29% and 48% respectively.
- Above 225 °C and for an exposure time equal or larger than 300 s there was the formation of a barrier that was visible in the J-V curves and became more evident with the increase of the exposure temperature. This barrier prevented the electrons extraction. The migration of Alluminium atoms from the front contact (ZnO:Al), creating trap points that contributed to recombination was the reason given for the occurrence of this barrier.
- Up to 225 °C the CIGSSe performance was not affected by the heat soaking treatment[73].

Other studies that used shorter exposure times obtained different results. In [27], a CIGS solar cell with a CdS buffer layer was annealed for only 1 minute at 200 °C, resulting in a higher efficiency of about 0.6% compared to an unannealed cell. The increase in J_{SC}, possibly due to improved optical transmittance of the CdS/glass at short wavelengths, justified this enhancement. This treatment was also suggested to eliminate recombination centers at the p-n junction.

Information on the behavior of alkali-treated solar cells subjected to heat treatment is scarce. In [30] a Cesium Fluoride (CsF)-treated CIGS solar cell was subjected to a heat-light soaking treatment and after to a heat-soaking treatment at 130 °C for 30 minutes. After the heat treatment, the V_{OC} and FF decreased and the J_{SC} and Efficiency increased[30]. A similar behaviour was reported on CsF-treated solar cells, where Heat-Soaking (at 130 °C for 5 minutes) was performed after a Heat-Bias Soaking (HBS) treatment. Heat soaking caused an increase in the SCR and a decrease in carrier concentration, resulting in a reduction of the J_{SC} loss previously observed after the HBS.[75].

In [72], KF-treated CIGS solar cells underwent dark heating for 100 hours at 90 °C, causing a significant decrease in the number of carriers, which resulted in a reduction of V_{OC} and FF. Consequently, an efficiency decrease of approximately 0.5% was reported.

Conversely, in [29], a KF-treated CIGS solar cell was subjected to a heat soaking treatment at 130 °C for 30 minutes, and no significant changes were observed compared to the initial cell performance. The same result was reported in [17], where NaF-treated CIGS solar cells underwent HS at 130 °C for 20 minutes. However, these samples were not subjected to a heat-light soaking treatment before.

4.3 Heat-light soaking

CIGS solar cells react to heat and to light exposure, as it was described in the latest sections. The combination of light and heat, called heat-light soaking, was also applied to these cells in order to achieve higher efficiencies, given the effects that heat and light may have separately.

Generally the effects of HLS are overall similar to the ones caused by LS, with an increase in V_{OC} and

net doping density. The most common behaviour of the short circuit current is its decrease which varies with the alkali that was used in the PDT. This decline in the current density is related to the reduction of the space-charge region and diminished carrier collection[30] [76]

HLS is more benefic in alkali-treated solar cells, as a result, most studies about HLS are done in CIGS treated cells. Although it has also benefits in non-treated cells, the effects are not as noticeable as in the treated cells or as beneficial as expected. [77] [30][28][29][76].

To get an improved efficiency after the heat-light soaking treatment, the ionized acceptor concentration should be optimized by controlling the light illuminance, heating temperature and heating time.

In [72] CIGS solar cells with KF-PDT had their conversion efficiency increased due to increasing V_{OC} and FF. The current density remained practically constant in this study. The best efficiency, 21.4% was achieved after 400h at 90 °C of HLS and an increasing hole concentration was verified. Passivation of recombination centers at the CdS/CIGS interface was suggested as a possible reason for these results.

On the other hand, HLS at 130 °C for 30 minutes had a different impact on the NaF-treated cells in [17], since the J_{SC} did not remain constant, instead it decreased. Although the efficiency increased with increased open-circuit voltage possibly caused by an increased net acceptor concentration.

SIMS depth profiles allowed to find changes after the HLS treatment in the distribution of the elements in the cell. The movement of the K and Na ions specially towards the CIGS surface region lead the authors to suggest that the ions were shifted by the photo-induced electric field. This redistribution may have eliminated the donor-like defects in CIGS absorber, resulting in the measured increase in net hole concentration. A scheme with the proposed mechanism is represented in Fig. 4.1

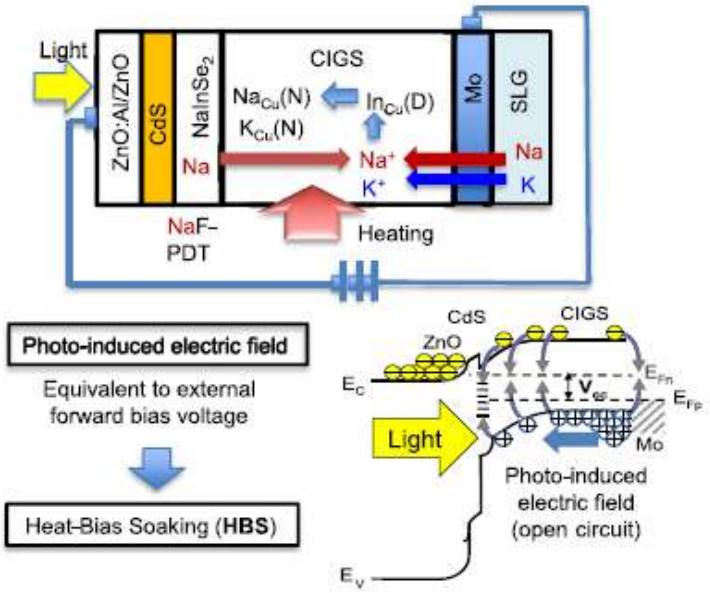

Figure 4.1: Possible mechanism of HLS effects for NaF-treated CIGS cells. The thermally activated alkali atoms (Na and K) may substitute for In and/or Ga at the Cu sites under photo-induced electric field, resulting in the increased net hole concentration, and thereby increasing the V_{OC}. From [17].

It was shown that the higher the atomic radius of the alkali used to the PDT, the higher the increased

carrier concentration, therefore more effective the HLS treatment. HLS showed results when the separate process (heat or light soaking) did not have any effect[77].

Chapter 5

Experimental Methods

5.1 Basic Principles of Magnetron Sputtering

Magnetron Sputtering is a high-rate vacuum physical vapor deposition (PVD) technique[6]. A physical vapor deposition technique is a process in which the material goes from a condensed phase (the target in our case) to a vapor phase and then back to a thin-film condensed phase[78].

Inert gases (the most commonly used is Argon) and reactive gases are supplied by a gas inlet. These will later form a plasma composed of neutral and ionized inert elements, electrons and photons. An external energy source, (for example a Radio Frequency power source or a DC source), is necessary to keep the plasma active.

Magnetron sputtering uses magnets behind the negative cathode to confine electrons over the negatively charged target material so they are not free to bombard the substrate, allowing for faster deposition rates.

The positive ions of the inert gas (in our case Ar^+) are attracted to the negatively biased target with large kinetic energies, resulting in their impact in the target and subsequent erosion. The erosion of the target allows that its atoms are free in the plasma and are then deposited in the substract[6][79].

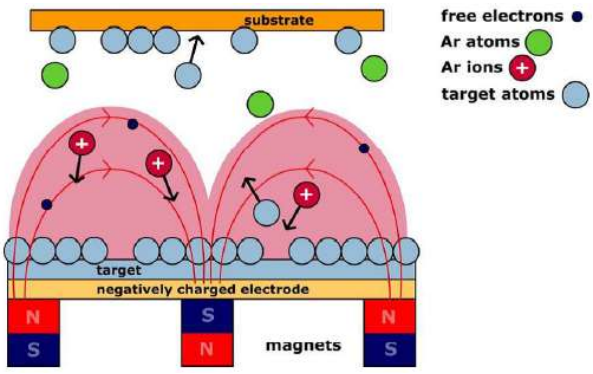

Figure 5.1: Schematic of the magnetron sputtering process. The impact of the Ar^+ ions in the target causes its erosion and subsequent deposition of its atoms onto the substrate[6].

5.2 Cells fabrication

The results presented are the outcome of measurements performed on the solar cells fabricated by Ishwor Khatri, Marie Curie fellow at the Laboratory for Nanostructured solar cells (LaNaSC). A small summary of the method used will be here described.

5.2.1 CIGS deposition

CIGS thin-films were deposited on molybdenum (Mo)-coated glass substrates (5 cm × 5 cm × 1 mm). The technique used for its deposition was pulsed hybrid reactive magnetron sputtering (PHRMS), developed by Instituto de Micro y Nanotecnologia and International Nanotechnology Laboratory. Its main advantage is the possibility of having a precise control of the selenium (Se) amount using a periodic pulsing of the selenium source[80]. Before being deposited onto the substrate, Se passes through a high-temperature cracker stage which allows to break large Se molecules into smaller ones, increasing the reactivity of the Se species on the deposition surface[18][54].

The deposition system used is STAR (Sputtering for Advanced Research) [81].

To attain a favourable Ga grading, the CIGS thin-films were deposited using a two-step deposition process. In the first stage, a slightly Cu-rich ($Cu_{0.50}In_{0.35}Ga_{0.15}$) target was used while evaporating Se in pulses using 1s period and 100 ms duty cycle (0.1s ON and 0.9s OFF). During $\sim$ 80 minutes of deposition, a Cu-rich CIGS layer of around $\sim$ 1500 nm thickness was formed.

In the second stage, $\sim$ 600 nm thick In-Se layer was deposited by sputtering an indium target and simultaneously evaporating Se in pulses with 1 s period and 300 ms duty cycle (in other words, 0.3s ON and 0.7s OFF) in the same chamber without breaking the vacuum[18].

The $Cu_{2-x}Se$ impurity phase causes shunt leakage paths which can lead to serious degradation in the conversion efficiency. It is, thus, unwanted. This two-stage process effectively eliminates it[82].

After the CIGS deposition, the 5 cm$\times$5 cm$\times$1 mm$\times$ was divided into four smaller cells with dimensions 2.5 cm$\times$2.5 cm$\times$1 mm.

5.2.2 Spin-coating PDT

A $CsCO_3$ (Purity 99.99%, Sigma Aldrich) solution was prepared by dissolving 0.001g of $CsCO_3$ in 10 ml of deionized water. The as-grown CIGS thin-films were then spin coated with the solution at 1000 rpm for 60 seconds, two CIGS absorbers had this treatment done twice and the other had it done once (CIGS absorbers subjected to a spin coating post-deposition treatment are named PDT_SC nº of times the treatment was done CIGS). A set of other 4 cells was not subjected to this treatment to be taken as the reference set of cells.

5.2.3 Annealing

PDT_SC CIGS absorbers (only the absorbers subjected to the spin-coating process) were transferred into the PHRMS chamber and annealed at 400℃ for 2 minutes at the chamber pressure of 6×10^{-6} mbar. No additional Se was supplied during the annealing. When the substrate temperature decreased to around 50 ℃, the samples were then taken out from the vaccum system and proceeded for buffer layer deposition.

5.2.4 Rinsing process

Before deposition of the cadmium sulfide (CdS) buffer layer, the samples (each PDT_SC CIGS and the non-treated CIGS) were rinsed separately with de-ionized (DI) water.

5.2.5 Buffer layer

The CdS buffer layer was prepared with a solution of 1.33 g of thiourea ($SC(NH_2)_2$), 0.118 g of cadmium acetate ($C_4H_6CdO_4$) in 15 ml of NH_3 , and 80 ml of DI water at 60 ℃. The CdS deposition (Chemical Bath Deposition) was performed in separate solutions for each PDT_SC CIGS and non-treated CIGS thin-films to avoid any cross-contamination.

5.2.6 Window layer

The samples were completed by deposition of ∼50 nm intrinsic-ZnO (i-ZnO) and ∼200 nm aluminium-doped ZnO (Al:ZnO) layers by radio-frequency sputtering at room temperature in the window chamber of the STAR system at 5.6×10^3 mbar Ar pressure and with 40 and 60 W, respectively[18].

5.2.7 Sample's division

The 2.5×2.5 cm^2 samples were divided into smaller cells, for three reasons:

- To provide larger statistics.
- To allow proper current transport in the smaller cells, since ZnO:Al is not conductive enough to allow proper current transport over large distances.
- The deposition of the different layers is not completely uniform, thus the cell separation provides a better understanding of the influence of the distance of the sample to the different targets and the selenium source[6].

After cells' separation, one corner of the sample is scratched until the Molybdenum layer is reached, so that it is possible to make a connection to the back contact when doing electrical characterizations.

The exposed Mo layer is covered with Indium, to ensure a proper electrical connection with the separated cells and simultaneously avoid the oxidation of the exposed molybdenum[6].

The nomenclature used for the samples is summarized in Table 6.1.

5.3 Light, Heat and Heat-Light Soaking

The previous sections correspond to work performed by Ishwor Khatri. Light, Heat and Heat-Light Soaking together with sample characterization are the focus of this thesis.

5.3.1 Light Soaking

Post-deposition light soaking was performed using a Newport Corporation's Oriel Sol3A Class AAA Solar Simulator, Model 94043A. It can be seen in Fig. 5.2.

Sample PDT_SC2a was exposed to light for 60 minutes being initially at room temperature. During this process the solar cells were under open-circuit, approximately 1 sun (100 mW/cm2) and AM1.5 conditions without any temperature control.

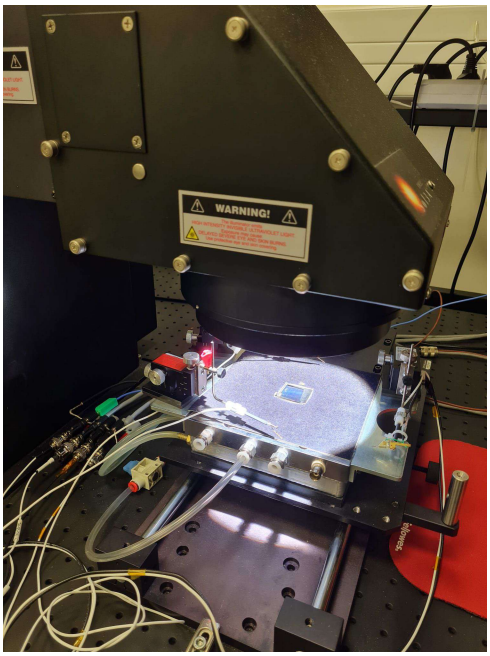

Figure 5.2: Light soaking apparatus.

5.3.2 Heat Soaking

Post-deposition heat soaking was performed using a Heat Plate Stirrer of Fisherbrand Isotemp in Ceramic.

Sample PDT_SC2b was placed in the plate and it was left 5-10min with the desired temperature indicated in the screen of the heater. The desired temperature in this case was 100 °C.

After measurements with the thermocouple, it was realized that after this period of time, in which it is expected that the sample attains the thermal equilibrium with the environment, the temperature of the cell was 75 °C.

After this time interval, 30 minutes were counted as the heat-soaking treatment.

The Heat Plate used is represented in Fig. 5.3.

Figure 5.3: Heat Plate Stirrer of Fisherbrand Isotemp in Ceramic used to the Heat Soaking treatment.

5.3.3 Heat-light soaking

This treatment was done to RS2 and PDT_SC1. It was accomplished using the heater used for the heat-soaking treatment and a LCS-100 Series Solar Simulator.

The heater was placed under the lamp of the solar simulator that had an AM 1.5 filter. For an intensity of 100mW/cm^2 to reach the cells, the sample must have been placed at a distance of 17.8 cm, according to the datasheet. However, it was not possible due to the height of the heater, so the cells were at a distance of 16 cm.

As it was done in the heat soaking treatment, the samples were placed in the heater at the desired temperature of the heater for 5 to 10 min for them to reach the thermal equilibrium with the environment, before turning on the lamp. After this time, the lamp was switched on and 30 minutes were counted for each temperature.

The HLS treatment was done for the temperatures indicated in table 6.13. The temperatures of the samples were again measured with a thermocouple.

After the HLS treatment for each temperature the cells were characterized using the methods here referred.

Fig. 5.4 shows how this treatment was done.

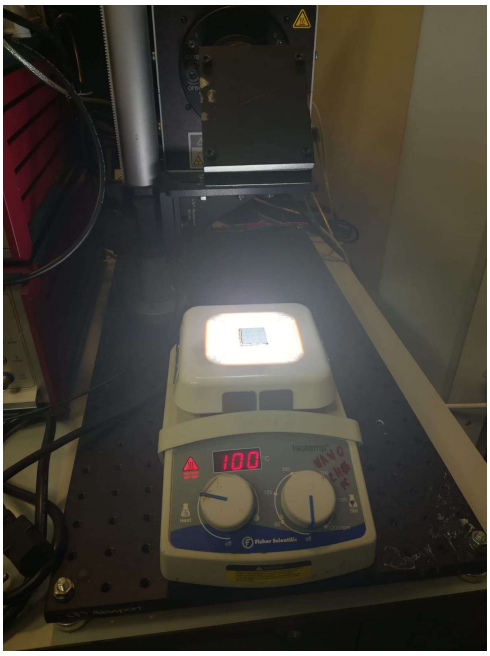

Figure 5.4: System used to do the Heat-Light Soaking treatment.

5.4 Characterization techniques

The characterizations after Light, Heat and Heat-Light Soaking were not done in the same day of the treatment to allow the cells to stabilize (rest time). These were usually done during the next two-three days after the treatments.

5.4.1 Current Density-Voltage

Ideally, the test of the solar cell parameters would be done outdoors, with natural conditions that represent the reality of its commercial application. However, since environment conditions (such as incident solar radiation, angle of incidence, spectral distributions, and temperature) can change throughout the day, year and on different locations on Earth it is essential to establish a basis for scientific testing and assessment of solar cell performance. The solar simulator has the capacity to simulate the standard conditions for cell assessment[37].

The solar simulator used was Oriel Sol3A Class AAA Solar Simulator, Model 94043A. The illumination of this equipment had an intensity of approximately 1 sun (100 mW/cm^2) and its spectrum corresponds to an AM1.5 spectrum.

Fig.5.5 shows the set-up used for the J-V measurements.

Figure 5.5: Solar simulator set-up. Legend: 1-Newport's Corporation Oriel Sol3A Class AAA Solar Simulator, Model 94043A; 2-Silicon Reference Cell; 3-Cell holder; 4-Keithley Source Meter , Model 2420; 5-Arc Lamp Power Supply, Model 69920; 6-Irradiance display; 7-Computer used for IV Test Station Software; 8-Protection Glasses 2, 6-Oriel PV Reference Cell System Model 91150V.

J-V characteristics of the cells were measured using a 4-point-probe set up. Two probes (one for current and one for voltage) were placed in the back contact and the other two probes were placed on the top contact of the cell that was meant to be measured. The position of the probes that gave more consistent results was the one shown in Fig.5.6. The voltage sweep under illumination provides the photovoltaic parameters of the solar cell.

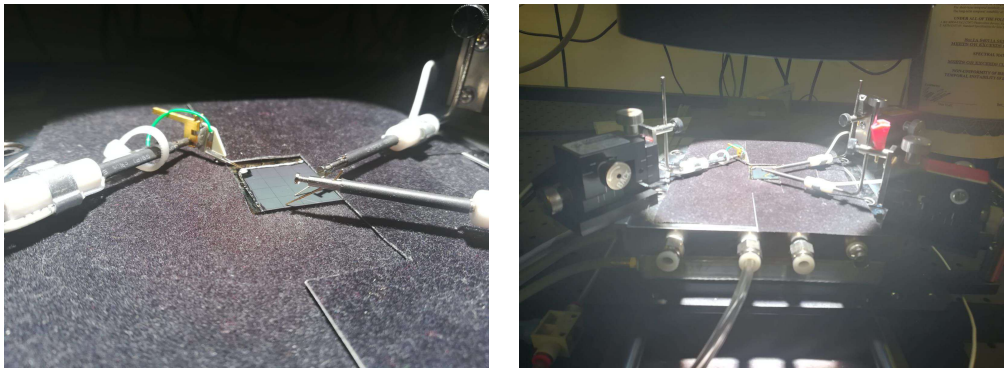

Figure 5.6: Images of solar cell J-V measurement setup with the contact tips.

Before doing the measurement, it was necessary to open the Oriel IV Test Station software and some adjustments had to be done in the PVIV Recipe Editor. Namely:

- The sample area (cell area) which was previously measured using software ImageJ.
- Max Reverse Bias and Max Forward Bias whose values were usually set to -0.1 and 0.6 respectively
- Current limit usually set, for this cells, to 10-15mA.
- Irradiance, that was measured using the reference sample of the Solar Simulator.

Fig. 5.7 shows the software used and where these parameters were changed.

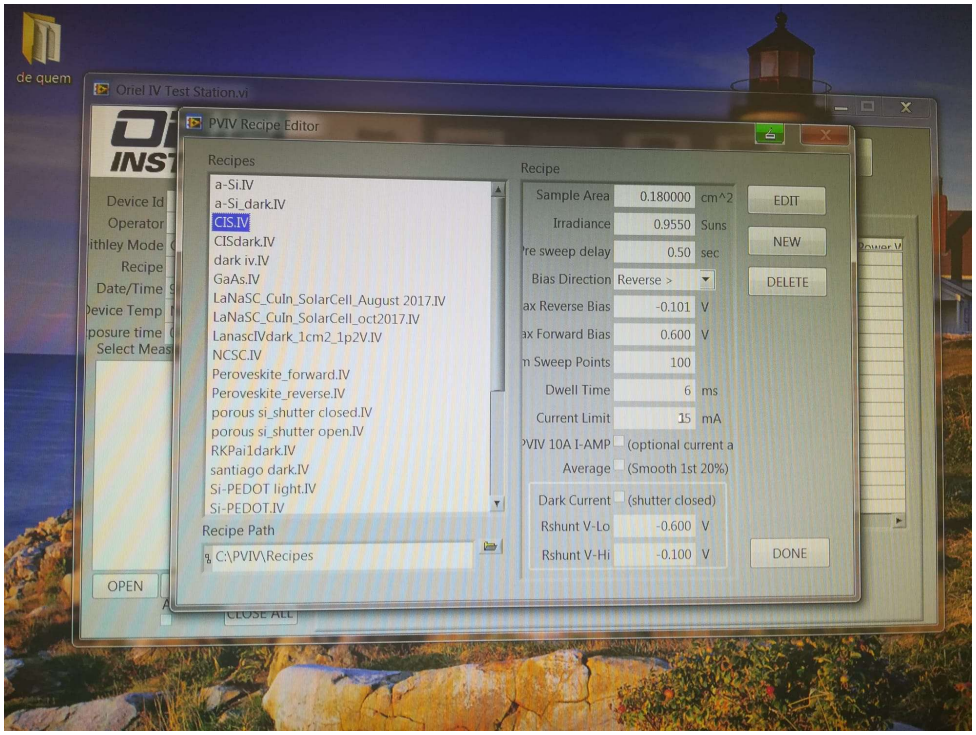

Figure 5.7: Oriel IV Test Station Software.

5.4.2 External Quantum Efficiency

To understand the response of the solar cell to the different wavelengths, external quantum efficiency measurements were taken. The instrumentation used to perform these measurements was Solar Cell Quantum Efficiency Measurement System, Model QEX10 that is depicted in Fig.5.8.

Figure 5.8: Solar Cell Quantum Efficiency Measurement System. On the left: the complete system. On the right: the black box opened. It is possible to see the platform where the cell is placed.

The software used was PV Measurements, Inc. QEX10 Spectral Response /QE/IPCE Measurement System. Some parameters had to be adjusted to get the intended measurements, as it is shown in Fig.5.9, namely:

- Measurement mode- should be DC
- Measurement type- should be Quantum Efficiency

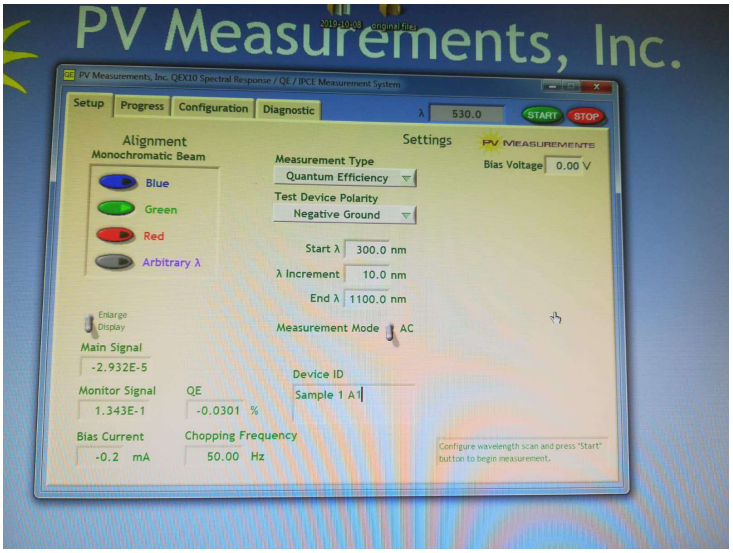

Figure 5.9: Software: PV Measurements, Inc. QEX10 Spectral Response/QE/IPCE Measurement System.

Two probes were used to perform the measurements, each one with one tip. One probe was placed

on the back contact and the other in the cell to be measured. To make sure that the cell catches all the light signal, the green light that can be seen in Fig.5.10 should be completely inside one cell. Besides, the Main Signal indicated in the software should be 1E10 when the lamp corresponding to that signal is in its maximum value of intensity, indicating a good mechanical/electrical connection between the tips and the cell.

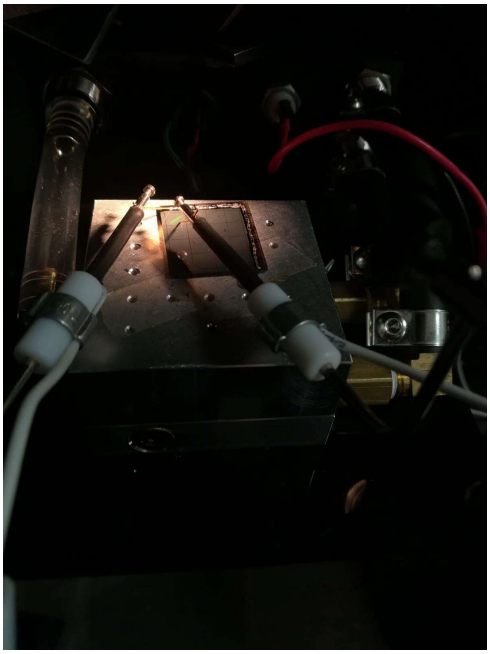

Figure 5.10: Solar cell in Solar Cell Quantum Efficiency Measurement System.

EQE Problems

As stated in Chapter 2, EQE can be used to calculate the J_{sc} of the cell under illumination, as a consequence, ideally, the J_{sc}, as measured by the solar simulator should match the one given by the Solar Cell Quantum Efficiency Measurement System . However, this does not happen in the measurements obtained in this thesis, where a difference between 0.6% and 29.5%, relative to the $J_{sc,JV}$ has been seen. This discrepancy has been reported by many research groups[51]. It was suggested that it might be related to the following effects:

- The setup of EQE uses as a light source a Xe lamp in combination with a monochromator and as a result, the light intensity at a given wavelength can be low compared to the standard 1 sun illumination used in the solar simulator. The charge density is influenced by the light intensity, as a consequence, the mismatch of the $J_{sc,EQE}$ and $J_{sc,JV}$ can increase due to this reason[51].
- For perovskites solar cells, it is mentioned that ion migration can change the interface dynamics during the relatively long time that it takes to record each wavelength for the $J_{sc,EQE}$. However, we are not aware that a similar process can take place in CIGS solar cells[51].
- Longer measurement times might induce long-term sample degradation (this refers to the EQE measurement)[51].
- The measurement conditions at the solar simulator differ from the conditions during the EQE measurement. In particular, when the forward and reverse bias are applied in the solar simulator, the electric field in the solar cell is altered leading to the movement of ions which might result in the creation of a partial build-in potential[51].
- The preconditioning measurement requires the use of white light to check if the required Main Signal is verified to proceed with a correct measurement as indicated in section 5.4.2. The incidence of light in the cell induces a photovoltage that can distort the $J_{sc,EQE}$[51].
- Bad contact of the tips since it is not possible to have a full control on the reliability of the physical contact of the tips. It is not fully reproducible.
- The fact that for some cells the EQE beam size was too large and it did not fit completely in one cell.
- The EQE could not be taken for the complete spectrum of wavelengths that can be absorbed by the CIGS solar cell because of EQE machine limitations.
- The Solar Cell Quantum Efficiency Measurement System was not calibrated as frequently as it would be desirable.

Chapter 6

Results and Discussion

This work consisted on an extensive electrical characterization and analysis of complete CIGS solar cells non-treated and treated by a $CsCO_3$-solution post deposition treatment. The aim was to shed some light in the effect of $CsCO_3$ treatment on the device figure of merit.

The impact of LS (Light Soaking), HS (Heat Soaking) and HLS (Heat-Light Soaking) on these parameters was assessed. LS and HS were only performed in the Cs-treated samples. HLS was carried out in a Cs-free sample and in a Cs-treated sample, allowing to evaluate the role of the alkali treatment on the HLS effect.

The basic solar cell parameters were extracted from the J-V curves. Each sample is composed of several cells, as it can be seen in the Figures presented in each Chapter. For statistically significant results, up to five J-V measurements were done for each cell and the basic solar cell parameters (V_{OC},J_{SC}, FF and Efficiency) were obtained and the corresponding average was calculated. These values, which are shown in section 6.5 were used to do the box-plots. The average and standard deviation for each sample was calculated based on the values obtained for all the cells contained in the sample. For each individual cell, the corresponding errors are not shown because the statistical errors obtained are smaller than the real error, the systematic error of the equipment.

EQE measurements were also done in each cell of the samples. Each cell was measured up to 5 times. However, only one measurement of one cell of each sample was presented here: the measurement of the cell that had a minor discrepancy between $J_{SC,JV}$ and $J_{SC,EQE}$, or, in the LS, HS and HLS case, the measurements of the cell for which the sum of discrepancies (for example, discrepancies for the measurements before and for the measurements after the LS in that cell) was smaller.

The Figures of the samples presented in each section and specially in section 6.5, have values highlighted in yellow, that correspond to the individual cells presented in this thesis, and values in green corresponding to the cell/s with the best efficiency.

The results of these measurements are presented in this chapter.

6.1 $CsCO_3$-Solution Post Deposition Treatment of CIGS

As mentioned in the previous section, a PDT treatment with Cesium was done for CIGS samples.

The following samples were analyzed: a reference sample (Cs-free), PDT_SC1, a sample with one spin-coating process of the $CsCO_3$ solution, and two samples, PDT_SC2a and PDT_SC2b, where the spin-coating process was repeated twice. The last two samples were subjected to the same treatment to test the reproducibility of the spin-coating process. The samples described are represented in Fig.6.1. Table 6.1 summarizes the nomenclature used.

	Times the spin-coating treatment was done	Rotations per minute	Concentration of the Cs solution	Date of fabrication
Reference samples	0	0	0	20/10/2021
PDT_SC1	1	1000	1mg/10mL	16/12/2021
PDT_SC2a	2	1000	1mg/10mL	16/12/2021
PDT_SC2b	2	1000	1mg/10mL	16/12/2021

Table 6.1: Information about the samples used

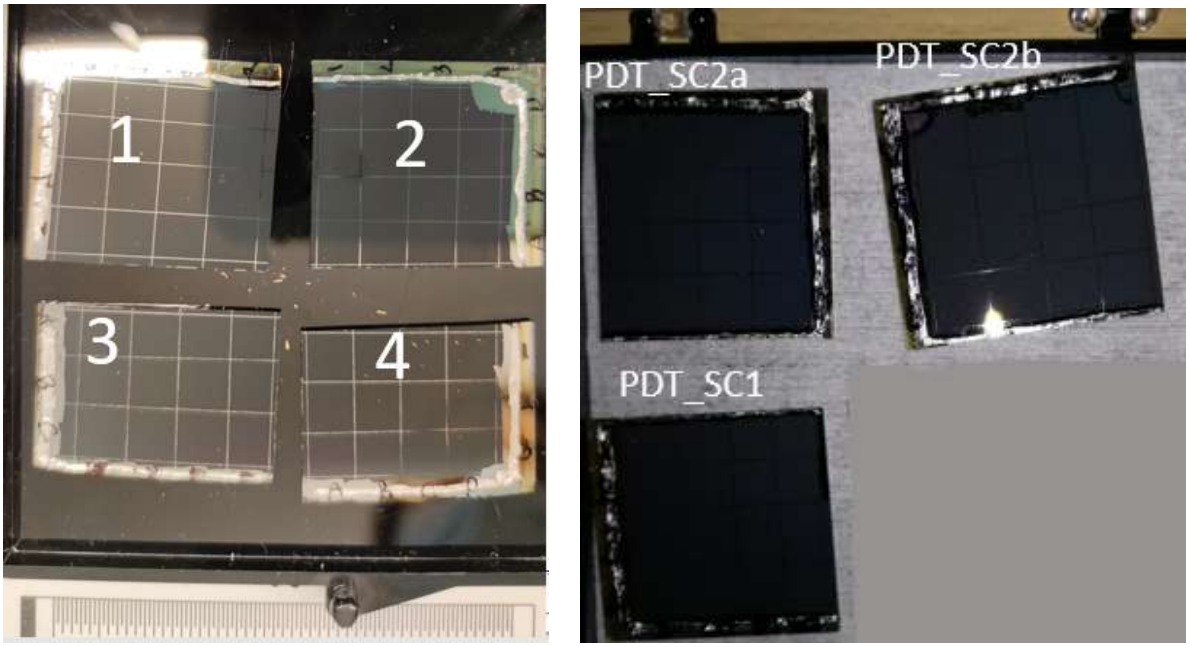

(a) (b)

Figure 6.1: a) Reference samples: Cs-free samples b)Treated samples: PDT SC1-with one spin-coating process of the $CsCO_3$ solution; PDT SC2a and PDT SC2b-samples where the spin-coating process was repeated twice.

6.1.1 J-V measurements

The basic solar cell parameters of the Reference samples, PDT_SC1, PDT_SC2a and PDT_SC2b are presented in here. Each rectangle in figure 6.2 a, b, c, d and in 6.3 a, b, c represents individual cells within a sample. The measurements of V_{OC} are shown in figures Fig.6.2 and Fig.6.3 for the reference cells and the treated samples respectively as an example although this procedure was used for all the parameters (V_{OC}, J_{SC}, FF and Efficiency). Values highlighted in yellow correspond to the individual cells presented in this thesis, and values in green correspond to the cell/s with the best efficiency.

	D	C	B	A
4				
3	0.367			
2		0.374	0.373	0.384
1			0.382	

(a) Reference Sample 1

1	2	3	4	
				D
0.379	0.388			C
		0.396		B
			0.403	A

(b) Reference Sample 2

A				0.381
B		0.396	0.356	
C	0.412			
	1	2	3	4

(c) Reference Sample 3

			0.406	1
	0.409	0.409		2
0.415				3
A	B	C	D	

(d) Reference Sample 4

Figure 6.2: V_{OC} measurements in Volts of reference samples 1, 2, 3 and 4.

1		0.483	0.332	0.350
2	0.487	0.485	0.484	0.477
3	0.484	0.480	0.481	0.478
4	0.429	0.484	0.482	0.426
	A	B	C	D

(a) PDT_SC1

1	2	3	4	
	0.423	0.487	0.466	A
0.470	0.478	0.480	0.478	B
0.475	0.481	0.479	0.470	C
0.438	0.492	0.479	0.432	D

(b) PDT_SC2a

	4	3	2	1
A		0.493	0.491	0.473
B	0.499	0.493	0.489	0.485
C	0.482		0.492	0.473
D	0.502	0.505	0.504	0.446

(c) PDT_SC2b

Figure 6.3: V_{OC} measurements in Volts of samples PDT_SC1, PDT_SC2a and PDT_SC2b.

Not all the cells of each reference sample were measured since all the 4 samples were fabricated in the same way and to get a similar data to the treated samples, only the diagonal cells were measured.

This also allows to consider the gradient that occurs due to the fixed sputtering source of the material which was also verified in other cells fabricated in STAR[83].

The box-plots of the basic solar cell parameters are represented in Fig.6.4 and its means and standard deviation are in Table 6.2. All the cell measurements that gave origin to these plots are in section 6.5.5.

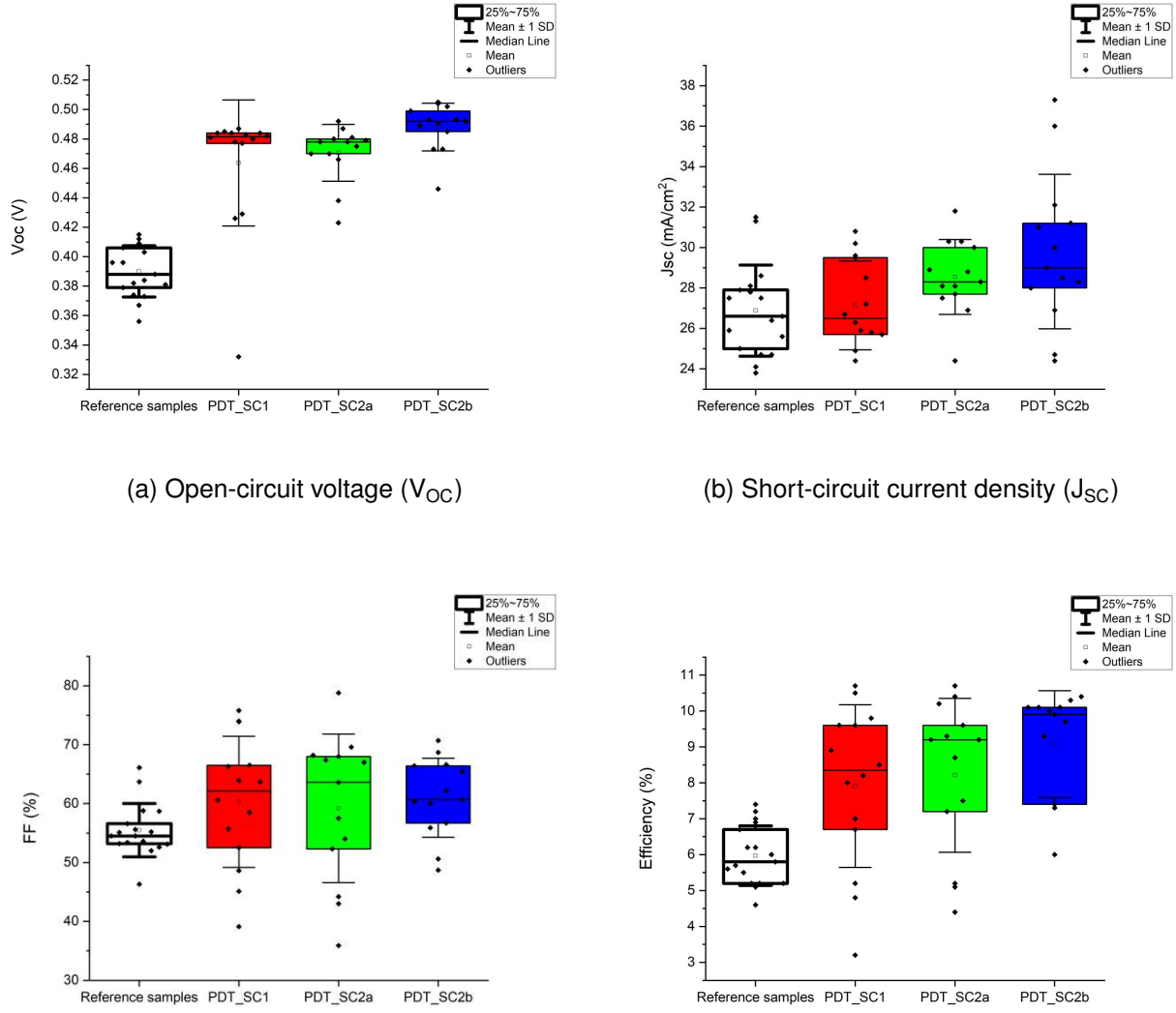

(a) Open-circuit voltage (V_{OC})

(b) Short-circuit current density (J_{SC})

(c) Fill Factor (FF)

(d) Efficiency

Figure 6.4: Box-plots of the solar cell basic parameters of the Reference Samples, PDT_SC1, PDT_SC2a and PDT_SC2b.

	V_{OC}(V)	J_{SC}(mA/cm^2)	FF(%)	Efficiency(%)
Reference samples Mean	0.390± 0.017	26.9 ± 2.3	55.5±4.5	6.0±0.8
PDT_SC1 Mean	0.464±0.043	27.1±2.2	60±11	7.9±2.3
PDT_SC2a Mean	0.471±0.019	28.5±1.9	59±13	8.2±2.1
PDT_SC2b Mean	0.488±0.016	29.8±3.8	61.0±6.7	9.1±1.5

Table 6.2: Solar cell basic parameters average and standard deviation of Reference samples, PDT_SC1, PDT_SC2a and PDT_SC2b.

From the graphs of Fig.6.4 and Table 6.2 it is possible to observe an increase in the V_{OC} with the spin-coating treatment. The treatment done once-PDT_SC1-leads to an increase of V_{OC} of the order of 0.074V . However, this increment is more pronounced for sample PDT_SC2b, for which an improvement of 0.098V was verified. The J_{SC} also showed an increase, not as pronounced as the V_{OC}, of 2.9 mA/cm^2 for PDT_SC2b. FF shows a small increase with respect to the Reference Samples. Both J_{SC} and FF changes are not as significant as the V_{OC} due to their large errors (which does not allow to conclude with confidence that the increase is real). The largest efficiency increase with the Cs-PDT treatment was 3.1% and was observed for the PDT_SC2b sample. Overall, the results indicate that the double spin-coating process results in better efficiency. According to the observations, the efficiency increase can be mainly attributed to the V_{OC} increase.

From the comparison of results of samples with the same treatment (PDT_SC2a and PDT_SC2b) and considering their standard deviations, it can be inferred that the reproducibility of the spin-coating process is fairly reasonable, once that no significant changes appear for the solar cell basic parameters.

J-V curves and basic parameters of the selected cells

The J-V curves of the selected cells for each treatment are presented in Fig. 6.5, along with the basic solar cell parameters for the same cells in Table 6.3.

	V_{OC}(V)	J_{SC}(mA/cm^2)	FF(%)	Efficiency(%)
Ref_Sample2_C1	0.379	27.5	66.1	7.0
PDT_SC1_A2	0.487	25.9	63.9	8.2
PDT_SC2a_B3	0.480	27.7	78.8	10.7
PDT_SC2b_D3	0.505	31.2	60.3	9.7

Table 6.3: Basic solar cell parameters of the selected cells of Reference samples, PDT_SC1, PDT_SC2a and PDT_SC2b.

Regarding the behaviour of the Cells PDT_SC2b_D3 and PDT_SC2a_B3, the first displays a higher Jsc and V_{OC}, (around 3.5 mA/cm^2 and 0.025V larger respectively) than the second. On the other hand, this previous cell shows a higher efficiency ($\approx$ 1% larger) which is caused by its greater FF (18.5% above that of cell PDT_SC2b_D3). This difference might be assigned to the non-homogeneity that results from the deposition process and the spin-coating treatment, meaning that the Cs-solution might be distributed in a different way in both cells, which might affect its solar cell basic parameters.

It is important to highlight that both cells, PDT_SC2a_B3 and PDT_SC2b_D3, exhibit better solar cell

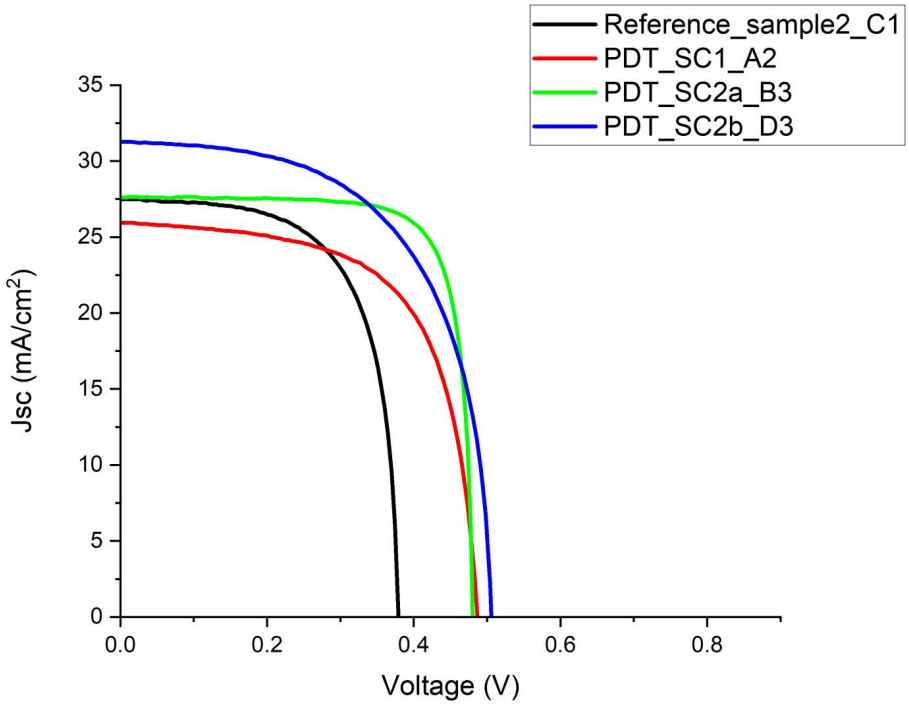

Figure 6.5: J-V curves of the selected solar cells: Ref_Sample2_C1, PDT_SC1_A2, PDT_SC2a_B3, PDT_SC2b_D3.

basic parameters than PDT_SC1, which indicates that doing the double spin-coating treatment leads to a better performance of the solar cell.

6.1.2 External quantum efficiency

EQE measurements were also performed. In this chapter, only the EQE of the selected cells is presented to display the differences between the several samples with different treatments.

	Ref_Sample2_C1	PDT_SC1_A2	PDT_SC2a_B3	PDT_SC2b_D3
$J_{sc,EQE}$ (mA/cm^2)	26.9	26.5	27.9	30.8
$J_{sc,JV}$ (mA/cm^2)	27.5	25.9	27.7	31.2

Table 6.4: Comparison of J_{SC} measured in the Solar Cell Quantum Efficiency System and in the Solar Simulator for Ref_Sample2_C1, PDT_SC1_A2, PDT_SC2a_B3, PDT_SC2b_D3.

The uncertainty of the EQE measurements was not indicated because only one measurement of EQE of each cell was considered. The uncertainty that should be considered is the instrumentation uncertainty.

There is a fair agreement for the J_{SC} values determined from J-V and EQE measurements. By comparing the EQE spectra in Fig. 6.6 the main changes are seen for PDT_SC2a_B3 and PDT_SC2b_D3 in relation to Ref_Sample2_C1. The EQE is higher for cells PDT_SC2a_B3 and PDT_SC2b_D3, from 500nm to 1100nm for PDT_SC2b_D3 and to 900nm for PDT_SC2a_B3 in comparison to Ref_Sample2_C1.

The EQE increase from 500nm to 540nm for PDT_SC2a_B3 and PDT_SC2b_D3 indicates a better

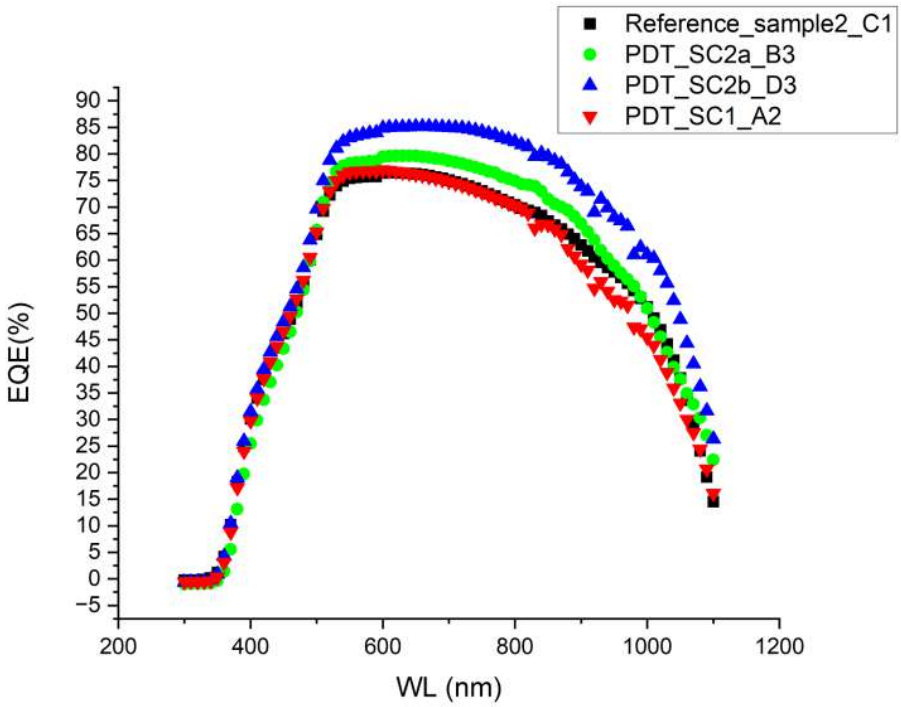

Figure 6.6: EQE curves of the selected solar cells: Ref_Sample2_C1, PDT_SC1_A2, PDT_SC2a_B3, PDT_SC2b_D3.

absorption and collection of photons absorbed in the CdS layer and at the interface CdS/CIGS as shown in Fig.2.14. The improvement of the EQE from 540nm to 900/1100 nm shows that the absorption and collection of photons absorbed in the CIGS is higher, the increase in EQE in this range also indicates that the recombination losses are smaller. The curve of PDT_SC2b_D3 has higher values of EQE until the longer wavelengths (1100nm) meaning that recombination losses are reduced until a greater depth of the absorber layer, which might mean that the Cs reached a greater depth for this cell[9][84]. These observations agree with the results of V_{OC} and J_{SC} registered for this cell, since less recombination and a better collection of carriers enhances these parameters, which are the highest among the 4 cells measured.

Although there is slight difference between PDT_SC2a_B3 and PDT_SC2b_D3, as it was verified too in $J_{sc,JV}$, both samples show an EQE larger than that of PDT_SC1_A2. EQE results confirm the results of J_{SC} obtained for J-V measurements and reinforce the observation that the double Cs treatment favors more the improvement of device properties.

6.1.3 Discussion of all the results of $CsCO_3$-solution post-deposition treatment

As previously mentioned, both Fig.6.4 and Table 6.2 demonstrate an overall improvement in all basic solar cell parameters with the spin-coating PDT, consistent with the findings reported in [18], except for J_{SC}. It was suggested that a possible reason for this improvement is the modification of the CIGS surface with the formation of O-Cs structures with Indium (represented in Fig.6.7). The Cs-induced CIGS

surface modification, has in addition an impact on the electronic properties , by lowering the VBM. This change is expected to increase the hole barrier, reducing the concentration of holes accumulating at the absorber surface and thus inhibiting the recombination at the buffer/CIGS interface. As a result, device performance should improve [66].

Reference [18] also suggested that Cs_{Cu} could form and annihilate the deep gap states at GBs(In_{Cu} deep donor-like defects)[85]. This hypothesis was presented since that there was an evidence of the presence of Cs at the grain boundaries together with a Cu depletion. Eliminating the deep gap states may enhance the p-type conductivity/increase the number of holes, contributing to the improvement of the V_{OC}. This may serve as a potential mechanism behind the results obtained in the present study.[18].

Regarding the improvements observed for the solar cells subjected to the double spin-coating, similar studies were done with other heavy metal such as K. It was verified that the greater the concentration of a KF solution, the greater the V_{OC} value[22]. In this thesis, the treatment involved increasing the number of times spin-coating was performed, rather than altering the solution concentration. In both cases, the amount of Cs present is increased. The results of this thesis and the ones obtained using a KF solution indicate that with increasing quantity of the heavy metal in the spin-coating treatment (whether in the form of concentration or times the spin-coating is done) better solar cell basic parameters are obtained. For a confirmation of this hypothesis for the $CsCO_3$-solution, a new treatment with a solution with greater concentration could be done. The results of Fig. 6.5, Table 6.3 reinforced this hypothesis as well as the results obtained from the EQE (Fig.6.6), which show that recombination losses in the absorber layer are smaller for the cells subjected to the spin-coating twice.

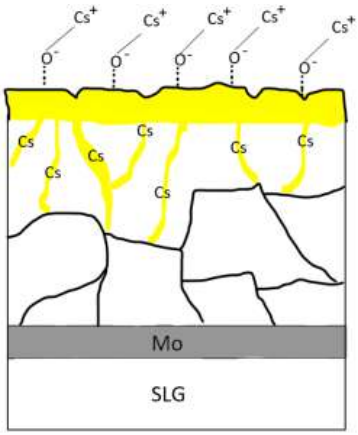

Figure 6.7: Structure suggested to be formed in the CIGS surface. Adapted from [18].

6.2 Light Soaking

The sample PDT_SC2a was subjected to a Light Soaking treatment, during 60 minutes, after which is labeled PDT_SC2a_LS60'. Table 6.5 resumes the nomenclature.

Denomination	PDT_SC2a	PDT_SC2a_LS60'
Light Soaking treatment for 60'		X

Table 6.5: Denomination of the sample.

6.2.1 J-V measurements

The box-plots of the basic solar cell parameters extracted from the J-V measurements of sample PDT_SC2a before and after Light Soaking are represented in Fig.6.9 and its means and standard deviations in Table 6.6. The measurements of V_{OC} were done for PDT_SC2a and PDT_SC2a_LS60'. These are shown in figure Fig.6.8. All the measurements that gave origin to these plots are shown in section 6.5.2.

1	2	3	4	
	0.423	0.487	0.466	A
0.470	0.478	0.480	0.478	B
0.475	0.481	0.479	0.470	C
0.438	0.492	0.479	0.432	D

(a) PDT_SC2a

1	2	3	4	
	0.322	0.481	0.453	A
0.462	0.476	0.477	0.458	B
0.474	0.481	0.480	0.472	C
0.317	0.470	0.459	0.453	D

(b) PDT_SC2a_LS60'

Figure 6.8: V_{OC} measurements in Volts of sample PDT_SC2a before and after Light Soaking.

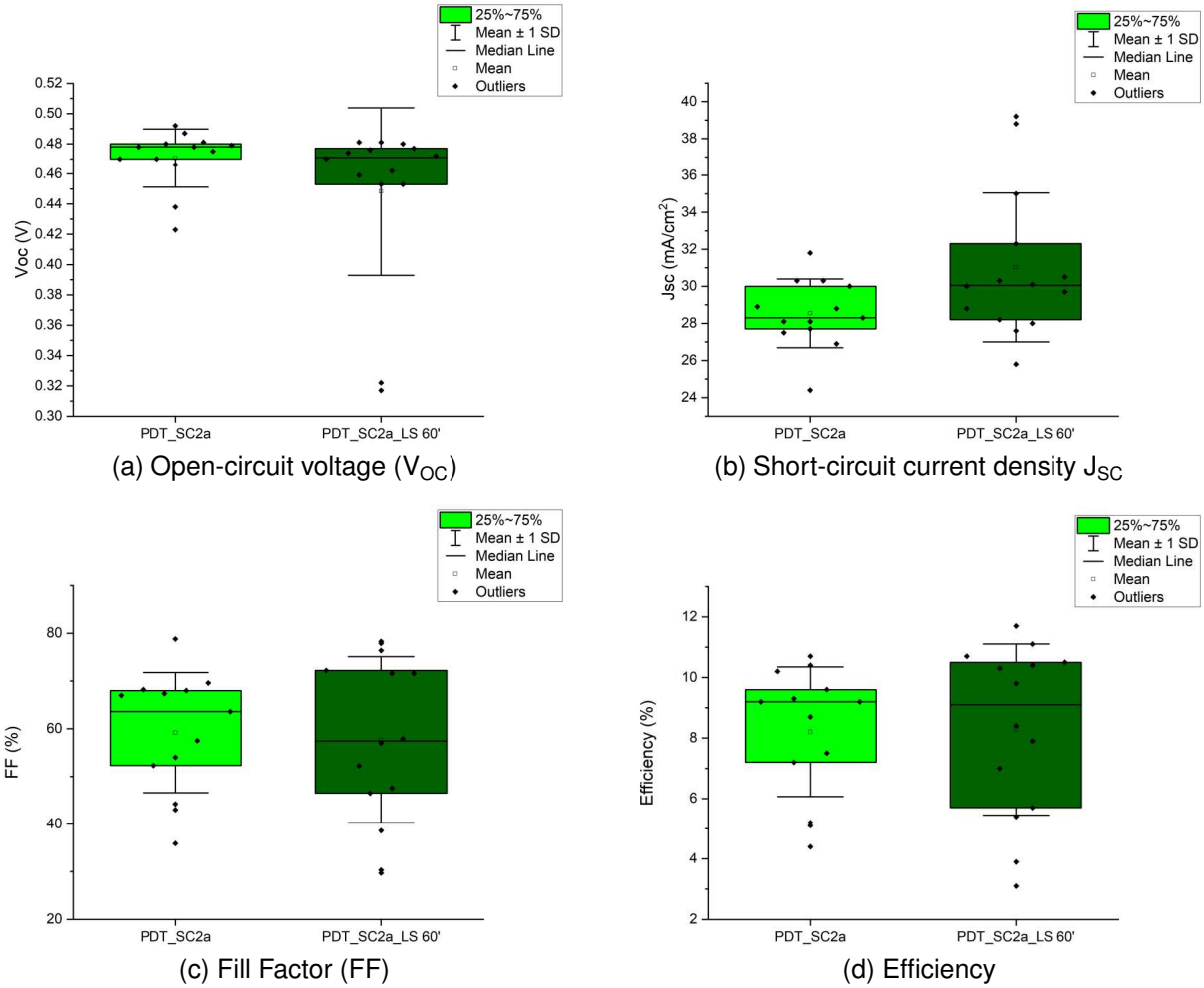

(a) Open-circuit voltage (V_{OC})

(b) Short-circuit current density J_{SC}

(c) Fill Factor (FF)

(d) Efficiency

Figure 6.9: Solar cell basic parameters of the samples before and after Light Soaking.

	V_{OC}(V)	J_{SC}(mA/cm^2)	FF(%)	Efficiency(%)
PDT_SC2a Mean	0.471±0.019	28.5±1.9	59±13	8.2±2.1
PDT_SC2a_LS60' Mean	0.448±0.055	31.0±4.0	58±17	8.3±2.8

Table 6.6: Solar cell basic parameters means and standard deviation of the sample PDT_SC2a before and after Light Soaking.

According to the results presented in Fig. 6.9 and Table 6.6 there is no evidence for light soaking induced effects on the CIGS solar cell figure of merit. The mean values of V_{OC}, J_{SC}, FF and Efficiency are quite similar, with the exception of a slight increase in the box-length 25%-75% core value.

J-V curves and solar cell basic parameters of the selected cell

The J-V curves of the selected cell (B3) before and after the light soaking treatment is presented in Fig.6.10 , along with its basic solar cell parameters in table 6.7.

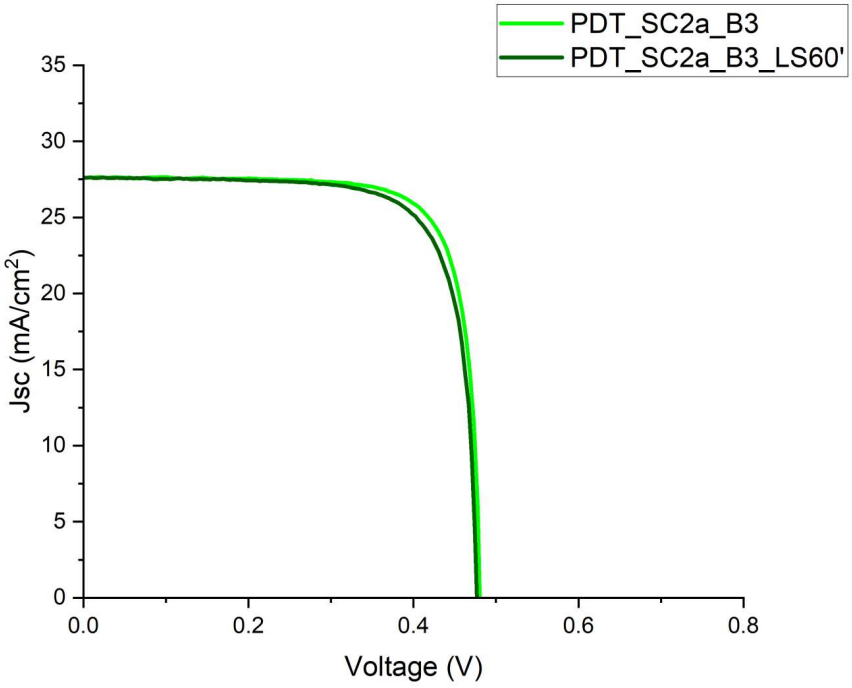

Figure 6.10: J-V curves before and after Light Soaking of cell PDT_SC2a_B3.

	V_{OC}(V)	J_{SC}(mA/cm^2)	FF(%)	Efficiency(%)
PDT_SC2a_B3 Mean	0.480	27.7	78.8	10.7
PDT_SC2a_B3_LS60' Mean	0.477	27.6	76.4	10.3

Table 6.7: Basic solar cell parameters of cell PDT_SC2a_B3 before and after Light Soaking.

From the analysis of the individual J-V curves of a selected cell, we observe a small variation (decrease) of the FF and Efficiency after the light-soaking process. These are not significant changes. Thus, they are in agreement with the conclusions taken from the the box-plots where no changes were observed with the LS (Fig.6.9).

6.2.2 External quantum efficiency

EQE measurements of the PDT_SC2a sample were taken before and after light soaking. The EQE curves shown in Fig.6.11 are also of the cell B3.

The shape of the EQE spectra does not change after the light soaking process and the J_{SC} extracted are very similar to the J_{SC} determined from J-V measurements (as well as their variation with the LS). The results indicate that the 60' light soaking process does not impact the CIGS cell properties.

	PDT_SC2a_B3	PDT_SC2a_B3_LS60'
$J_{sc,EQE}$(mA/cm^2)	27.9	28.0
$J_{sc,JV}$(mA/cm^2)	27.7	27.6

Table 6.8: Comparison of J_{SC} measured in the Solar Cell Quantum Efficiency System and in the Solar Simulator for PDT_SC2a_B3.

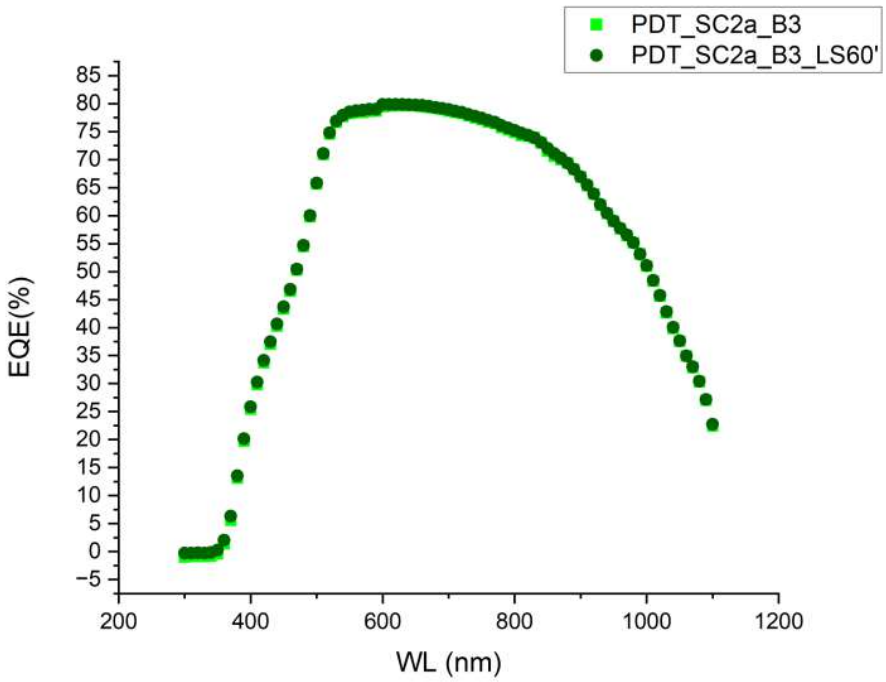

Figure 6.11: EQE curves of the solar cell PDT_SC2a_B3 before and after Light Soaking.

6.2.3 Discussion of all the results of the Light Soaking Treatment

J-V and EQE characterizations indicate that the Light Soaking process of 60 minutes does not have a noticeable effect on the CIGS sample. Similar observations were also reported in [17] where LS was performed for NaF treated CIGS solar cells for 30 minutes under 1-sun illumination and the cell parameters hardly changed. It was suggested that a long-term LS could change the cell performance together with moderated temperatures[17]. This could allow to promote the change of configuration of the V_{Se}-V_{Cu} complex from donor to acceptor with the increase of net hole concentration and subsequent increase in V_{OC}[86] [71].

Currently, in the state-of-the-art solar cells, there is a lack of evidence regarding the distribution of Cs within CIGS solar cells both before and after light soaking. It is possible that light soaking alters the distribution of the Cs atoms through a photo-induced electric field produced by the accumulation of charges in the opposite contacts[17]. The new distribution of the Cs atoms may cause electrostatic fluctuations in the SCR, which has, as mentioned in [71], negative effects on the V_{OC}. This detrimental effects may be counteracted by the positive effects of the LS reported, such as the increase of diffusion-length due to the occupation of donor states/emptying of acceptor states during illumination, which then reduces the trapping of free charge carriers during the operation of the solar cell[71]. The net effect

of these opposing factors may be negligible, resulting in no significant overall effect on the solar cell performance.

On the other hand, it is possible that the positive effects of light soaking are not immediately observable after a single night in the dark. This could be due to insufficient time for the redistribution of free charge carriers after modifications in charge states of point defects. Such phenomenon could lead to a more homogeneous width of the SCR and a subsequent reduction of electrostatic fluctuations[71].

6.3 Heat-soaking

Sample PDT_SC2b was subjected to a Heat Soaking treatment, during 30 minutes, with a temperature of the heater of 100 °C. The temperature of the sample measured with a thermocouple was of 75 °C. The sample after the Heat Soaking is labeled PDT_SC2b_HS30'.Table 6.9 resumes the nomenclature.

	PDT_SC2b	PDT_SC2b_HS30'
Heat soaking treatment for 30'		X

Table 6.9: Denomination of the sample.

6.3.1 J-V measurements

The box-plots of the basic solar cell parameters extracted from the J-V measurements of sample PDT_SC2b before and after HS are represented in Fig.6.13 and its mean and standard deviation in Table 6.10. The measurements of V_{OC} for PDT_SC2b and PDT_SC2b_HS30' are shown in figure Fig.6.12. All the measurements that gave origin to these plots are in section 6.5.3. Values highlighted in yellow correspond to the individual cells presented in this thesis, and values in green correspond to the cell/s with the best efficiency.

	4	3	2	1
A		0.493	0.491	0.473
B	0.499	0.493	0.489	0.485
C	0.482		0.492	0.473
D	0.502	0.505	0.504	0.446

(a) PDT_SC2b

	4	3	2	1
A		0.484	0.486	0.411
B		0.492	0.484	0.479
C	0.468	0.484	0.332	0.466
D	0.489	0.490	0.483	0.478

(b)PDT_SC2b_HS30'

Figure 6.12: V_{OC} measurements in Volts of sample PDT_SC2b before and after Heat Soaking.

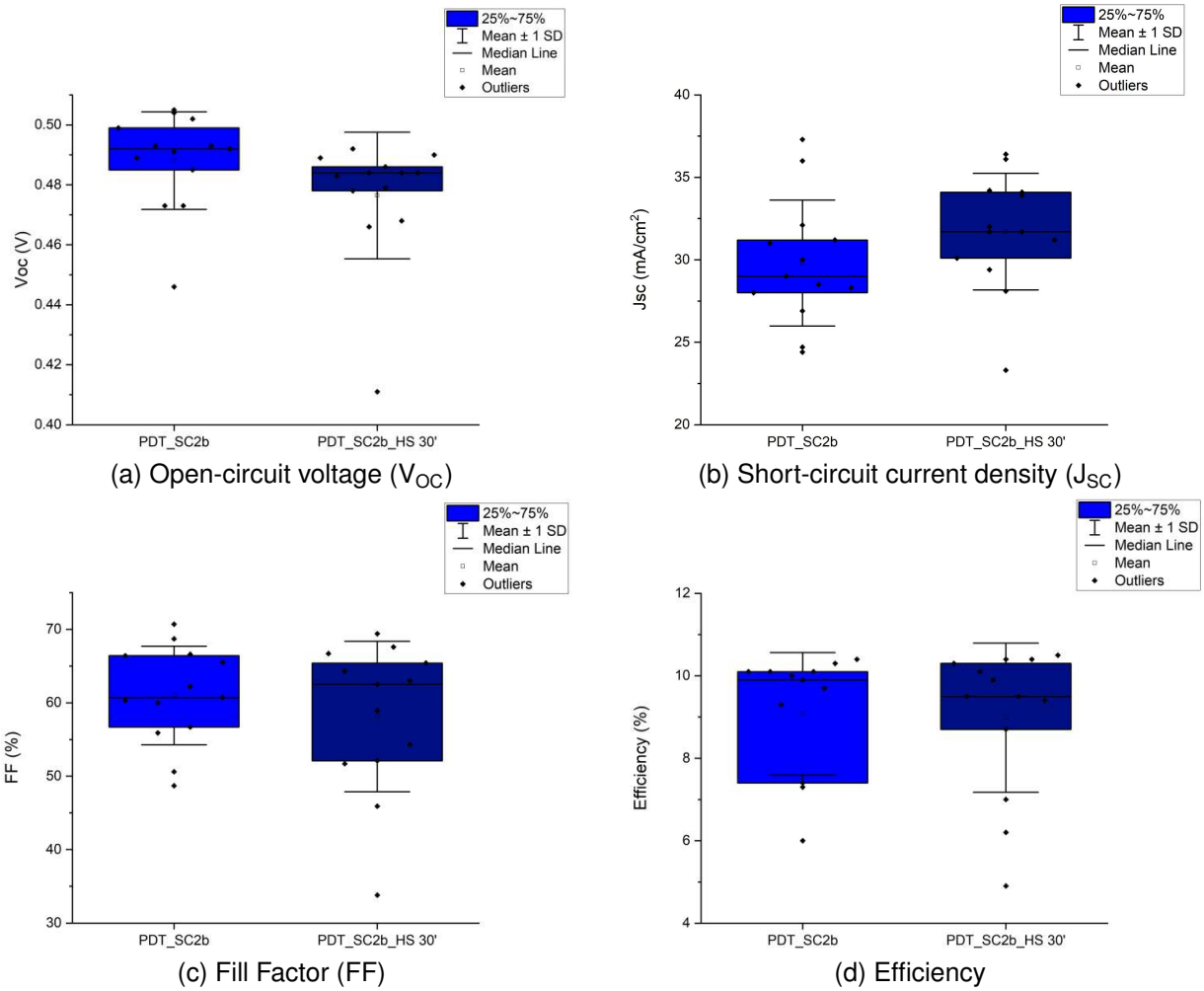

(a) Open-circuit voltage (V_{OC})

(b) Short-circuit current density (J_{SC})

(c) Fill Factor (FF)

(d) Efficiency

Figure 6.13: Solar cell basic parameters of the samples before and after Heat Soaking.

	V_{OC}(V)	J_{SC}(mA/cm^2)	FF(%)	Efficiency(%)
PDT_SC2b Mean	0.488±0.016	29.8±3.8	61.0±6.7	9.1±1.5
PDT_SC2b_HS30' Mean	0.476±0.021	31.7±3.5	58±10	9.0±1.8

Table 6.10: Solar cell basic parameters means and standard deviations of the samples before and after Heat Soaking.

After the HS treatment no changes are visible in the solar cell basic parameters. Since the uncertainties are very large there is no obvious trend associated with the HS treatment.

J-V curves and solar cell basic parameters

The J-V curves of the selected cell(A2) before and after the Heat Soaking treatment is presented in Fig.6.14 , along with the basic solar cell parameters in table 6.11.

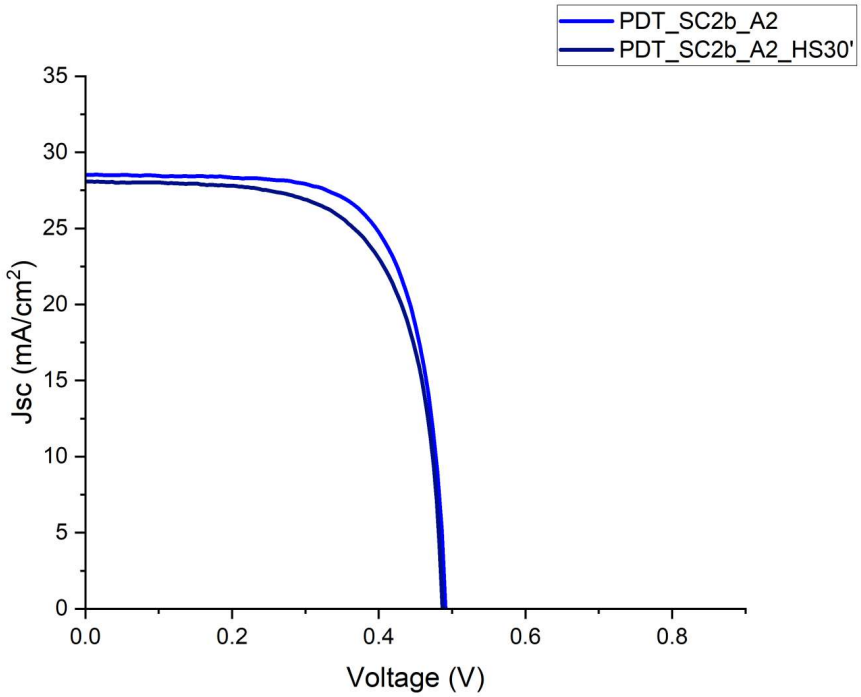

Figure 6.14: J-V curves of cell PDT_SC2b_A2 before and after Heat Soaking.

	V_{OC}(V)	Jsc(mA/cm^2)	FF(%)	Efficiency(%)
PDT_SC2b_A2	0.491	28.5	70.7	10.1
PDT_SC2b_A2_HS 30'	0.486	28.1	67.6	9.5

Table 6.11: Basic solar cell parameters of cell PDT_SC2b_A2 before and after Heat Soaking.

The J_{SC} was the parameter that suggests a different tendency from the one displayed by the means of all the cells in Table 6.10, however these values are within the uncertainties calculated.

In this cell, the significant changes (considering the relative error of all the parameters in relation to the cell before the HS) were the FF and efficiency (3.1% and 0.65% respectively). The decrease of the FF might be related to a decrease of the R_{Shunt}, which can be hypothesized by noting the shape of the J-V curve and comparing it to Fig.2.13. The efficiency decrease might be related to the decrease of the FF.

6.3.2 External quantum efficiency

EQE measurements of the PDT_SC2b sample were taken before and after Heat Soaking. The EQE curves shown in Fig.6.15 are also of the cell A2.

	PDT_SC2b_A2	PDT_SC2b_A2_HS 30'
$J_{sc,EQE}$(mA/cm^2)	29.8	28.9
$J_{sc,JV}$(mA/cm^2)	28.5	28.1

Table 6.12: Comparison of J_{SC} measured in the Solar Cell Quantum Efficiency System and in the Solar Simulator for PDT_SC2b_A2.

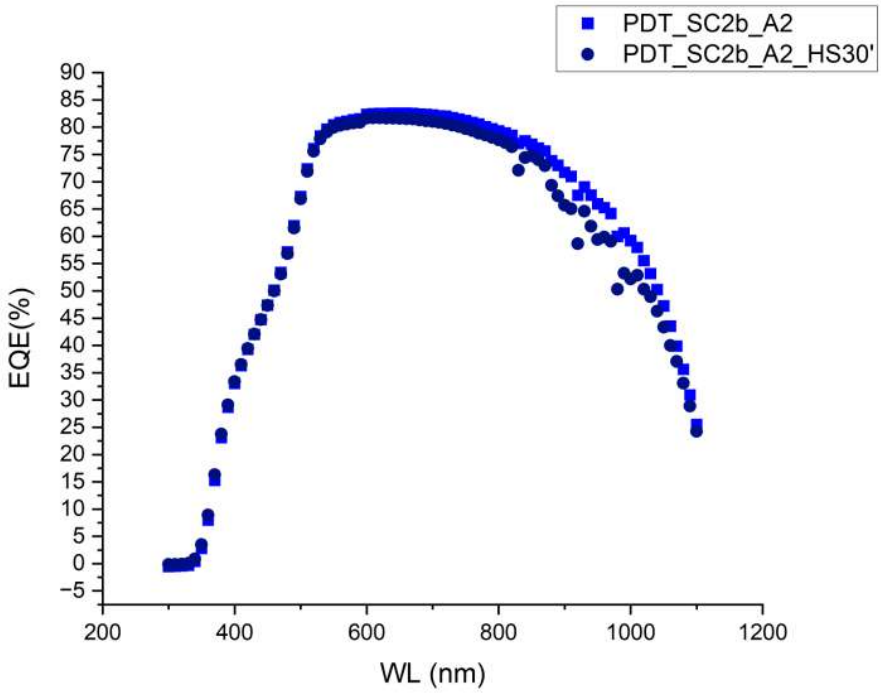

Figure 6.15: EQE curves of cell PDT_SC2b_A2 before and after Heat Soaking.

The $J_{sc,EQE}$ follows the trend given by $J_{sc,JV}$. The EQE shows a small decrease from 600 nm to 1050 nm after the HS, this might happen due to recombination losses in the CIGS as it is explained in Fig. 2.14.

6.3.3 Discussion of all the results of the Heat Soaking Treatment

The sample that was exposed to the heat-soaking treatment did not show relevant changes taking into account the standard deviations. The selected cell showed a small decrease in the FF and in the efficiency, which could be caused, as mentioned before by a decrease of the R_{shunt} or, as indicated by the EQE, by recombination losses in the CIGS. Generally, when HS alters the behaviour of the basic solar cell parameters of treated and non-treated CIGS, the exposition times and/or temperatures are usually longer and higher respectively or the Heat Soaking is performed after a previous HLS treatment[17] [72]

[75] [27] [87]. The absence of significant improvement on the solar cell parameters, for the conditions used, may indicate that higher temperatures or longer annealing/ heating should be used to get an HS effect. That way, more energy can be transmitted to the constituents of the cell and perhaps allow the movement of alkali atoms through the solar cell, which can lead to passivation of defects and ionic substitution of lighter alkali atoms for example, inducing variations in the solar cell basic parameters[28] [30]. Higher temperatures would also contribute to the conversion of the V_{Se}-V_{Cu} defect complex from donor to acceptor (because this configuration is enhanced with temperature). This reaction, would lead to the increase of the number of holes in the CIGS and as a consequence to a higher open-circuit voltage (and lower Jsc because of the decreased SCR)[86]. [17]

These are hypothesis, so, further studies are needed to fully understand the effects of heat soaking on Cs-treated samples, especially considering that this is a novel approach and little research has been conducted on it. To better understand these effects, it may be helpful to apply the heat treatment to a non-treated sample as well as a sample that has undergone spin-coating more than twice. This would allow for a more comprehensive investigation of the impact of heat treatment on the samples.

6.4 Heat-light soaking

Heat-light soaking treatment was performed on a reference sample (Reference sample 2) and on a sample subjected to a spin-coating Cs-PDT (PDT_SC1). A reference sample was used in order to understand if the heat-light soaking effects are enhanced by the spin-coating Cs-PDT.

In this treatment, the samples were heated at several temperatures while exposed to light. For each temperature, the cell was subjected to the Heat-Light Soaking treatment for 30 minutes. After the Heat-Light Soaking treatment at each temperature, J-V and EQE were done to examine the behaviour of the samples.

6.4.1 Reference Sample 2

The denomination used in the graphs as well as the temperatures that were set in the heater and the respective temperatures of the sample measured by a thermocouple are summarized in table 6.13.

	RS2_RT	**RS2_HLS_75 °C**	**RS2_HLS_90 °C**	**RS2_HLS_112 °C**	**RS2_HLS_145 °C**
Heat-light soaking treatment		X	X	X	X
Temperature indicated in the heater(°)	0	100	130	150	200
Temperature of the sample(ºC)	25	75	90	112	145

Table 6.13: Sample denomination for each temperature.

J-V measurements

The box-plots of the basic solar cell parameters extracted from the J-V measurements of Reference Sample 2 are represented in Fig.6.17, and its means and standard deviation shown in Table 6.14. In the

horizontal axis of the box-plots, the temperatures of the HLS are indicated. RT stands for Room Temperature, the temperature of the sample before doing the HLS. The measurements of V_{OC} of Reference Sample 2 after each temperature are shown in figure Fig.6.16. The diagonal cells previously measured were remeasured. All the measurements that gave origin to these graphs are in section 6.5.4.

1	2	3	4	
0.376	0.376	0.377		D
0.38	0.356	0.384	0.388	C
0.388	0.388	0.391	0.392	B
0.391	0.401	0.402	0.4	A

(a)RS2_RT

1	2	3	4	
0.379	0.384	0.387		D
0.379	0.379	0.387	0.392	C
0.387	0.388	0.394	0.397	B
0.387	0.393	0.396	0.398	A

(b) RS2_HLS_75 °C

1	2	3	4	
0.373	0.367	0.369		D
0.374	0.376	0.378	0.375	C
0.384	0.383	0.382	0.388	B
0.380	0.389	0.388	0.394	A

(c)RS2_HLS_90 °C

1	2	3	4	
0.380	0.379	0.382		D
0.375	0.375	0.380	0.385	C
0.379	0.381	0.383	0.386	B
0.390	0.391	0.391	0.389	A

(d) RS2_HLS_112 °C

1	2	3	4	
0.366	0.369	0.317		D
0.371	0.377	0.352	0.324	C
0.383	0.384	0.381	0.354	B
0.337	0.391	0.389	0.395	A

(e) RS2_HLS_145 °C

Figure 6.16: V_{OC} of the sample RS2 before (RT) and after Heat-Light Soaking at 75 °C, 90 °C, 112 °C and 145 °C.

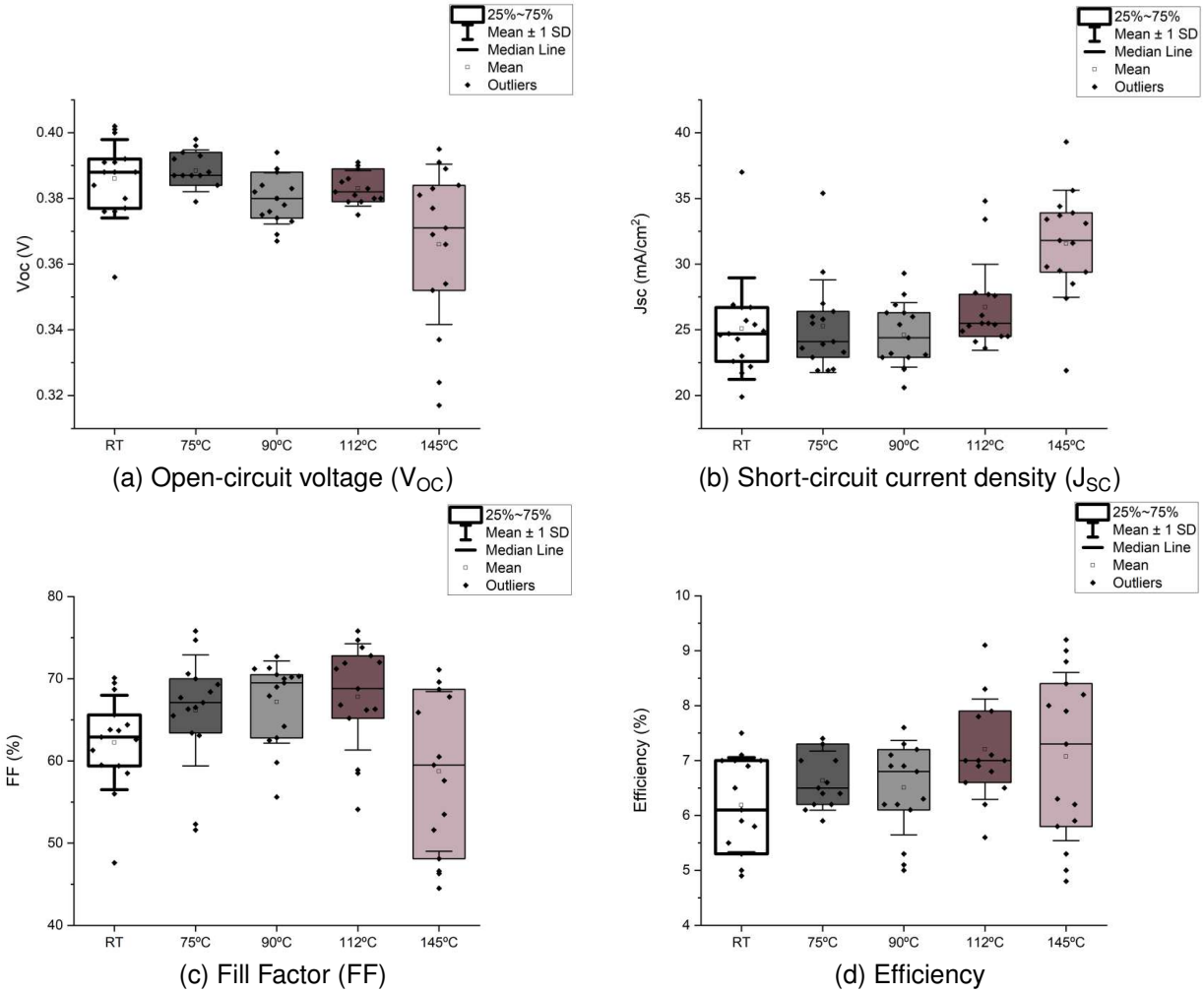

(a) Open-circuit voltage (V_{OC})

(b) Short-circuit current density (J_{SC})

(c) Fill Factor (FF)

(d) Efficiency

Figure 6.17: Solar cell basic parameters of reference sample RS2 before and after Heat-Light Soaking at RT, 75 ºC, 90 ºC, 112 ºC and 145 ºC.

	V_{OC}(V)	J_{SC}(mA/cm^2)	FF(%)	Efficiency(%)
RS2_RT Mean	0.386±0.012	25.1±3.9	62.2±5.7	6.2±0.9
RS2_HLS_75 ºC Mean	0.388±0.006	25.3±3.5	66.2±6.8	6.6±0.5
RS2_HLS_90 ºC Mean	0.380±0.008	24.6±2.5	67.2±5.0	6.5±0.9
RS2_HLS_112 ºC Mean	0.383±0.005	26.7±3.3	67.8±6.5	7.2±0.9
RS2_HLS_145 ºC Mean	0.366±0.024	31.6±4.1	58.7±9.7	7.1±1.5

Table 6.14: Solar cell basic parameters means and standard deviations of reference sample RS2 before (RT) and after Heat-Light Soaking at 75 ºC, 90 ºC, 112 ºC and 145 ºC.

From the box-plots, it is to notice that the highest used temperature is the one that shows a change in the solar cell basic parameters: a decrease of the V_{OC} of around 0.020V and an increase of the J_{SC} of $\sim$6.5mA/cm^2. These variations are in relation to the values of the Reference Sample 2 before the HLS. The FF presents a decrease and the efficiency an increase maybe due to the increase in J_{SC}. However, their averages are in the range of values that RS2_RT might have. Thus, we can consider that the efficiency and FF did not show a significant change. For the other temperatures, the sample shows no change in relation to the sample with no HLS treatment.

J-V curves and solar cell basic parameters

The J-V curves of the selected cell (A2) before (RT) and after the Heat-Light Soaking treatment at 75 °C, 90 °C, 112 °C and 145 °C are presented in Fig.6.18, along with the basic solar cell parameters in table 6.15.

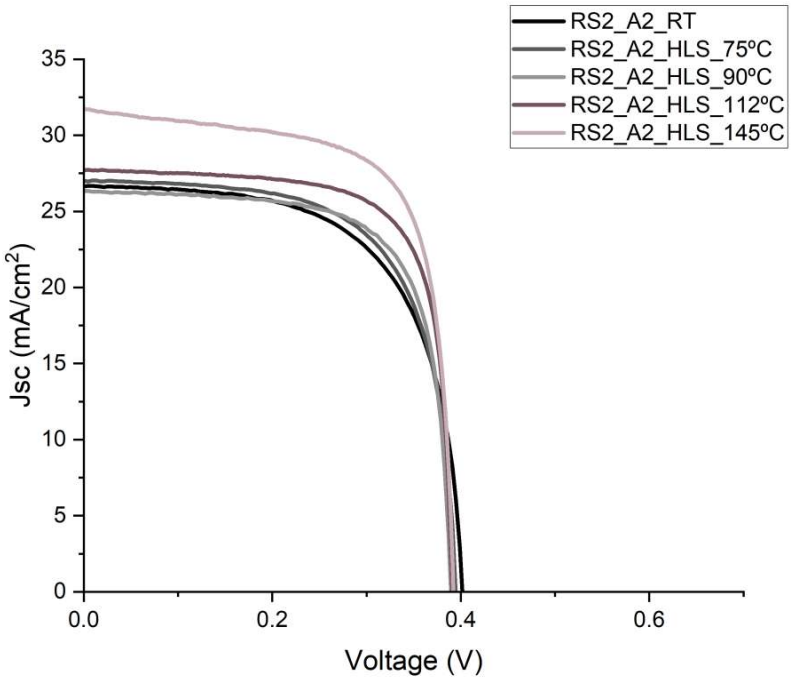

Figure 6.18: J-V curves of cell RS2_A2 before (RT) and after HLS at 75 °C, 90 °C, 112 °C and 145 °C.

	V_{OC}(V)	Jsc(mA/cm$_2$)	FF(%)	Efficiency(%)
RS2_A2_RT	0.401	26.7	63.7	7.0
RS2_A2_HLS_75 °C	0.393	27.0	66.5	7.3
RS2_A2_HLS_90 °C	0.389	26.3	69.0	7.3
RS2_A2_HLS_112 °C	0.391	27.7	73.8	8.3
RS2_A2_HLS_145 °C	0.391	31.6	71.0	9.2

Table 6.15: Basic solar cell parameters before (RT) and after Heat-Light Soaking at 75 °C, 90 °C, 112 °C and 145 °C.

The results observed on cell A2 show the following: a decrease of around 0.010V of the V_{OC} and an increase of $\approx$ 4.9 mA/cm^2, 7.3% and 2.2% in J_{SC}, FF and efficiency respectively were measured for the last temperature comparing to the sample before the HLS. The tendency of the FF is the opposite of the one registered by the box-plots, where the FF mean decreased with temperature, although not significantly. For RS2_A2 as the HLS temperature increases, all the solar cell basic parameters get an improvement, except the V_{OC}. Since the percentage variation of J_{SC} is larger comparing to FF, we can hypothesize that the efficiency increase was mainly due to the variation in J_{SC}. The balance between V_{OC} decrease and J_{SC} increase seems to be essential to improve the efficiency, since there is a trade-off between these two parameters, also shown in the box-plots.

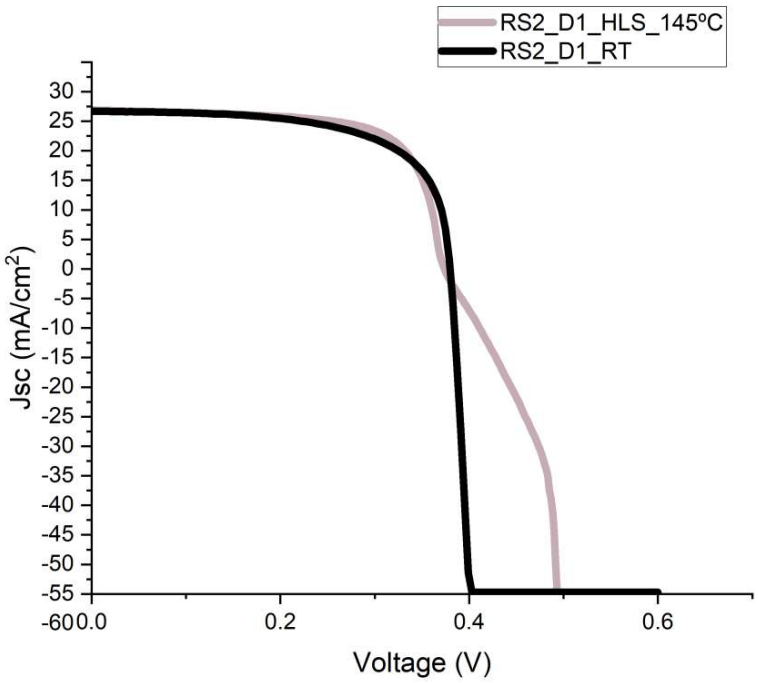

Figure 6.19: J-V curve of cell RS2_D1 before HLS treatment (RT) and after HLS at 145 °C.

For some cells after the HLS treatment at 145 °C, the J-V curve gained the shape of an S-kink. This is illustrated in Fig.6.19 , where the J-V curve of the cell D1 is represented and this phenomenon is very evident. This effect of the S-kink shape will be discussed in the discussion section.

External quantum efficiency

EQE measurements of the RS2 sample were taken before and after the Heat-Light Soaking at several temperatures. The EQE curves shown in Fig.6.20 are also of the cell A2.

	RS2_A2_RT	**RS2_A2_HLS_75 °C**	**RS2_A2_HLS_90 °C**	**RS2_A2_HLS_112 °C**	**RS2_A2_HLS_145 °C**
$J_{SC,EQE}$(mA/cm^2)	28.41	29.0	29.2	29.6	22.3
$J_{SC,JV}$(mA/cm^2)	26.7	27.0	26.3	27.7	31.6

Table 6.16: Comparison of J_{SC} measured in the Solar Cell Quantum Efficiency System and in the Solar Simulator for cell RS2_A2.

The $J_{sc,EQE}$ does not follow all the trends given by $J_{sc,JV}$. In particular the EQE curve at 145 °C has an unexpected behaviour. The $J_{sc,EQE}$ decreases, which would not be expected. This might happen due to the reasons listed in Chapter 5.4.2. Besides, the cell was subjected to a cumulative heat and light soaking, which may have caused some irreversible effects.

However, for the remaining curves we can conclude that there is an increase from 700nm to 1050nm that may correspond to a reduction in recombination losses in the CIGS layer and a decrease from 400nm to 600nm that implies a reduction in the absorption and collection of photons in the CdS layer and in the CdS/CIGS interface as the temperature increases[84]. The shape of the EQE curve varies,

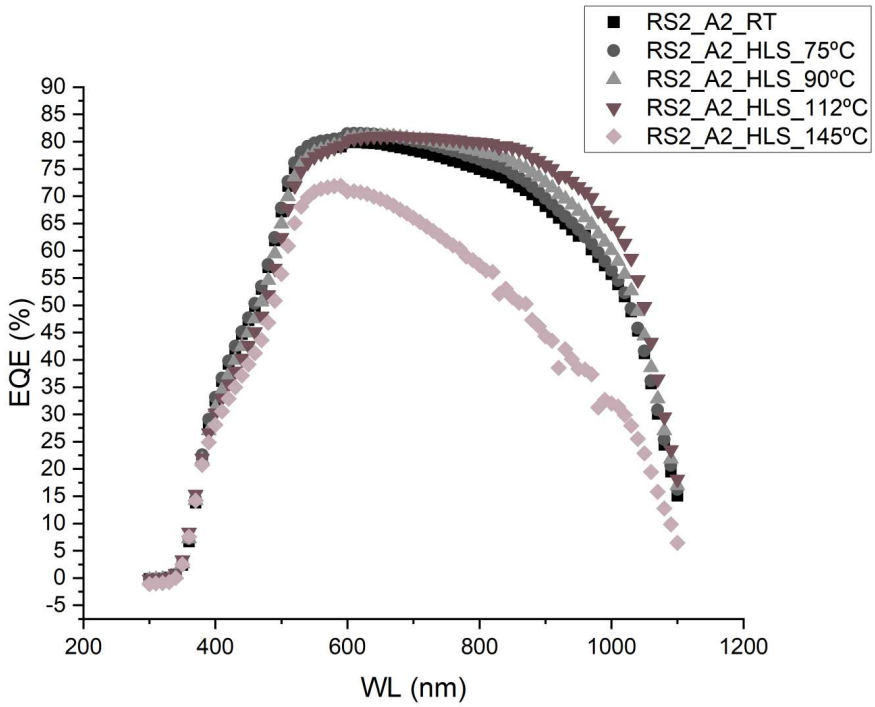

Figure 6.20: EQE curves of cell RS2_A2 before (RT) and after Heat-Light Soaking at 75 °C, 90 °C, 112 °C and 145 °C.

with its values becoming more similar from 600 nm to 850 nm as the temperature increases.

6.4.2 PDT_SC1

The denomination used in the graphs as well as the temperatures that were put in the heater and the respective temperatures of the sample measured by a thermocouple are summarized in table 6.17.

	PDT_SC1 RT	PDT_SC1_HLS_75 °C	PDT_SC1_HLS_90 °C	PDT_SC1_HLS_112 °C	PDT_SC1_HLS_145 °C
Heat-light soaking treatment		X	X	X	X
Temperature indicated in the heater(°C)	0	100	130	150	200
Temperature of the sample(°C)	25	75	90	112	145

Table 6.17: Sample denomination for each temperature.

J-V measurements

The box-plots of the basic solar cell parameters extracted from the J-V measurements of sample PDT_SC1 are represented in Fig.6.22 and its means and standard deviations in Table 6.18. In the horizontal axis of the box-plots, the temperatures of the HLS are indicated. RT stands for Room Temperature, the temperature of the sample before doing the HLS. The measurements of V_{OC} of PDT_SC1 after each temperature are shown in figure Fig.6.21. All the measurements that gave origin to these graphs are in Section 6.5.5.

1		0.483	0.332	0.350
2	0.487	0.485	0.484	0.477
3	0.484	0.480	0.481	0.478
4	0.429	0.484	0.482	0.426
	A	B	C	D

(a) PDT_SC1 RT

1		0.473	0.450	0.304
2	0.476	0.482	0.476	0.465
3	0.480	0.461	0.471	0.467
4	0.362	0.465	0.457	0.408
	A	B	C	D

(b) PDT_SC1_HLS_75 °C

1		0.472	0.380	0.126
2	0.474	0.472	0.468	0.456
3	0.476	0.464	0.466	0.463
4	0.367	0.461	0.453	0.439
	A	B	C	D

(c)PDT_SC1_HLS_90 °C

1		0.477	0.306	0.141
2	0.471	0.473	0.469	0.469
3	0.471	0.454	0.465	0.463
4	0.269	0.462	0.460	0.431
	A	B	C	D

(d) PDT_SC1_HLS_112 °C

1		0.460	0.333	0.151
2	0.421	0.437	0.440	0.451
3	0.390	0.380	0.431	0.455
4	0.376	0.445	0.460	0.437
	A	B	C	D

(e) PDT_SC1_HLS_145 °C

Figure 6.21: V_{OC} of the sample PDT_SC1 before (RT) and after Heat-Light Soaking at temperatures 75 °C, 90 °C, 112 °C and 145 °C.

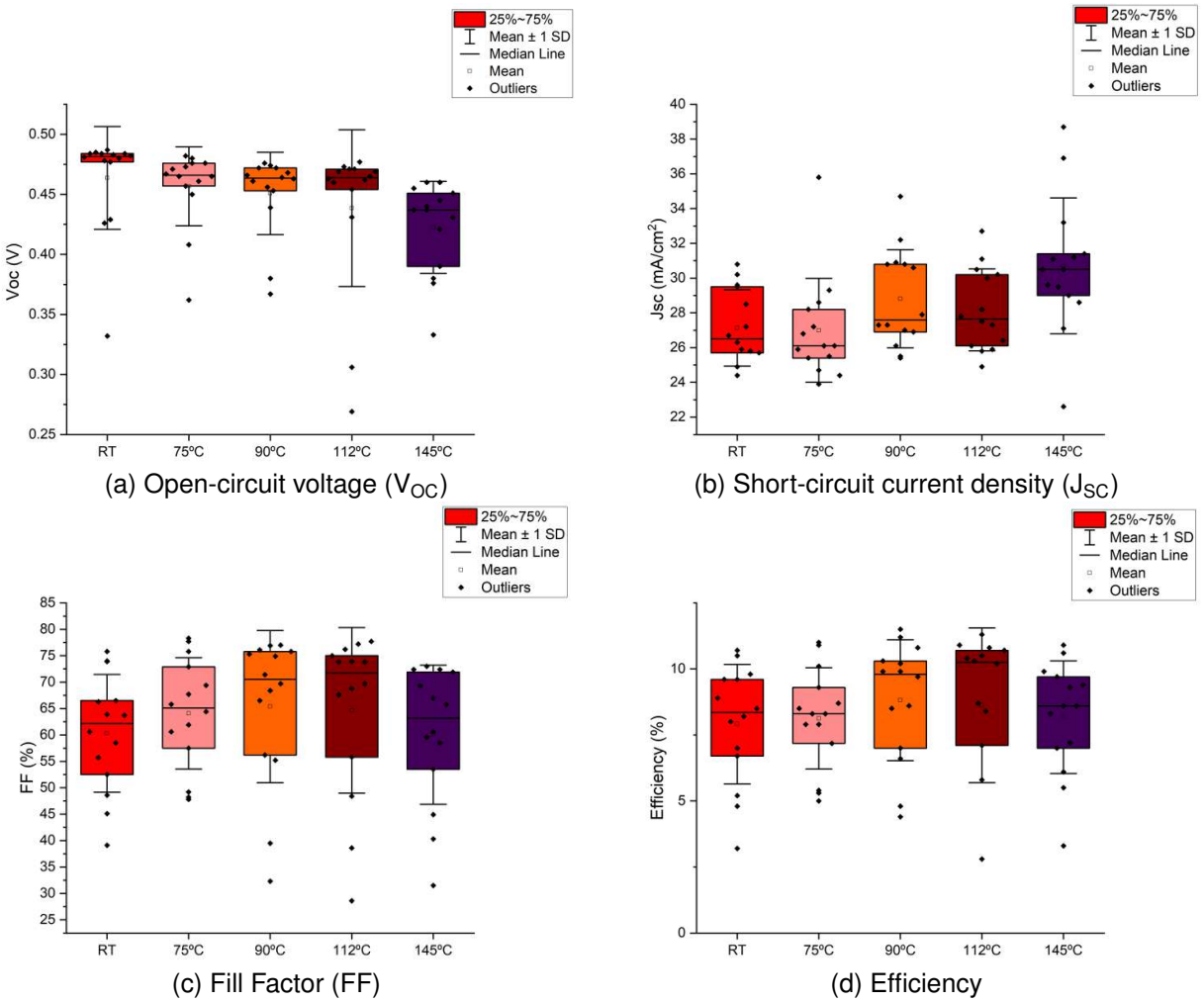

(a) Open-circuit voltage (V_{OC})

(b) Short-circuit current density (J_{SC})

(c) Fill Factor (FF)

(d) Efficiency

Figure 6.22: Solar cell basic parameters of sample PDT_SC1 before (RT) and after Heat-Light Soaking at temperatures 75 °C, 90 °C, 112 °C and 145 °C.

	V_{OC}(V)	J_{SC}(mA/cm^2)	FF(%)	Efficiency(%)
PDT_SC1_RT Mean	0.464±0.043	27.1±2.2	60±11	7.9±2.3
PDT_SC1_HLS_75 °C Mean	0.457±0.033	27.0±3.0	64.±11	8.1±1.9
PDT_SC1_HLS_90 °C Mean	0.451±0.034	28.8±2.8	65±14	8.8±2.3
PDT_SC1_HLS_112 °C Mean	0.439±0.065	28.2±2.4	65±16	8.6±2.9
PDT_SC1_HLS_145 °C Mean	0.423±0.038	30.7±3.9	60±13	7.6±2.9

Table 6.18: Solar cell basic parameters means and standard deviations of sample PDT_SC1 before (RT) and after Heat-Light Soaking at temperatures 75 °C, 90 °C, 112 °C and 145 °C.

It is observed that the V_{OC} and J_{SC} of the PDT_SC1 sample with HLS 145 °C differ slightly from those of the same sample without the HLS process (RT conditions), decreasing by approximately 0.041V and increasing around 3.6 mA/cm^2. However, the change is relatively small, considering the standard deviations. The FF and Efficiency values do not significantly differ, due to large associated errors. Notably, the PDT_SC1 sample has larger standard deviations compared to RS2, which may be related to the distribution of the Cs in the sample.

J-V curves and solar cell basic parameters

The J-V curves of the selected cell (A3) before and after the Heat-Light Soaking treatment at 75 °C, 90 °C, 112 °C and 145 °C is presented in Fig.6.23 , along with the basic solar cell parameters in Table 6.19.

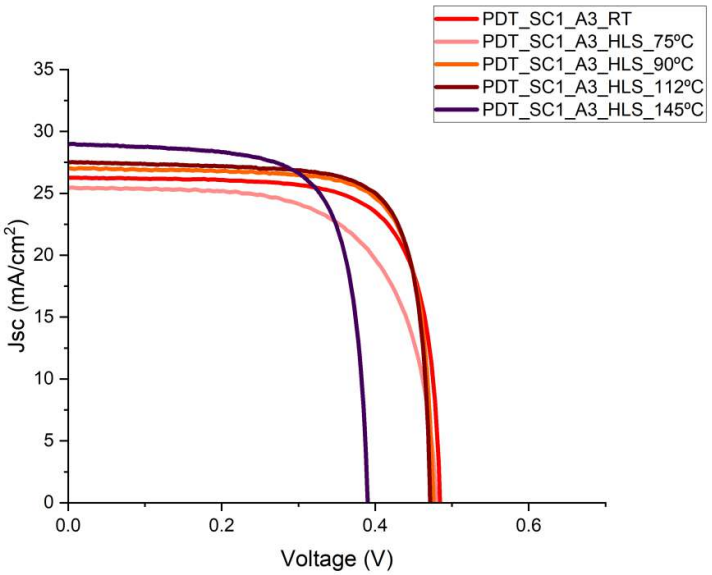

Figure 6.23: J-V curves of cell PDT_SC1_A3 before (RT) and after Heat-Light Soaking at temperatures 75 °C, 90 °C, 112 °C and 145 °C.

	V_{OC}(V)	J_{SC}(mA/cm^2)	FF(%)	Efficiency(%)
PDT_SC1_A3_RT	0.484	26.3	74.0	9.6
PDT_SC1_A3_HLS_75 °C	0.480	25.4	65.8	8.3
PDT_SC1_A3_HLS_90 °C	0.476	27.0	76.9	10.2
PDT_SC1_A3_HLS_112 °C	0.471	27.5	77.2	10.5
PDT_SC1_A3_HLS_145 °C	0.390	29.0	72.3	8.6

Table 6.19: Basic solar cell parameters before and after Heat-Light Soaking at several temperatures.

The solar cell basic parameters show a considerable change at 145 °C HLS, namely a decrease in V_{OC}, an increase in J_{SC} and a decrease in efficiency of around 0.094V, 2.7mA/cm^2 and 1.0% respectively. This is also reflected in the different shape of the J-V curve for PDT_SC1_A3_HLS_145 °C as shown in Fig.6.23. The decrease in V_{OC} might be the responsible for the decrease in efficiency. In contrary to what happens in RS2_A2, the decrease in V_{OC} prevails over the increase of J_{SC} for the highest HLS temperature (PDT_SC1_A3_HLS_145 °C) . Nonetheless, for the temperatures bellow (except for 75 °C), the tendency was the decrease of V_{OC}, an increase of J_{SC}, the increase of FF and the increase in efficiency. This suggests that the optimal temperature for performing HLS may be around 112 °C. The mean values of efficiency from the box-plots in Table 6.18 support this, but only if the standard deviation is not considered. Yet, this is just an hypothesis, since there is a high variability of the parameters for this sample. Conducting a similar study with a sample that has a smaller standard deviation for its cells could help in understanding if this is the correct interpretation.

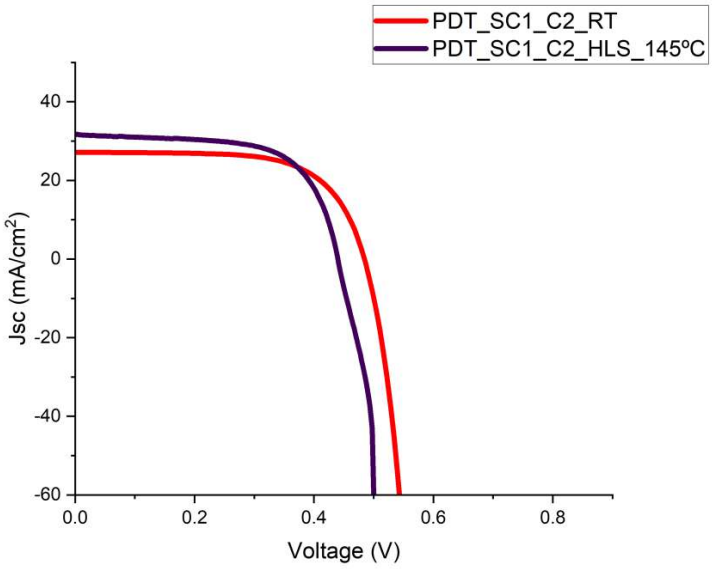

Figure 6.24: J-V curve of cell PDT_SC1_C2 before the HLS treatment (RT) and after HLS at 145 °C.

The S-kink phenomenon referred concerning some of the RS2_HLS_145 °C cells also took place in some cells of sample PDT_SC1_HLS_145 °C. Nevertheless, these revealed a less evident S-kink, as it is possible to confirm by the example of cell C2 in Fig. 6.24.

External Quantum Efficiency

EQE measurements of the PDT_SC1 sample were taken before and after Heat-Light Soaking. The EQE curves shown in Fig.6.25 are of the cell A3.

	PDT_SC1_A3_RT	PDT_SC1_A3_HLS_75 °C	PDT_SC1_A3_HLS_90 °C_A3	PDT_SC1_A3_HLS_112 °C	PDT_SC1_A3_HLS_145 °C
$J_{sc,EQE}$(mA/cm^2)	27.2	26.5	28.3	28.7	29.6
$J_{sc,JV}$(mA/cm^2)	26.3	25.4	27.0	27.5	29.0

Table 6.20: Comparison of J_{SC} measured in the Solar Cell Quantum Efficiency System and in the Solar Simulator for PDT_SC1_A3.

The $J_{SC,EQE}$ follows the tendency of $J_{SC,JV}$. The increase of the J_{SC} mean might be due to the increase of EQE from 600nm to 1050 nm, corresponding to a better absorption of photons in the CIGS layer and respective generated carriers collection. In contrast to what happens in RS2, the EQE seems to increase slightly from 400nm to 600nm, meaning that with the Cs-PDT the absorption of photons in the CdS layer and CdS/CIGS interface and respective collection of generated charge carriers after the HLS gets better.

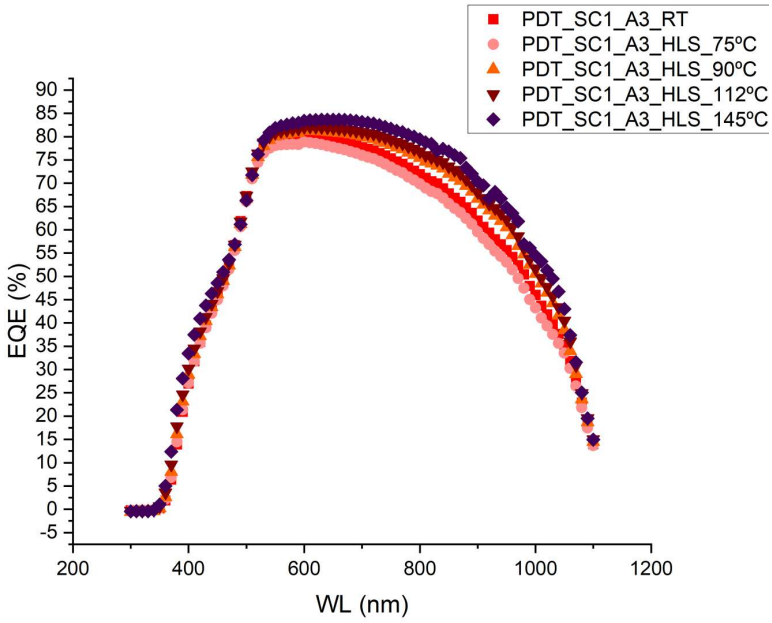

Figure 6.25: EQE curves of cell PDT_SC1_A3 before (RT) and after Heat-Light Soaking at temperatures 75 °C, 90 °C, 112 °C and 145 °C.

6.4.3 Discussion of all the results of the Heat-Light Soaking Treatment

Both non-treated and Cs-treated samples show a decrease of the V_{OC}, the percentage of change was about 5.2% and 8.8%, and an increase of the J_{SC} where the percentage of change was around 25.9% and 13.3%, for the highest temperature of 145 °C. The same occurred for the selected cells, where this percentage is 2.5% and 19.4% respectively for the V_{OC} decrease and 18.4% and 10.3% for the J_{SC} increase. The selected cells of both treated and non-treated samples present similar tendencies in all the solar cell parameters until the temperature of 112 °C. Thus, the mechanism behind these results may be similar for both samples and hence it depends on the cell fabrication procedure. Considering that a trade-off, the decrease of V_{OC} and increase of J_{SC}, the opposite that is reported in literature [30] [29], is verified in both selected cells (PDT_SC1_A3 and RS2_A2) and in the results of sample RS2 and sample PDT_SC1 , it is possible to speculate that the contrary process occurs, the decrease in the net holes concentration and the increase of the space-charge region, contributing to an increase of the J_{SC} and decrease of the V_{OC}. [29] To check this hypothesis a capacitance-voltage measurement should be done. The FF and efficiency of both samples did not show significant changes due to their large errors. However, for the individual cells shown, the FF and Efficiency increased until the temperature of 145 °C for the non-treated cell and 112 °C for the Cs-treated cell. The balance between the V_{OC} decrease and J_{SC} increase reveals, thus, to be very important to attain an efficiency improvement through this treatment.

The increase in the number of holes is usually attributed to the V_{Se}-V_{Cu} defect complex, that with higher temperatures, converts into its acceptor configuration with the creation of a hole[86]. However, according to the hypothesis proposed, a reduction of the number of holes with temperature occurs, which

may suggest that the behaviour observed is not related to the V_{Se}-V_{Cu} defect complex. To discern if this complex has any influence in the results, a new set of samples grown with a Na treatment and grown under ”Se-rich” and ”Cu-rich” conditions could be done, as it was suggested that growing cells in these conditions supresses the formation of the divacancy complex in the absorber[30].

On the other hand, it is possible that higher temperatures may have allowed the diffusion of Na and K from the SLG substrate to near the Mo back contact, which may have helped to increase carrier collection, increasing the J_{SC}[30]. However, these variations after HLS were not reported before and further investigation is necessary to understand their causes.

The EQE evolution with temperature for cell RS2_A2 and PDT_SC1_A3 exhibits differences, namely the opposite tendency in EQE from 400nm to 600nm, a decrease and an increase respectively. This may indicate that the absorption of photons in the CdS and CdS/CIGS interface and collection of the respective photo-generated carriers has changed with the alkali treatment. Maybe there was a reduction of recombination in this layer/interface of the solar cell due to passivation of recombination centers[72] by Cs atoms, enhanced by the akaline metal migrations caused by the photo-induced field and higher temperatures, [72] [17] which contributed to a greater diffusion length of the electrons and consequently to a greater collection of carriers.

A S-kink appeared for some cells after the HLS at 145 ^{o}C and it was more pronounced for the non-treated sample than for the treated sample. This S-kink is usually caused by the formation of a p+/p junction in the absorber due to the excess of holes [88] created with the conversion of the V_{Se}-V_{Cu} defect complex from donor to acceptor. As previously referred, this conversion is enhanced with higher temperature, so it would be possible that in the case of the HLS treatment performed in this thesis, that would have happened[86]. However, this hypothesis contradicts the possibility of reduction of holes, mentioned to justify the behaviour of V_{OC} and J_{SC}. If the conversion from donor to acceptor occurred, then the accumulation of holes (resultant from this conversion) would form the p+ ”defected” layer, responsible for the J-V distortion. This distortion is said to the be reduced by blue light that is usually absorbed in the CdS. Since the collection and absorption of photons corresponding to blue light increases with temperature for the Cs-treated sample and decreases for the non-treated sample, it makes sense that the S-kink is also less pronounced in the Cs-treated sample[88][89].

6.5 J-V Measurements of all the cells

In this section, the basic solar cell parameters of all the cells are presented. The name of the subsections will correspond to the name of the sections in which these measurements were used to do the box-plots. Throughout this section some values are highlighted in red because they are higher than what is desirable for these cells. The cell/s in green are the ones that present the best efficiency of that sample and the ones highlighted in yellow are the cells of whose J-V and EQE measurements were presented in Chapter 6.

6.5.1 $CsCo_3$-solution post deposition treatment of CIGS

The color code of the samples is according to table 6.1.

Reference cells

	D	C	B	A
4				
3	0.367			
2		0.374	0.373	0.384
1			0.382	

(a) Reference Sample 1

1	2	3	4	
				D
0.379	0.388			C
		0.396		B
			0.403	A

(b) Reference Sample 2

A				0.381
B		0.396	0.356	
C	0.412			
	1	2	3	4

(c) Reference Sample 3

			0.406	1
	0.409	0.409		2
0.415				3
A	B	C	D	

(d) Reference Sample 4

Figure 6.26: V_{OC} measurements in Volts of Reference samples 1, 2, 3 and 4.

	D	C	B	A
4				
3	23.9			
2		24.7	24.1	24.7
1			28.6	

(a) Reference Sample 1

1	2	3	4	
				D
27.5	28.1			C
		27.8		B
			26.4	A

(b) Reference Sample 2

A				28.0
B		25.6	26.6	
C	25.0			
	1	2	3	4

(c) Reference Sample 3

			27.5	1
	31.5	31.3		2
25.9				3
A	B	C	D	

(d) Reference Sample 4

Figure 6.27: J_{SC} measurements in mA/cm^2 of Reference Samples 1, 2, 3 and 4.

	D	C	B	A
4				
3	52.0			
2		58.9	54.5	53.6
1			46.3	

(a) Reference Sample 1

1	2	3	4	
				D
66.1	55.6			C
		55.2		B
			53.4	A

(b) Reference Sample 2

A				52.6
B		53.1	53.2	
C	63.7			
	1	2	3	4

(c) Reference Sample 3

			58.7	1
	55.1	56.6		2
54.5				3
A	B	C	D	

(d) Reference Sample 4

Figure 6.28: Fill Factor measurements of Reference Samples 1, 2, 3 and 4.

	D	C	B	A
4				
3	4.6			
2		5.5	5.1	5.2
1			5.2	

(a) Reference Sample 1

1	2	3	4	
				D
7.0	6.2			C
		6.2		B
			5.8	A

(b) Reference Sample 2

A				5.7
B		5.6	5.2	
C	6.9			
	1	2	3	4

(c) Reference Sample 3

			6.7	1
	7.2	7.4		2
6.0				3
A	B	C	D	

(d) Reference Sample 4

Figure 6.29: Efficiency measurements of Reference samples 1, 2, 3 and 4.

Treated samples

1		0.483	0.332	0.350
2	0.487	0.485	0.484	0.477
3	0.484	0.480	0.481	0.478
4	0.429	0.484	0.482	0.426
	A	B	C	D

(a) PDT_SC1

1	2	3	4	
	0.423	0.487	0.466	A
0.470	0.478	0.480	0.478	B
0.475	0.481	0.479	0.470	C
0.438	0.492	0.479	0.432	D

(b) PDT_SC2a

	4	3	2	1
A		0.493	0.491	0.473
B	0.499	0.493	0.489	0.485
C	0.482		0.492	0.473
D	0.502	0.505	0.504	0.446

(c) PDT_SC2b

Figure 6.30: V_{OC} measurements in Volts of samples PDT_SC1, PDT_SC2a and PDT_SC2b.

1		25.8	24.4	7.9
2	25.9	26.7	27.2	25.7
3	26.3	30.8	29.6	28.5
4	24.4	29.5	30.2	24.9
	A	B	C	D

(a) PDT_SC1

1	2	3	4	
	28.1	28.1	24.4	A
28.8	28.9	27.7	28.3	B
30.3	27.5	28.6	30.3	C
26.9	30.0	31.8	63.7	D

(b) PDT_SC2a

	4	3	2	1
A		24.4	28.5	24.7
B	36.0	28.3	29.0	30.0
C	44.2		31.0	37.3
D	28.0	31.2	32.1	26.9

(c) PDT_SC2b

Figure 6.31: J_{SC} measurements in mA/cm^2 of samples PDT_SC1, PDT_SC2a and PDT_SC2b.

1		52.5	39.1	25.1
2	63.9	60.6	66.5	55.7
3	74.0	63.7	73.9	75.8
4	45.1	58.5	66.3	48.6
	A	B	C	D

(a) PDT_SC1

1	2	3	4	
	35.9	54.0	44.2	A
52.3	68.0	78.8	67.4	B
69.6	68.2	81.4	63.6	C
43.0	57.5	67.0	41.0	D

(b) PDT_SC2a

	4	3	2	1
A		60.0	70.7	62.2
B	56.7	65.5	68.7	66.6
C	44.9		66.4	55.9
D	50.7	60.3	60.7	48.7

(c) PDT_SC2b

Figure 6.32: Fill Factor measurements of samples PDT_SC1, PDT_SC2a and PDT_SC2b.

1		6.7	3.2	0.7
2	8.2	8.0	8.9	7.0
3	9.6	9.6	10.7	10.5
4	4.8	8.5	9.8	5.2
	A	B	C	D

(a) PDT_SC1

1	2	3	4	
	4.4	7.5	5.1	A
7.2	9.6	10.7	9.3	B
10.2	9.2	11.4	9.2	C
5.2	8.7	10.4	11.5	D

(b) PDT_SC2a

	4	3	2	1
A		7.4	10.1	7.4
B	10.3	9.3	10.0	9.9
C	9.8		10.4	10.1
D	7.3	9.8	10.1	6.0

(c) PDT_SC2b

Figure 6.33: Efficiency measurements of samples PDT_SC1, PDT_SC2a and PDT_SC2b.

6.5.2 Light Soaking

The color code of the samples is according to table 6.5.

1	2	3	4	
	0.423	0.487	0.466	A
0.470	0.478	0.480	0.478	B
0.475	0.481	0.479	0.470	C
0.438	0.492	0.479	0.432	D

(a) PDT_SC2a

1	2	3	4	
	0.322	0.481	0.453	A
0.462	0.476	0.477	0.458	B
0.474	0.481	0.480	0.472	C
0.317	0.470	0.459	0.453	D

(b) PDT_SC2a_LS60'

Figure 6.34: V_{OC} measurements in Volts of sample PDT_SC2a before and after Light Soaking.

1	2	3	4	
	28.1	28.1	24.4	A
28.8	28.9	27.7	28.3	B
30.3	27.5	28.6	30.3	C
26.9	30.0	31.8	63.7	D

(a) PDT_SC2a

1	2	3	4	
	38.8	28.0	25.8	A
28.2	29.7	27.6	50.2	B
30.1	28.8	30.3	30.5	C
32.3	35.0	39.2	30.0	D

(b) PDT_SC2a_LS60'

Figure 6.35: J_{SC} measurements in mA/cm^2 of sample PDT_SC2a before and after Light Soaking.

1	2	3	4	
	35.9	54.0	44.2	A
52.3	68.0	78.8	67.4	B
69.6	68.2	81.4	63.6	C
43.0	57.5	67.0	41.0	D

(a) PDT_SC2a

1	2	3	4	
	30.3	57.0	47.5	A
52.2	71.6	76.4	45.4	B
71.6	77.9	78.3	72.2	C
29.7	57.9	46.5	38.6	D

(b) PDT_SC2a_LS60'

Figure 6.36: Fill Factor measurements of sample PDT_SC2a before and after Light Soaking.

1	2	3	4	
	4.4	7.5	5.1	A
7.2	9.6	10.7	9.3	B
10.2	9.2	11.4	9.2	C
5.2	8.7	10.4	11.5	D

(a) PDT_SC2a

1	2	3	4	
	3.9	7.9	5.7	A
7.0	10.4	10.3	10.7	B
10.5	11.1	11.7	10.7	C
3.1	9.8	8.4	5.4	D

(b) PDT_SC2a_LS60'

Figure 6.37: Efficiency measurements of sample PDT_SC2a before and after Light Soaking.

6.5.3 Heat Soaking

The color code of the samples is according to table 6.9.

	4	3	2	1
A		0.493	0.491	0.473
B	0.499	0.493	0.489	0.485
C	0.482		0.492	0.473
D	0.502	0.505	0.504	0.446

(a) PDT_SC2b

	4	3	2	1
A		0.484	0.486	0.411
B		0.492	0.484	0.479
C	0.468	0.484	0.332	0.466
D	0.489	0.490	0.483	0.478

(b)PDT_SC2b_HS30'

Figure 6.38: V_{OC} measurements in Volts of sample PDT_SC2b before and after Heat Soaking.

	4	3	2	1
A		24.4	28.5	24.7
B	36.0	28.3	29.0	30.0
C	44.2		31.0	37.3
D	28.0	31.2	32.1	26.9

(a) PDT_SC2b

	4	3	2	1
A		34.2	28.1	34.1
B		31.7	29.4	33.9
C	31.7	36.4	44.7	36.1
D	30.1	31.2	32.0	23.3

(b)PDT_SC2b_HS30'

Figure 6.39: J_{SC} measurements in mA/cm^2 of sample PDT_SC2b before and after Heat Soaking.

	4	3	2	1
A		60.0	70.7	62.2
B	56.7	65.5	68.7	66.6
C	44.9		66.4	55.9
D	50.7	60.3	60.7	48.7

(a) PDT_SC2b

	4	3	2	1
A		58.9	67.0	33.8
B		65.4	69.4	62.5
C	45.9	51.7	25.7	52.1
D	63.0	66.7	64.3	54.3

(b)PDT_SC2b_HS30'

Figure 6.40: Fill Factor measurements of sample PDT_SC2b before and after Heat Soaking.

	4	3	2	1
A		7.4	10.1	7.4
B	10.3	9.3	10.0	9.9
C	9.8		10.4	10.1
D	7.3	9.8	10.1	6.0

(a) PDT_SC2b

	4	3	2	1
A		9.9	9.5	4.9
B		10.5	10.1	10.4
C	7.0	9.4	4.0	8.7
D	9.5	10.5	10.3	6.3

(b)PDT_SC2b_HS30'

Figure 6.41: Efficiency measurements of sample PDT_SC2b before and after Heat Soaking.

6.5.4 Heat-Light Soaking

Reference Sample 2

The color code of the samples is according to table 6.13.

1	2	3	4	
0.376	0.376	0.377		D
0.38	0.356	0.384	0.388	C
0.388	0.388	0.391	0.392	B
0.391	0.401	0.402	0.4	A

(a)RS2_RT

1	2	3	4	
0.379	0.384	0.387		D
0.379	0.379	0.387	0.392	C
0.387	0.388	0.394	0.397	B
0.387	0.393	0.396	0.398	A

(b) RS2_HLS_75 °C

1	2	3	4	
0.373	0.367	0.369		D
0.374	0.376	0.378	0.375	C
0.384	0.383	0.382	0.388	B
0.380	0.389	0.388	0.394	A

(c)RS2_HLS_90 °C

1	2	3	4	
0.380	0.379	0.382		D
0.375	0.375	0.380	0.385	C
0.379	0.381	0.383	0.386	B
0.390	0.391	0.391	0.389	A

(d) RS2_HLS_112 °C

1	2	3	4	
0.366	0.369	0.317		D
0.371	0.377	0.352	0.324	C
0.383	0.384	0.381	0.354	B
0.337	0.391	0.389	0.395	A

(e) RS2_HLS_145 °C

Figure 6.42: V_{OC} measurements in Volts of sample RS2 before (RT) and after Heat-Light Soaking at temperatures 75 °C, 90 °C, 112 °C and 145 °C.

1	2	3	4	
21.7	24.6	22.2		D
24.9	23.0	22.6	19.9	C
25.4	26.9	26.7	24.7	B
37.0	26.7	25.7	24.3	A

(a)RS2_RT

1	2	3	4	
22.0	23.6	23.3		D
29.4	21.9	21.9	22.9	C
25.5	26.0	26.4	24.1	B
35.5	27.0	25.8	23.9	A

(b) RS2_HLS_75 °C

1	2	3	4	
23.2	23.1	22.9		D
22.0	29.3	22.1	20.6	C
26.0	26.3	27.7	25.4	B
22.9	26.3	26.9	24.4	A

(c)RS2_HLS_90 °C

1	2	3	4	
25.3	24.5	24.8		D
23.6	24.1	24.5	27.8	C
33.4	27.6	34.8	25.4	B
25.5	27.7	26.1	25.5	A

(d) RS2_HLS_112 °C

1	2	3	4	
21.9	31.8	33.4		D
29.8	33.7	33.1	34.4	C
29.4	33.9	39.3	35.6	B
28.5	31.6	29.5	27.4	A

(e) RS2_HLS_145 °C

Figure 6.43: J_{SC} measurements in mA/cm^2 of sample RS2 before (RT) and after Heat-Light Soaking at temperatures 75 °C, 90 °C, 112 °C and 145 °C.

1	2	3	4	
62.6	61.3	70.1		D
56.0	58.5	59.5	62.9	C
63.8	64.4	69.5	59.4	B
47.6	63.7	65.6	68.7	A

(a)RS2_RT

1	2	3	4	
75.8	74.7	69.3		D
51.7	68.4	70.6	65.5	C
63.1	70.0	67.7	63.4	B
52.3	66.5	66.3	67.1	A

(b) RS2_HLS_75 °C

1	2	3	4	
69.5	71.2	70.3		D
62.5	59.8	70.2	64.2	C
70.0	72.7	62.8	67.9	B
55.6	69.0	70.5	71.3	A

(c)RS2_HLS_90 °C

1	2	3	4	
66.3	72.0	71.2		D
66.8	72.8	71.9	58.5	C
58.9	75.8	65.2	66.2	B
54.1	73.8	74.7	68.8	A

(d) RS2_HLS_112 °C

1	2	3	4	
68.7	59.5	46.3		D
53.5	65.9	51.6	46.6	C
67.8	60.5	57.6	44.5	B
48.1	71.1	69.5	69.6	A

(e) RS2_HLS_145 °C

Figure 6.44: Fill Factor measurements of sample RS2 before (RT) and after Heat-Light Soaking at temperatures 75 °C, 90 °C, 112 °C and 145 °C.

1	2	3	4	
5.3	5.8	6.1		D
5.5	4.9	5.3	5.0	C
6.5	7.0	7.5	5.9	B
7.1	7.0	7.0	6.9	A

(a)RS2 RT

1	2	3	4	
6.5	7.0	6.4		D
5.9	5.9	6.2	6.1	C
6.4	7.3	7.3	6.3	B
7.4	7.3	7.0	6.6	A

(b) RS2_HLS_75 °C

1	2	3	4	
6.2	6.3	6.2		D
5.3	6.8	6.1	5.1	C
7.2	7.6	6.9	6.9	B
5.0	7.3	7.6	7.1	A

(c)RS2_HLS_90 °C

1	2	3	4	
66.3	72.0	71.2		D
66.8	72.8	71.9	58.5	C
58.9	75.8	65.2	66.2	B
54.1	73.8	74.7	68.8	A

(d) RS2_HLS_112 °C

1	2	3	4	
5.8	7.3	5.0		D
6.2	8.8	6.3	5.3	C
8.0	8.2	9.0	5.9	B
4.8	9.2	8.4	7.9	A

(e) RS2_HLS_145 °C

Figure 6.45: Efficiency measurements of sample RS2 before (RT) and after Heat-Light Soaking at temperatures 75 °C, 90 °C, 112 °C and 145 °C.

6.5.5 PDT_SC1

The color code of the samples is according to table 6.17.

1		0.483	0.332	0.350
2	0.487	0.485	0.484	0.477
3	0.484	0.480	0.481	0.478
4	0.429	0.484	0.482	0.426
	A	B	C	D

(a) PDT_SC1 RT

1		0.473	0.450	0.304
2	0.476	0.482	0.476	0.465
3	0.480	0.461	0.471	0.467
4	0.362	0.465	0.457	0.408
	A	B	C	D

(b) PDT_SC1_HLS_75 °C

1		0.472	0.380	0.126
2	0.474	0.472	0.468	0.456
3	0.476	0.464	0.466	0.463
4	0.367	0.461	0.453	0.439
	A	B	C	D

(c)PDT_SC1_HLS_90 °C

1		0.477	0.306	0.141
2	0.471	0.473	0.469	0.469
3	0.471	0.454	0.465	0.463
4	0.269	0.462	0.460	0.431
	A	B	C	D

(d) PDT_SC1_HLS_112 °C

1		0.460	0.333	0.151
2	0.421	0.437	0.440	0.451
3	0.390	0.380	0.431	0.455
4	0.376	0.445	0.460	0.437
	A	B	C	D

(e) PDT_SC1_HLS_145 °C

Figure 6.46: V_{OC} in Volts sample PDT_SC1 before (RT) and after Heat-Light Soaking at temperatures 75 °C, 90 °C, 112 °C and 145 °C.

1		25.8	24.4	7.9
2	25.9	26.7	27.2	25.7
3	26.3	30.8	29.6	28.5
4	24.4	29.5	30.2	24.9
	A	B	C	D

(a) PDT_SC1 RT

1		26.1	23.9	7.8
2	24.7	25.5	26.8	25.9
3	25.4	27.2	28.6	29.3
4	35.8	26.1	28.2	24.4
	A	B	C	D

(b) PDT_SC1_HLS_75 °C

1		26.1	34.7	6.9
2	25.5	26.9	27.9	25.4
3	27.0	30.8	30.9	30.8
4	32.2	27.3	30.6	27.3
	A	B	C	D

(c)PDT_SC1_HLS_90 °C

1		25.8	30.0	4.9
2	24.9	27.3	28.2	25.9
3	27.5	32.7	30.5	31.1
4	26.1	27.8	30.2	26.4
	A	B	C	D

(d) PDT_SC1_HLS_112 °C

1		29.5	29.6	3.3
2	27.1	30.5	31.2	33.2
3	29.0	31.1	36.9	31.4
4	38.7	28.6	30.5	22.6
	A	B	C	D

(e) PDT_SC1_HLS_145 °C

Figure 6.47: J_{SC} measurements in mA/cm^2 of sample PDT_SC1 before (RT) and after Heat-Light Soaking at temperatures 75 °C, 90 °C, 112 °C and 145 °C.

1		52.5	39.1	25.1
2	63.9	60.6	66.5	55.7
3	74.0	63.7	73.9	75.8
4	45.1	58.5	66.3	48.6
	A	B	C	D

(a) PDT_SC1 RT

1		61.9	47.8	27.1
2	67.7	72.9	64.4	57.5
3	65.8	60.6	78.3	77.7
4	49.2	69.4	75.8	48.2
	A	B	C	D

(b) PDT_SC1_HLS_75 °C

1		66.5	32.3	25.4
2	68.4	74.9	71.4	55.2
3	76.9	69.7	77.0	75.8
4	39.5	76.1	75.3	56.2
	A	B	C	D

(c)PDT_SC1_HLS_90 °C

1		67.6	28.6	25.4
2	68.8	76.2	73.9	55.8
3	77.2	69.7	73.8	75.0
4	38.6	77.7	73.8	48.4
	A	B	C	D

(d) PDT_SC1_HLS_112 °C

1		58.5	31.5	23.9
2	60.6	67.0	65.7	44.9
3	72.4	69.3	59.6	72.4
4	40.3	73.0	71.9	53.5
	A	B	C	D

(e) PDT_SC1_HLS_145 °C

Figure 6.48: Fill Factor measurements of sample PDT_SC1 before (RT) and after Heat-Light Soaking at temperatures 75 °C, 90 °C, 112 °C and 145 °C.

1		6.7	3.2	0.7
2	8.2	8.0	8.9	7.0
3	9.6	9.6	10.7	10.5
4	4.8	8.5	9.8	5.2
	A	B	C	D

(a) PDT_SC1 RT

1		7.9	5.3	0.7
2	8.3	9.3	8.5	7.2
3	8.3	7.9	10.9	11.0
4	5.4	8.7	10.1	5.0
	A	B	C	D

(b) PDT_SC1_HLS_75 °C

1		8.5	4.4	0.2
2	8.6	9.9	9.7	6.6
3	10.2	10.3	11.5	11.2
4	4.8	9.9	10.8	7.0
	A	B	C	D

(c)PDT_SC1_HLS_90 °C

1		8.7	2.8	0.2
2	8.4	10.3	10.2	7.1
3	10.5	10.8	10.9	11.3
4	2.8	10.4	10.7	5.8
	A	B	C	D

(d) PDT_SC1_HLS_112 °C

1		8.3	3.3	0.1
2	7.2	9.3	9.4	7.0
3	8.6	8.6	9.9	10.9
4	6.1	9.7	10.6	5.5
	A	B	C	D

(e) PDT_SC1_HLS_145 °C

Figure 6.49: Efficiency measurements of sample PDT_SC1 before (RT) and after Heat-Light Soaking at temperatures 75 °C, 90 °C, 112 °C and 145 °C.

Chapter 7

Conclusions

In this study, we investigated the effect of Cesium doping on the performance of Cu(In,Ga)Se_2 (CIGS) solar cells using a novel $CsCO_3$ spin-coating process. The performance of both non-treated and Cs-treated samples subjected to different post-process conditions, such as heat, light, and heat-light soaking, were evaluated using two electrical/optoelectronic device analysis techniques: External Quantum Efficiency Measurement and J-V measurements in the Solar Simulator.

The $CsCO_3$ solution was applied to the CIGS absorber through a spin-coating post-deposition treatment and the samples subjected to this treatment twice exhibited significant improvements in the open-circuit voltage and efficiency (of approximately 100 mV and 3.1%). An increase in the EQE indicated the reduction of recombination losses in the buffer/absorber interface and in the CIGS absorber. The improvement may be due to the modification of the CIGS absorber surface through the formation of O-Cs structures with Indium causing the lowering of the valence band maximum in the CdS/CIGS interface, leading to a reduction of recombination in this region. Another possible reason proposed was the elimination of deep-gap states at GBs through the formation of Cs_{Cu}. To confirm these hypothesis, further characterization techniques should be employed. For instance, Ultraviolet Photoelectron Spectroscopy (UPS) can be used to observe the changes in the valence band, X-ray Photoelectron Spectroscopy (XPS) can help to understand if the structure formed is the one suggested, and Energy Dispersive X-ray Spectroscopy (EDS) can be employed to analyze the presence of Cs in the grain boundaries, which is still under debate.

In this study, the twice spin-coated samples showed better solar cell basic parameters and EQE values, suggesting that a major quantity of Cs used in the treatment leads to better results. To confirm this hypothesis, more studies should be done, since the variability of the solar cell basic parameters is quite large. For example, this hypothesis should be tested with more samples or even trying to do the spin-coating treatment three times and check if the improvements persist.

J-V and EQE characterizations indicate that the light soaking process does not have a noticeable effect on the twice Cs-spin-coated CIGS sample, PDT_SC2a. A balance between detrimental and positive effects may lead to a no discernible net effect: the new distribution of the Cs atoms after the LS may

lead to electrostatic fluctuations which are counteracted by a possible increase of the diffusion-length of the charge carriers after the LS treatment. To fully observe any positive effects of light soaking, it is suggested that the sample be kept in the dark for one week after treatment to allow for proper redistribution of charges and potentially detectable changes in the solar cell's basic parameters.

The heat soaking treatment of the twice Cs-spin-coated sample, PDT_SC2b, resulted in negligible changes in the device performance. However, the selected cell exhibited a slight reduction in the fill factor (by approximately 3.1%), which in turn led to a decrease in efficiency (of around 0.65%). This reduction in efficiency may have been caused by a corresponding decrease in R_{Shunt}. The lack of substantial improvement in the solar cell parameters under the current conditions suggests that higher temperatures or longer annealing times may be necessary to achieve improved device performance.

Trying the LS and HS in samples subjected to the spin-coating more than twice and on non-treated samples would give more insight into the role of the alkali in these treatments. This is particularly important when using the alkali-solution spin-coating method, which has not been previously extensively studied.

The impact of heat-light soaking (HLS) has been investigated in a non-treated sample (Reference Sample 2) and in a sample to which the $CsCO_3$ solution PDT was done once (PDT_SC1). Both samples show a decrease in V_{OC}, of around 5.2% and 8.8% respectively, and an increase of the J_{SC}, of the order of 25.9% and 13.3% correspondingly comparing the sample at RT and the sample after the HLS at 145 °C. The FF and Efficiency did not show significant changes since these parameters presented large errors. Considering that the tendencies registered for both samples are similar, it is proposed that the mechanism behind these results is similar too and may be due to the samples' fabrication procedure. It is also hypothesized that a decrease of the number of holes and a consequent increase of the SCR may happen which results in the decrease of the V_{OC} and increase of the J_{SC}, the opposite trade-off registered in literature. Capacitance-voltage measurements should be performed to check this hypothesis. The increase of J_{SC}, could also be due to the diffusion of Na and K from the SLG substrate to the Mo back-contact and consequent increase of the carrier collection efficiency.

It is suggested that the V_{Se}-V_{Cu} complex is not related to the results presented. To investigate this hypothesis, the growth of CIGS under Se-rich conditions and Na treatment would suppress the formation of this complex and make it clear on how this complex affects or not the basic solar cell parameters.

The collection of photons in the CdS and CdS/CIGS interface increases with temperature for the Cs-treated samples, while the opposite happens to the non-treated sample. It is suggested that the HLS allows the migration of Cs atoms, which with the higher temperatures, may enhance the passivation of recombination centers in the interface by these atoms, contributing to a greater diffusion length. Both samples present a better collection of carriers generated in the CIGS with increasing temperature.

For the higher temperature, both samples show an S-kink for some cells, which is suggested to be a p+ defected layer resultant from the accumulation of holes in the CIGS , which contradicts in a certain way the initial hypothesis that the number of holes would decrease with the temperature. This distortion

may not be so sharp in the Cs-treated sample because it is said to be reduced by blue light, which is better absorbed and collected in this sample.

In summary, the Cs-solution spin coating doping has been demonstrated to improve the performance of CIGS solar cells, but further research is needed to understand which is the best quantity/concentration of solution to achieve the best solar cell efficiency. On the other hand, HS and LS treatments did not exhibit a significant impact on the Cs-treated CIGS solar cells. HLS treatment resulted in a distinct behavior compared to what was previously reported, for both non-treated and alkali-treated CIGS, including a decrease in V_{OC} and an increase in J_{SC}, along with an increase in efficiency. For future investigations, HS, LS, and HLS treatments should be conducted on samples from the same batch of CIGS, with consistent treatment to investigate their individual and combined effects. Given the significant variability in the solution-PDT process, additional statistical data and characterization are required to verify the outcomes obtained for the various treatments.

References

[1] Fred Ortenberg. *Ozone: Space Vision (Space monitoring of Earth Atmospheric Ozone)*. 01 2002.

[2] Rabindra Satpathy and Venkateswarlu Pamuru. Chapter 4 - Making of crystalline silicon solar cells. In Rabindra Satpathy and Venkateswarlu Pamuru, editors, *Solar PV Power*, pages 71–134. Academic Press, 2021.

[3] Rui Vilão. Semicondutores e nanoestruturas. Unpublished Manuscript, 2019.

[4] Ishwor Khatri. Power point presentation: Routes to high-efficiency solar cell. LaNaSc group meeting, 2021.

[5] Billel Salhi. The photovoltaic cell based on cigs: Principles and technologies. *Materials*, 15(5), 2022.

[6] Pedro Henrique Oliveira de Melo Santos. Growth and characterization of Cu(In,Ga)Se_2 thin film solar cells with a cu-rich cu-in-ga target. Master's thesis, Universidade do Minho, 2020.

[7] Maria Inês Mendes Martins. Innovative dielectric materials for passivation of interfaces in solar cells: a musr study. Master's thesis, Universidade de Coimbra, 2020.

[8] Jeffery Gray. *The Physics of the Solar Cell*, pages 82 – 129. 03 2011.

[9] Markus Gloecker. Device Physics of Cu(In,Ga)Se_2 Thin-Film Solar Cells. Master's thesis, Colorado State University, 2005.

[10] ZEISS Crossbeam. Cigs solar cells. 2018.

[11] Jeyakumar Ramanujam and Udai P. Singh. Copper indium gallium selenide based solar cells – a review. *Energy Environ. Sci.*, 10:1306–1319, 2017.

[12] Fabien Mollica. *Optimization of ultra-thin Cu(In, Ga)Se_2 based solar cells with alternative back-contacts*. PhD thesis, Université Pierre et Marie Curie-Paris VI, 2016.

[13] Gregory Ferguson Brown. *The Effects of Non-Uniform Electronic Properties on Thin Film Photovoltaics*. University of California, Berkeley, 2011.

[14] Xiaofang Chen, Yaoxin Hu, Zongli Xie, and Huanting Wang. Chapter 3 - Materials and Design of Photocatalytic Membranes. In Angelo Basile, Sylwia Mozia, and Raffaele Molinari, editors, *Current Trends and Future Developments on (Bio-) Membranes*, pages 71–96. Elsevier, 2018.

[15] Yazi Wang, Lv Shasha, and Zhengcao Li. Review on incorporation of alkali elements and their effects in Cu(In,Ga)Se_2 solar cells. *Journal of Materials Science Technology*, 96, 01 2021.

[16] Tzu-Ying Lin, Ishwor Khatri, Junpei Matsuura, Kosuke Shudo, Wei-Chih Huang, Mutsumi Sugiyama, Chih-Huang Lai, and Tokio Nakada. Alkali-induced grain boundary reconstruction on Cu(In,Ga)Se_2 thin film solar cells using cesium fluoride post deposition treatment. *Nano Energy*, 68:104299, 2020.

[17] Junpei Matsuura, Ishwor Khatri, Tzu-Ying Lin, Mutsumi Sugiyama, and Tokio Nakada. Impact of heat-light soaking and heat-bias soaking on naf-treated cigs thin film solar cells. *Progress in Photovoltaics: Research and Applications*, 27(7):623–629, 2019.

[18] I.Khatri et. al. Effect of Solution-Processed Cesium Carbonate on Cu(In,Ga)Se_2 Thin-Film Solar Cell. Manuscript under preparation, 2022.

[19] Bayram Saparov. Next Generation Thin-Film Solar Absorbers Based on Chalcogenides. *Chemical Reviews*, 122(11):10575–10577, 2022. PMID: 35673852.

[20] Giancarlo C. Righini and Francesco Enrichi. Chapter One - Solar cells' evolution and perspectives: a short review. In Francesco Enrichi and Giancarlo C. Righini, editors, *Solar Cells and Light Management*, pages 1–32. Elsevier, 2020.

[21] Solar Frontier. Solar Frontier Achieves World Record Thin-Film Solar Cell Efficiency of 23.35%, 2019, 2019.

[22] J. de Wild, M. Simor, D.G. Buldu, T. Kohl, G. Brammertz, M. Meuris, J. Poortmans, and B. Vermang. Alkali treatment for single-stage co-evaporated thin $CuIn_{0.7}Ga_{0.3}Se_2$ solar cells. *Thin Solid Films*, 671:44–48, 2019.

[23] Onyekachi Nwakanma, Arturo Morales-Acevedo, and Velumani Subramaniam. Study Of The Effects Of Non-Vacuum Deposited Alkali-Metals On Copper-Indium-Gallium-Selenide Absorber Layers For Solar Cells. In *2020 47th IEEE Photovoltaic Specialists Conference (PVSC)*, pages 2392–2396. IEEE, 2020.

[24] Jinsong Huang, Zheng Xu, and Yang Yang. Low-Work-Function Surface Formed by Solution-Processed and Thermally Deposited Nanoscale Layers of Cesium Carbonate. *Advanced Functional Materials*, 17:1966 – 1973, 08 2007.

[25] Liu, Debei and Wang, Gang and Niu, Lian and Chen, Li and Liu, Ding and Rao, Xi and Elseman, Ahmed and Song, Qun. Energy Level Bending of Organic-Inorganic Halide Perovskite by Interfacial Dipole. *physica status solidi (RRL) - Rapid Research Letters*, 13, 04 2019.

[26] Michael Gostein and Larry Dunn. Light soaking effects on photovoltaic modules: Overview and literature review. *Conference Record of the IEEE Photovoltaic Specialists Conference*, pages 003126–003131, 06 2011.

[27] Yong-Duck Chung, Dae-Hyung Cho, Nae-Man Park, Kyu-Seok Lee, and Jeha Kim. Effect of annealing on CdS/Cu(In,Ga)Se_2 thin-film solar cells. *Current Applied Physics*, 11(1):S65–S67, 2011.

[28] Hamidou Tangara, Yulu He, Muhammad Monirul Islam, Shogo Ishizuka, and Takeaki Sakurai. Analysis of the combined effect of long-term heat light soaking and KF/NaF post-deposition treatment on the open-circuit voltage loss in CIGS solar cells. *Japanese Journal of Applied Physics*, 61(SC):SC1050, 2022.

[29] Ishwor Khatri, Kosuke Shudo, Junpei Matsuura, Mutsumi Sugiyama, and Tokio Nakada. Impact of heat-light soaking on potassium fluoride treated CIGS solar cells with CdS buffer layer. *Progress in Photovoltaics: Research and Applications*, 26(3):171–178, 2018.

[30] Ishwor Khatri, Takahiko Yashiro, Tzu-Ying Lin, Mutsumi Sugiyama, and Tokio Nakada. Metastable Behavior on Cesium Fluoride-Treated Cu(In_{1-x}, Ga_x)Se_2 Solar Cells. *physica status solidi (RRL)–Rapid Research Letters*, 14(4):1900701, 2020.

[31] SEIA. https://www.seia.org/initiatives/about-solar-energy. Last accessed:12 August 2022.

[32] Adolf Goetzberger, Christopher Hebling, and Hans-Werner Schock. Photovoltaic materials, history, status and outlook. *Materials Science and Engineering: R: Reports*, 40(1):1–46, 2003.

[33] Y. Jestin. 1.26 - Down-Shifting of the Incident Light for Photovoltaic Applications. In Ali Sayigh, editor, *Comprehensive Renewable Energy*, pages 563–585. Elsevier, Oxford, 2012.

[34] D.L. King, J.A. Kratochvil, and W.E. Boyson. Measuring solar spectral and angle-of-incidence effects on photovoltaic modules and solar irradiance sensors. In *Conference Record of the Twenty Sixth IEEE Photovoltaic Specialists Conference - 1997*, pages 1113–1116, 1997.

[35] PVEducation. https://www.pveducation.org/pvcdrom/properties-of-sunlight/air-mass. Last accessed:14 August 2022.

[36] PVEducation. https://www.pveducation.org/pvcdrom/appendices/standard-solar-spectra. Last accessed:14 August 2022.

[37] Ana Carolina Silva Duarte. Fabrication of Cu(In,Ga)Se_2 micro-concentrator photovoltaics. Master's thesis, Universidade do Minho, 2021.

[38] Vítězslav Benda. Photovoltaics: The Basics. In *A comprehensive guide to solar energy systems*, pages 151–179. Elsevier, 2018.

[39] Badih El-Kareh. *Semiconductor Crystals*, pages 1–38. Springer US, Boston, MA, 1995.

[40] Hans J. Queisser and Eugene E. Haller. Defects in Semiconductors: Some Fatal, Some Vital. *Science*, 281(5379):945–950, 1998.

[41] Marius Grundmann. *Physics of semiconductors*, volume 11. Springer, 2010.

[42] Matthew D. McCluskey and Anderson Janotti. Defects in Semiconductors. *Journal of Applied Physics*, 127(19):190401, 2020.

[43] Chapter 41 - Engineered Nanomaterials for Energy Applications. In Chaudhery Mustansar Hussain, editor, *Handbook of Nanomaterials for Industrial Applications*, Micro and Nano Technologies, pages 751–767. Elsevier, 2018.

[44] Dr.Alan Doolittle. https://alan.ece.gatech.edu/ECE3080/Lectures/ECE3080-Equilibreum%20and%20Einstien%20Relationships%20-%20Recombination%20-%20Generation.pdf. Last accessed: 23 August 2022.

[45] Wikipedia. https://en.wikipedia.org/wiki/Fermi_energy. Last accessed: 24 August 2022.

[46] Khan Academy India-English. Forward biasing a p-n junction. Available at https://www.youtube.com/watch?v=2iWnCoL1F04. Last accessed: 26 August 2022.

[47] Khan Academy India-English. Reverse biasing a pn junction. Available at https://www.youtube.com/watch?v=TtF3bNyAm7k. Last accessed: 26 August 2022.

[48] Khan Academy India-English. Solar cells-iv characteristics. Available at https://www.youtube.com/watch?v=9IGAEKzdJ_k. Last accessed: 26 August 2022.

[49] Brian J. Skromme and G.K. Sujan. Semiconductor Heterojunctions. In *Reference Module in Materials Science and Materials Engineering*. Elsevier, 2018.

[50] *Basic Structure of Solar Cells*, chapter 6, pages 109–136. John Wiley & Sons, Ltd, 2005.

[51] Michael Saliba and Lioz Etgar. Current Density Mismatch in Perovskite Solar Cells. *ACS Energy Letters*, 5:2886–2888, 08 2020.

[52] cigs pv.net. https://cigs-pv.net/wortpresse/wp-content/uploads/2019/04/CIGS_White_Paper_2019_online.pdf. Last accessed 13 February 2022.

[53] Taesoo D. Lee and Abasifreke U. Ebong. A review of thin film solar cell technologies and challenges. *Renewable and Sustainable Energy Reviews*, 70:1286–1297, 2017.

[54] Marina do Carmo Alves. Cu(In,Ga)Se_2 thin film solar cell by magnetron sputtering. Master's thesis, Universidade do Minho, 2018.

[55] J.W. Martin. *Materials for Engineering (Third Edition)*. Woodhead Publishing, 2006.

[56] T Wada, N Kohara, S Nishiwaki, and Ts Negami. Characterization of the Cu(In,Ga)Se_2/Mo interface in CIGS solar cells. *Thin Solid Films*, 387(1-2):118–122, 2001.

[57] Adrian Chirilă, Patrick Reinhard, Fabian Pianezzi, Patrick Bloesch, Alexander R Uhl, Carolin Fella, Lukas Kranz, Debora Keller, Christina Gretener, Harald Hagendorfer, et al. Potassium-induced surface modification of Cu(In,Ga)Se_2 thin films for high-efficiency solar cells. *Nature materials*, 12(12):1107–1111, 2013.

[58] Yun Sun, Shuping Lin, Wei Li, Shiqing Cheng, Yunxiang Zhang, Yiming Liu, and Wei Liu. Review on alkali element doping in Cu(In,Ga)Se_2 thin films and solar cells. *Engineering*, 3(4):452–459, 2017.

[59] Onyekachi Nwakanma, Arturo Morales-Acevedo, and Velumani Subramaniam. Study Of The Effects Of Non-Vacuum Deposited Alkali-Metals On Copper-Indium-Gallium-Selenide Absorber Layers For Solar Cells. In *2020 47th IEEE Photovoltaic Specialists Conference (PVSC)*, pages 2392–2396. IEEE, 2020.

[60] P.M.P. Salomé, H. Rodriguez-Alvarez, and S. Sadewasser. Incorporation of alkali metals in chalcogenide solar cells. *Solar Energy Materials and Solar Cells*, 143:9–20, 2015.

[61] Nam-Trung Nguyen. Chapter 4 - Fabrication technologies. In Nam-Trung Nguyen, editor, *Micromixers (Second Edition)*, Micro and Nano Technologies, pages 113–161. William Andrew Publishing, Oxford, second edition edition, 2012.

[62] Richard Smith, Hiroshi Inomata, and Cor Peters. Chapter 4 - Historical Background and Applications. In Richard Smith, Hiroshi Inomata, and Cor Peters, editors, *Introduction to Supercritical Fluids*, volume 4 of *Supercritical Fluid Science and Technology*, pages 175–273. Elsevier, 2013.

[63] Paras and Aditya Kumar. Anti-Wetting Polymeric Coatings. In M.S.J. Hashmi, editor, *Encyclopedia of Materials: Plastics and Polymers*, pages 786–795. Elsevier, Oxford, 2022.

[64] Susanne Siebentritt, Enrico Avancini, Marcus Baer, Jakob Bombsch, Emilie Bourgeois, Stephan Buecheler, Romain Carron, Celia Castro, Sébastien Duguay, Roberto Felix, Evelyn Handick, Dimitrios Hariskos, Ville Havu, Philip Jackson, Hannu-Pekka Komsa, Thomas Kunze, Maria Malitckaya, Roberto Menozzi, Milos Nesladek, and Max Wolter. Heavy alkali treatment of Cu(In,Ga)Se_2 solar cells: Surface versus bulk effects. *Advanced Energy Materials*, 10:1903752, 01 2020.

[65] Ishwor Khatri, Hirofumi Fukai, Hiroshi Yamaguchi, Mutsumi Sugiyama, and Tokio Nakada. Effect of potassium fluoride post-deposition treatment on Cu(In,Ga)Se_2 thin films and solar cells fabricated onto sodalime glass substrates. *Solar Energy Materials and Solar Cells*, 155:280–287, 10 2016.

[66] Shiqing Cheng, Kaizhi Zhang, Shuping Lin, Yunxiang Zhang, Yun Sun, and Wei Liu. Analysis of the Heavy Alkali Element Postdeposition Treatment: Which Factors Determine the Electronic Structure and Transport Properties of the Heterojunction in CIGS Thin Film Solar Cells. *ACS Applied Energy Materials*, 4(4):3279–3287, 2021.

[67] Shiqing Cheng, Kaizhi Zhang, Yunxiang Zhang, Zhichao He, Baolai Liang, Qian Du, Yun Sun, and Wei Liu. Effects of different Cs distribution in the film on the performance of CIGS thin film solar cells. *Solar Energy Materials and Solar Cells*, 222:110917, 2021.

[68] Si Chen, Tobias Jarmar, Sven Södergren, Ulf Malm, Erik Wallin, Olle Lundberg, Sebastian Jander, and Lars Stolt. Light soaking induced doping increase and sodium redistribution in Cu(In,Ga)Se_2-based thin film solar cells. *Thin Solid Films*, 582, 05 2015.

[69] Katsumi Kushiya and Osamu Yamase. Stabilization of PN Heterojunction between Cu(InGa)Se_2 Thin-Film Absorber and ZnO Window with Zn(O, S, $OH)_x$ Buffer. *Japanese Journal of Applied Physics*, 39:2577–, 05 2000.

[70] F Engelhardt, M Schmidt, Th Meyer, O Seifert, J Parisi, and U Rau. Metastable electrical transport in Cu(In,Ga)Se_2 thin films and ZnO/CdS/Cu(In,Ga)Se_2 heterostructures. *Physics Letters A*, 245(5):489–493, 1998.

[71] Aleksandra Nikolaeva, Maximilian Krause, Norbert Schäfer, Wolfram Witte, Dimitrios Hariskos, Tim Kodalle, Christian A Kaufmann, Nicolas Barreau, and Daniel Abou-Ras. Electrostatic potential fluctuations and light-soaking effects in Cu(In,Ga)Se_2 solar cells. *Progress in Photovoltaics: Research and Applications*, 28(9):919–934, 2020.

[72] Jiro Nishinaga, Takashi Koida, Shogo Ishizuka, Yukiko Kamikawa, Hideki Takahashi, Masayuki Iioka, Hirofumi Higuchi, Yuko Ueno, Hajime Shibata, and Shigeru Niki. Effects of long-term heat-light soaking on Cu(In,Ga)Se_2 solar cells with KF postdeposition treatment. *Applied Physics Express*, 10(9):092301, 2017.

[73] Marco Giacomo Flammini, Nicola Debernardi, Maxime Le Ster, Brendan Dunne, Johan Bosman, and Mirjam Theelen. The influence of heating time and temperature on the properties of CIGSSe solar cells. *International Journal of Photoenergy*, 2016, 2016.

[74] Mohamed Fathi, Mahfoud Abderrezek, Farid Djahli, and Mohammed Ayad. Study of thin film solar cells in high temperature condition. *Energy Procedia*, 74:1410–1417, 2015.

[75] Ishwor Khatri, Junpei Matsuura, Mutsumi Sugiyama, and Tokio Nakada. Effect of heat-bias soaking on cesium fluoride-treated CIGS thin film solar cells. *Progress in Photovoltaics: Research and Applications*, 27(1):22–29, 2019.

[76] Romain Carron, Shiro Nishiwaki, Shih-Chi Yang, Mario Ochoa, Xiaoxiao Sun, Thomas Feurer, and Ayodhya Tiwari. Heat-light soaking treatments for high-performance CIGS solar cells on flexible substrates, 2022.

[77] Ishwor Khatri, K Shudo, J Matsuura, M Sugiyama, and T Nakada. Comparative study of heat light soaking on MF (M= K, Cs) treated CIGS solar cells with CdS buffer layer. *Proc. 27th PVSEC Kyoto Japan*, pages 12–17, 2017.

[78] Ajay Vasudeo Rane, Krishnan Kanny, V.K. Abitha, and Sabu Thomas. Chapter 5 - Methods for Synthesis of Nanoparticles and Fabrication of Nanocomposites. In Sneha Mohan Bhagyaraj, Oluwatobi Samuel Oluwafemi, Nandakumar Kalarikkal, and Sabu Thomas, editors, *Synthesis of Inorganic Nanomaterials*, Micro and Nano Technologies, pages 121–139. Woodhead Publishing, 2018.

[79] Matt Hughes. What is RF sputtering? Available at https://www.semicore.com/news/92-what-is-rf-sputtering. Last accessed: 5 November 2022.

[80] Jaime A Perez-Taborda, Liliana Vera, Olga Caballero-Calero, Elvis O Lopez, Juan J Romero, Daniel G Stroppa, Fernando Briones, and Marisol Martin-Gonzalez. Pulsed hybrid reactive magnetron sputtering for high zT Cu_2Se thermoelectric films. *Advanced Materials Technologies*, 2(7):1700012, 2017.

[81] David Fuster, Pedro Anacleto, José Virtuoso, Marco Zutter, Daniel Brito, Marina Alves, Luis Aparicio, David Marrón, Fernando Briones, Sascha Sadewasser, and Jorge García. System for manufacturing complete Cu(In,Ga)Se_2 solar cells in situ under vacuum. *Solar Energy*, 198:490–498, 03 2020.

[82] Xiao Peng, Ming Zhao, Daming Zhuang, Li Guo, Liangqi Ouyang, Rujun Sun, Leng Zhang, Yaowei Wei, Shilu Zhan, Xunyan Lv, Yixuan Wu, and Guoan Ren. Eliminating the excess Cu_xSe phase in Cu-rich Cu(In,Ga)Se_2 by In_2Se_3 treatment. *Journal of Alloys and Compounds*, 709:31–35, 2017.

[83] Diana Sofia Azevedo de Oliveira. Impact of alkali-post deposition treatment on Cu(In,Ga)Se_2 solar cells. Master's thesis, Universidade do Minho, 2022.

[84] Enlitech. Quantum efficiency/spectral response/IPCE application in Copper Indium Gallium Senillide (CIGS) solar cells. Available at https://enlitechnology.com/blog/qe/quantum-efficiency-01/. Last accessed: 18 January 2023.

[85] Hojin Lee, Yuseong Jang, Sung-Wook Nam, Chanwon Jung, Pyuck-Pa Choi, Jihye Gwak, Jae Ho Yun, Kihwan Kim, and Byungha Shin. Passivation of deep-level defects by cesium fluoride post-deposition treatment for improved device performance of Cu(In,Ga)Se_2 solar cells. *ACS applied materials & interfaces*, 11(39):35653–35660, 2019.

[86] Stephan Lany and Alex Zunger. Light-and bias-induced metastabilities in Cu(In,Ga)Se_2 based solar cells caused by the (V_{Se}-V_{Cu}) vacancy complex. *Journal of Applied Physics*, 100(11):113725, 2006.

[87] Mohsen Jahandardoost, Marco Nardone, Theresa Magorian Friedlmeier, Curtis Walkons, and Shubhra Bansal. Heat-and light-soaking behavior of RbF-treated Cu(In,Ga)Se_2 solar cells with two different buffer layers. *Journal of Materials Research*, 37(2):436–444, 2022.

[88] Hye-Jung Yu, Woo-Jung Lee, Jae-Hyung Wi, Dae-Hyung Cho, Won Seok Han, Yong-Duck Chung, Tae-Soo Kim, and Jung-Hoon Song. Light-soaking effects and capacitance profiling in Cu(In,Ga)Se_2 thin-film solar cells with chemical-bath-deposited ZnS buffer layers. *Physical Chemistry Chemical Physics*, 18(48):33211–33217, 2016.

[89] M. Igalson, Marika Bodegård, and Lars Stolt. Reversible changes of the fill factor in the ZnO/CdS/Cu(In,Ga)Se_2 solar cells. *Solar Energy Materials and Solar Cells*, 80(2):195–207, 2003.